Ultraviolet and visible semiconductor lasers based on ZnO heterostructures

D I S S E R T A T I O N

zur Erlangung des akademischen Grades

Dr. rer. nat.
im Fach Physik

eingereicht an der
Mathematisch-Naturwissenschaftlichen Fakultät I
Humboldt-Universität zu Berlin

von
Dipl.-Phys. Sascha Kalusniak

Präsident der Humboldt-Universität zu Berlin:
Prof. Dr. Jan-Hendrik Olbertz

Dekan der Mathematisch-Naturwissenschaftlichen Fakultät I:
Prof. Stefan Hecht, Ph.D.

Gutachter:
1. Prof. Dr. Fritz Henneberger
2. Prof. Dr. Oliver Benson
3. Prof. Dr. Heinz Kalt

eingereicht am: 07.06.2012
Tag der mündlichen Prüfung: 09.04.2013

Abstract

In the framework of this thesis, the optical properties of ZnO-based heterostructures fabricated by molecular beam epitaxy have been investigated, particularly with regard to their suitability for semiconductor laser devices operating in the ultraviolet and visible spectral range. It turned out that ZnO and its ternary alloys ZnMgO and ZnCdO are extremely versatile. They allow to tune the laser emission in a wide spectral range as well as to realize various laser geometries, even if they require a considerable amount of optical gain. In detail, it was shown that the laser emission of ZnCdO/ZnO multiple quantum wells can cover a spectral range from violet to green wavelengths. Although these structures suffer from large built-in electric fields, room temperature laser action under optical pumping was demonstrated up to a wavelength of 510 nm on appropriately designed samples. The optical feedback for lasing is provided by growth imperfections on a macroscopic length scale turning these structures into random lasers. The fabrication of micro-resonators allowed for the first study on the interplay between random and Fabry-Perot feedback. The experimental and theoretical analysis show that random feedback generally requires a larger gain than under Fabry-Perot feedback, which can be provided by ZnO nanostructures. Moreover, the random feedback creates a subtle modal gain distribution of the Fabry-Perot laser.
Further, this work demonstrates for the first time that ZnO- and ZnMgO-layers can be used to fabricate highly reflective distributed Bragg reflectors for applications in the ultraviolet and blue/green spectral range. The key is the ability for growth of strongly alloyed, single-phase ZnMgO ternary films with a good surface morphology. The index of refraction of such an alloy is significantly reduced compared to that of ZnO, which makes the fabrication of distributed Bragg reflectors possible. The partly unknown dispersion curves of the index of refraction of the employed ternary alloys have been elaborated, allowing for a theoretical description of the experimental spectra. This enabled the design and finally the realization of all monolithic microcavities with ZnO/ZnMgO quantum wells as active zone. For temperatures below 150 K strong exciton-photon coupling is observed in such microcavities. The homogeneous broadening of the quantum well excitons destroys the strong coupling at higher temperatures. Increasing the number of quantum wells will allow to overcome this limitation. At room temperature, vertical cavity surface emitting laser action in the near UV spectral range is demonstrated for appropriately designed microcavities.

Keywords:
(Mg,Cd,Zn)O heterostructures, visible- and ultraviolet-emitting laser, random laser, microcavities, vertical cavity surface emitting laser, strong exciton-photon coupling

Zusammenfassung

Im Rahmen dieser Arbeit wurden die optischen Eigenschaften von, mittels Molekularstrahl Epitaxie hergestellten, auf ZnO-basierenden Heterostrukturen untersucht. Besonderes Augenmerk lag hierbei auf ihrer Eignung als aktives Material in Laserdioden für den ultravioletten und sichtbaren Spektralbereich. Es wurde gezeigt, dass ZnO und seine ternären Mischkristalle ZnCdO und ZnMgO erstaunlich vielfältige Anwendungen ermöglichen. Es lässt sich mit diesem Materialsystem sowohl ein sehr großer Spektralbereich für Lasertätigkeit abdecken als auch eine Vielzahl von Lasergeometrien realisieren, darunter auch Geometrien, welche einen hohen optischen Gewinn benötigen. Im Detail wurde demonstriert, dass sich die Lasertätigkeit von ZnCdO/ZnO Quantengraben-Strukturen vom violetten bis in den grünen Spektralbereich verschieben lässt. Obwohl diese Strukturen starke interne elektrische Felder aufweisen, konnte an maßgeschneiderten Proben optisch gepumpte Lasertätigkeit bei Zimmertemperatur bis zu einer Wellenlänge von 510 nm demonstriert werden. In weiteren Untersuchungen stellte sich heraus, dass die für die Lasertätigkeit nötige optische Rückkopplung durch makroskopische Defekte der Probe verursacht wird und die Proben somit als Zufallslaser fungieren. Die Herstellung von Mikroresonatoren ermöglichte erstmals die Untersuchung des Zusammenspiels von Fabry-Perot- und Zufalls-Rückkopplung. Die experimentellen und theoretischen Ergebnisse zeigen, dass der Schwellengewinn eines Zufallslasers in der Regel größer ist als der des Fabry-Perot-Lasers. Dieser hohe Schwellengewinn kann von ZnO Nanostrukturen zur Verfügung gestellt werden. Außerdem führt die Zufalls-Rückkopplung zu einer Modifikation der modalen Gewinnverteilung des Fabry-Perot-Lasers.
Des Weiteren wurde im Rahmen dieser Arbeit zum ersten Mal gezeigt, dass hoch reflektierende Braggreflektoren für den ultravioletten und blau/grünen Spektralbereich aus ZnO- und ZnMgO-Schichten hergestellt werden können. Die Möglichkeit phasenreine, stark vermischte ternäre ZnMgO-Schichten mit einer guten Oberflächenmorphologie herzustellen ist hierbei der Schlüssel. Diese Mischkristalle weisen im Vergleich zu ZnO einen erheblich reduzierten Brechungsindex auf, was die Herstellung von Braggreflektoren erst ermöglicht. Ferner wurden die teils unbekannten Brechungsindexverläufe der verwendeten ternären Materialen erarbeitet um die experimentell gewonnenen Spektren theoretisch reproduzieren zu können. Dies erlaubte es, Mikrokavitäten mit ZnO/ZnMgO Quantengraben Strukturen als aktive Schichten zu entwerfen und letztendlich zu realisieren. An diesen Kavitäten konnte bei Temperaturen bis zu 150 K starke Kopplung zwischen Exzitonen und Photonen nachgewiesen werden. Die Zunahme der homogenen Verbreiterung der Exzitonen bei höheren Temperaturen zerstört die starke Kopplung. Diese Begrenzung lässt sich aber durch eine erhöhte Zahl an ZnO Quantengräben aufheben. An entsprechend entworfenen Mikrokavitäten konnte bei Zimmertemperatur vertikal-emittierende Lasertätigkeit im nahen ultravioletten Spektralbereich demonstriert werden.

Keywords:
(Mg,Cd,Zn)O Heterostrukturen, sichtbar- und ultraviolett-emittierender Laser, Zufallslaser, Mikrokavitäten, vertikal-emittierender Laser, starke Licht-Exziton Kopplung

Contents

1. Introduction

Optoelectronics is a key technology of this century. Very recently the German government has established the "Photonik Forschung Deutschland - Licht mit Zukunft" program to support research and development in this field by approximately 400 million Euro over four years. This attempt is mainly driven by the increasing economic relevance of optoelectronic devices. The field of application is large and includes, e.g., communication, display as well as lightening technology.
In many aspects, optoelectronics is inextricably linked with nanotechnology. In particular, semiconductor based nanostructures are of extraordinary relevance and will play a major role for future optoelectronic devices. Light emitting diodes (LEDs) and laser diodes (LDs) are part of our daily life, sometimes clearly recognizable but very often unperceived. In various kinds of displays, LEDs are an essential component and they will become more and more important for lightening applications. Semiconductor lasers are also of great technological importance, e.g., for data-storage applications (Compact Discs, Digital Versatile Discs and Blu-ray Discs), optical communication systems (especially fiber optical communication) and laser printers. Their compactness and versatility combined with a low-power consumption make LDs superior compared to other laser sources.
It appears obvious that present and future optoelectronic devices are of direct practical relevance. However, the development of new technologies and devices requires profound understanding of the underlying physics as well as detailed knowledge of the properties of the employed materials. This is where fundamental research comes into play. Tailoring of semiconductor nanostructures for specific applications is the major challenge. For LDs this includes manipulation of the emission wavelength as well as the design of appropriate resonators to control lasing threshold and emission characteristics.
The emission photon energy of a LD is determined by the respective band gap of the employed semiconductor which can be only manipulated in a "relatively" narrow spectral range by alloying of the semiconductor to a ternary compound. Moreover, the emission can be tuned by quantum size effects. However, a single semiconductor can only cover a part of the technological relevant spectral range, and new materials are required to extend the wavelength range further. This often requires to start again from the very beginning. Then, the objective is to find adequate growth regimes for the new material, to design and grow nanostructures and finally to investigate and evaluate their optical properties.
If these efforts culminate in the demonstration of stimulated emission at the desired wavelength, the next step is the designing of the resonator and, by that, to tailor mode spectrum and beam profile. The standard configuration is the Fabry-Perot resonator but also distributed feedback (DFB) laser and vertical cavity surface emitting laser (VCSEL)

devices are commonly used. While Fabry-Perot and DFB LDs are edge-emitter and therefore exhibit an elliptical beam profile, VCSEL devices emit from the sample surface with a narrow and circular beam profile, which allows for simplified coupling into fibers. Moreover, they offer single mode emission as opposed to Fabry-Perot laser [1] and can be tested directly after growth without cleaving or further processing. There are some more advantages compared to edge-emitting LDs (see, e.g., [1]), explaining the increasing use of VCSEL devices. Under certain conditions, there is even the possibility to observe and investigate the strong coupling of light and excitons in such devices. Recently, a new type of laser, the random laser, went into the focus. Here, the feedback for lasing is provided by scatterers which are randomly distributed in a gain medium or which by themselves act as optical amplifiers. Until now, their properties are not totally explored.
For a rather long time, the emission wavelength of available LDs was restricted to the infrared and red spectral range. This limit was a fundamental one, directly related to the small band gap of the employed materials (Phosphites as well as Arsenides and their alloys). First attempts, in the 1990s, to achieve electrically driven laser action in the blue/green spectral range by ZnSe-based heterostructures succeeded but a commercial level was never reached because of the limited device lifetime. The breakthrough was achieved with the (Al,In,Ga)N heterosystem. In the mid 1990s, the first electrically driven violet-emitting InGaN-based laser diode has been developed, allowing to increase the capacity for optical data storage (Blu-ray Discs). Extensive material research and an increasing understanding of the optoelectronic properties of the material system culminated so far in commercially available LDs emitting at a wavelength of 488 nm. Recently, it has been demonstrated that this range can be even extended into the true-green spectral range by further alloying GaN with Indium (see, e.g., [2] and references therein). Combining blue, green and red LDs would enable the realization of laser television and laser-based micro-projectors. However, true-green LDs are not commercially available, so far.
ZnO is an alternative semiconductor capable of short-wavelength emission in the near ultraviolet (UV) spectral range [3]. An intrinsically high radiative yield up to room temperature and a very strong exciton-photon coupling, both related to an exciton binding energy as large as 60 meV, are factors that make ZnO potentially superior to GaN. Other features in favor of ZnO are very low growth temperatures compatible with organic and biomolecules [4] and its radiation hardness. All these properties turn ZnO into a material with considerable potential for optoelectronic applications.
In fact, the fundamental properties of ZnO have been studied already in the 30s and 70s of the last century. Presently, there is a renewed interest in ZnO. A considerable amount of reports on stimulated emission and lasing of ZnO films and ZnO/ZnMgO heterostructures is found in literature (see e.g. [5] and references therein), demonstrating strong intentions to cultivate ZnO as a laser material. Surprisingly, attempts to go closer to more practical laser geometries are rarely reported in literature, and a resonator is often formed naturally. So far, only an optically pumped ZnO-based DFB laser has been reported [6].

[1] DFB lasers are also capable of single mode operation.

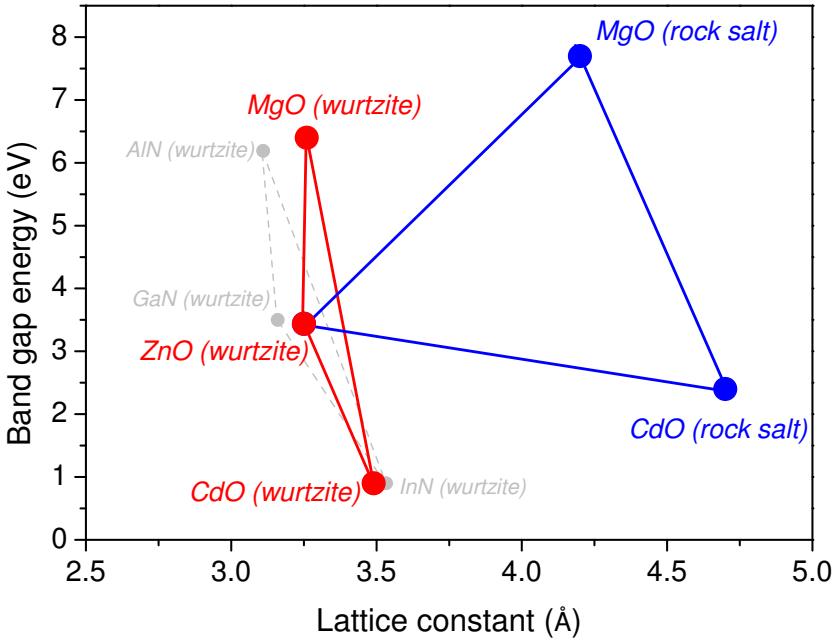

Figure 1.1: Band edge versus a-lattice constant for ZnO, MgO and CdO in wurtzite (red) and rock salt phase (blue). Parameters for ZnO as well as rock salt phase MgO and CdO are taken from [8]. Theoretical parameters for hypothetical wurtzite MgO and CdO are taken from [9]. The same dependence is also plotted for the (Al,In,Ga)N heterosystem. Parameters are taken from References [10] and [11].

The ternary alloys ZnMgO and ZnCdO are less studied, as their growth is more challenging and ternary films could be fabricated only since the end of the 90s. In particular, ZnCdO is a barely studied semiconductor so far. The number of publications concerning growth and optical properties of ZnCdO and ZnCdO/ZnO heterostructures is very limited (see, e.g., [7] and references therein). Therefore, its potential for optoelectronic applications is almost totally unexplored.
Figure 1.1 schematizes how the band gap can be engineered by alloying of ZnO with CdO or MgO. In principle, the ternary ZnCdO can cover a range extending from ultraviolet to infrared wavelengths, while the ZnMgO alloy is suitable to enlarge the band gap into the deep UV spectral range. However, unlike the group-III nitrides, the binary components have different crystalline structures, namely wurtzite for ZnO and rock salt for MgO as well as CdO. As a consequence, the equilibrium solubility limit of both, MgO and CdO in ZnO is only about some percent [3, 12]. Phase separation is thus an obstacle that has to be overcome when aiming at devices emitting at wavelengths essentially different from that of pure ZnO.
Utilizing molecular beam epitaxy (MBE), the Photonics Group at "Humboldt Universität zu Berlin" has established growth modes for both ternaries far away from thermal equilibrium, allowing to fabricate alloys with band gaps ranging from 4.4 down to 2.1 eV and to produce well-defined hetero- and quantum well (QW) structures [13].

Based on these achievements, this thesis is aimed to explore the fundamental potential of ZnO-based heterostructures as the active material for semiconductor laser devices operating in the UV and visible spectral range. This comprises both, to study the spectral tunability of the laser emission of ZnO-based QW structures as well as to realize some of the above-mentioned laser geometries. It will be shown, that the ternary ZnCdO is a potential candidate to make a semiconductor laser operating from violet to green wavelengths. Room temperature lasing of appropriately designed ZnCdO/ZnO multiple QW (MQW) structures will be presented up to wavelengths of 510 nm. The feedback for laser action of these samples is of random type. It will be studied more detailed and directly compared with the Fabry-Perot arrangement. Moreover, it is shown that highly reflective distributed Bragg reflectors (DBRs) can be fabricated out of ZnO- and ZnMgO-layers, allowing to fabricate all monolithic MCs with ZnO/ZnMgO QWs as active zone. Finally, strong exciton-photon coupling at cryogenic temperatures as well as room temperature VCSEL action in the UV wavelengths range will be demonstrated.

Outline of this thesis:
In **Chapter 2**, the physical properties of various gain processes and laser geometries are discussed. Further the influence of polarization charges on the emission of QWs is described and some principles of strong-exciton photon coupling in MCs are introduced.
Chapter 3 briefly describes the MBE apparatus used for sample fabrication as well as the conditions employed for their growth. The excitation sources and detection system used for optical investigation of the samples are summarized in the same chapter.
The optical properties of ZnCdO/ZnO QWs in the high-and low-density excitation regime are investigated in **Chapter 4**. It will be shown, that the low-density photoluminescence (PL) is affected by the presence of strong built-in electric fields. At moderate excitation intensities in the 10 kW/cm^2 effective screening of these fields by photogenerated carriers occurs. In the same excitation range, visible wavelength laser action of MQW structures is demonstrated from violet to green wavelengths.
In **Chapter 5**, it will be revealed that the ZnCdO/ZnO MQW structures actually act as random lasers as a result of macroscopic growth imperfections. Fabrication of Fabry-Perot resonators allows to study and to compare directly random and cavity feedback. A theoretical model will be presented and the numerical results will be discussed in context with the experiment.
The first realization of highly reflective DBRs based on ZnO and ZnMgO layers is presented in **Chapter 6**. Their design for ultraviolet and blue/green wavelengths will be discussed and their structural as well as optical properties will be evaluated.
Based on these findings, the successful fabrication of high quality all monolithic ZnO-based MCs with ZnO/ZnMgO QWs as active zone will be reported in **Chapter 7**. Strong exciton-photon coupling at cryogenic temperatures as well as room temperature VCSEL action in the UV-wavelengths range will be demonstrated for such MCs.
Finally, the main results of this work will be summarized.

2. Background

Although lasers can be fabricated by a multitude of different materials (e.g., gases, dyes, solid states and of course semiconductors) and in various geometries, the basic concept of a laser is always the same. A certain material, which provides optical gain and amplifies light by stimulated emission, is embedded in a resonator in which the light can circulate. The optical gain of the material itself is not a state of nature and has to be created by external pumping. The spectral range in which the laser can emit is then restricted to the energy range in which the medium amplifies light. As any resonator experience losses, the intensity of the light circulating in the resonator would continuously decay without optical gain. For laser action, the optical gain has to be large enough to compensate the losses of the resonator (and any additional losses that the system might experience), which defines the threshold condition of a laser.
This chapter will give a brief overview of relevant designs and gain processes of semiconductor lasers, in particular with regard to ZnO. Further the influence of built-in electric fields on the optical properties of QW structures as well as the regime of strong exciton-photon coupling in MCs will be discussed.

2.1. Optical gain in semiconductors

The occurrence of optical gain requires that the rate of stimulated emission of a transition exceeds its rate of absorption. In semiconductors, the fundamental optical excitation is the bound state of electron and hole, the exciton. However, in some materials electron and hole are only weakly bound at each other and at higher temperatures or densities the excitons dissociate and a plasma like phase is formed. Hence, optical gain in semiconductors can be either of excitonic nature or related to an electron-hole (e-h) plasma. In the following, possible gain processes in semiconductors will be presented, and it will be discussed under which conditions they occur. This will be treated in more detail for bulk material and finally modifications for quantum well structures will be discussed.
Further information on the e-h plasma in semiconductors can be found in many textbooks (e.g., [14, 15, 16]). For details about optical gain related to excitonic processes the reader might be referred to References [16] and [17].

2.1.1. The electron-hole plasma

A large number of e-h pairs is created in a semiconductor under high excitation conditions. In this case, many particle effects (e.g., screening of the Coulomb interaction as well as exchange- and correlation effects) strongly influence the optical properties. Among other effects, these interactions lead to a down-shift of the continuum states (a

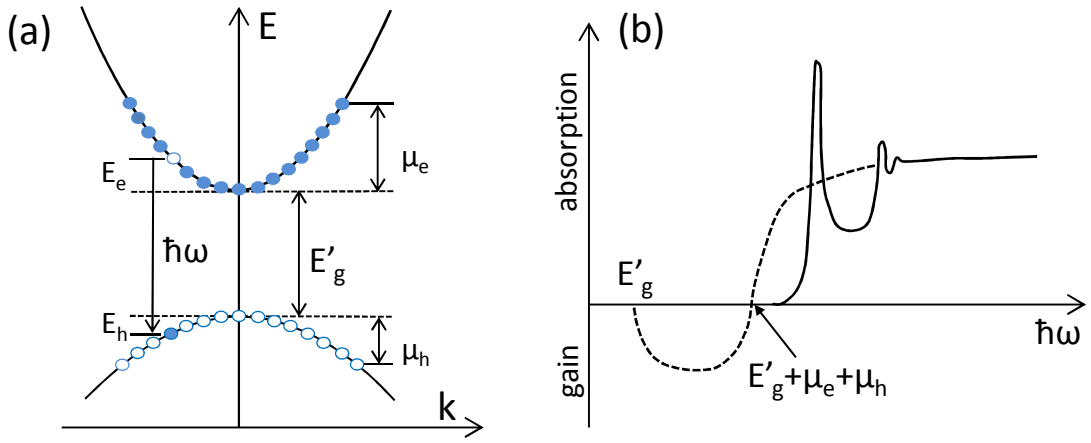

Figure 2.1: Optical gain related to an e-h plasma. (a) Scheme of recombination of an electron-hole plasma. (b) Absorption spectra without excitation (straight line) and in the presence of an e-h plasma (dashed line). Figure is adapted from [16].

shrunk gap (E'_g)) of the semiconductor while the excitonic energy levels hardly move until they become unstable by the crossing band gap [18]. When the injected carrier density reaches the Mott density (n_m), i.e. the down-shifting continuum crosses the exciton ground state level, excitons lose their identity as individual quasiparticles and a plasma like phase is formed.
A recombination scheme of an e-h plasma is shown in Figure 2.1 (a). Valence and conduction band are filled up to the respective chemical potential μ_h and μ_e. Recombination of an electron and hole leaves behind an empty state in the conduction band and an occupied state in the valence band. Both states rapidly relax to lower energies.
A complete theory, which takes all many-body and band-structure effects into account, is very complicated. An approximation formula for the optical spectrum of the gain coefficient, which allows to discuss important aspects, is given in Reference [16]:

$$g(\hbar\omega) \sim M^2 \sqrt{\hbar\omega - E'_g} \cdot (f_e + f_h - 1) \quad \text{for } \hbar\omega > E'_g, \tag{2.1}$$

with M being the transition matrix element and the square root term describes the density of states of the bulk semiconductor. The term in parentheses is the population factor with the Fermi distribution functions for electrons $f_e(E) = (1+e^{\frac{E_e-\mu_e}{kT}})^{-1}$ and holes $f_h(E) = (1+e^{\frac{E_h-\mu_h}{kT}})^{-1}$. In this notation μ_e and E_e are measured from the conduction band edge and are positive into the conduction band and μ_h and E_h are measured from the valence band edge and are positive into the valence band. Hence, gain can only appear if the condition $f_e(E) + f_h(E) > 1$ and thus $\mu_e + \mu_h > E_e + E_h$ is fulfilled. The magnitude of optical gain is directly related to the transition matrix element. The spectral shape of absorption without excitation and in the plasma state is illustrated in Figure 2.1 (b). At low carrier densities, sharp excitonic features followed by the above-band gap continuum absorption appear in the absorption spectrum. These features

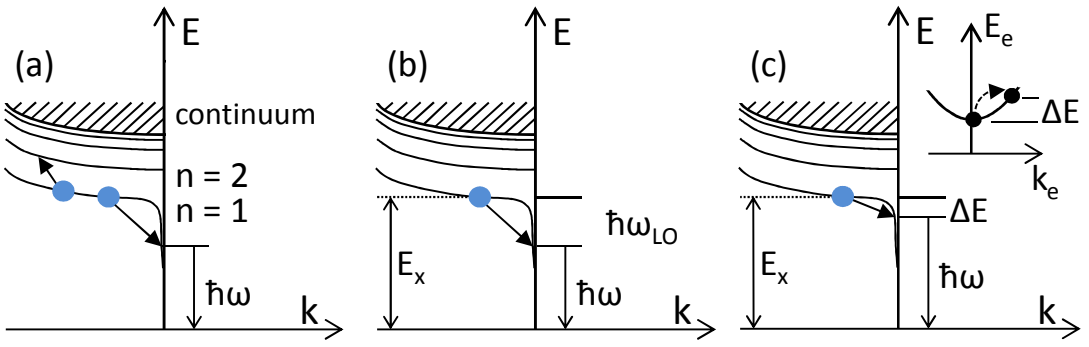

Figure 2.2: Inelastic scattering and recombination of excitons (scheme). (a) Inelastic exciton-exciton scattering. (b) Exciton-phonon scattering. (c) Exciton-free carrier scattering. Upper right: free electron in the conduction band. Figure is adapted from [16].

vanish for an e-h plasma, and gain occurs in the spectral region $E_g' < \hbar\omega < E_g' + \mu_e + \mu_h$. For higher photon energies a sharp crossover from gain to absorption sets in.
The condition $\Delta E_g = -R_y$, i.e., the red-shift of the band gap is as large as the exciton binding energy, allows for estimation of the Mott density

$$r_s = (\frac{4\pi a_b^3}{3} n_m)^{-\frac{1}{3}}, \tag{2.2}$$

with a_b being the Bohr radius and r_s the density parameter. From this formula a density of about $n_m = 4 \cdot 10^{17}\text{cm}^{-3}$ is found at a temperature of 5 K using $a_b = 1.8$ nm [8] and $r_s = 4.8$ for ZnO (for details see [18]). This is a relatively large density compared with other semiconductors, suggesting relevance of excitonic processes even at high injection levels.
In materials with a large Bohr radius, e.g., GaAs and CdTe an e-h plasma emerges much faster when the carrier density is increased. Indeed, the above-described mechanism is responsible for optical gain in these materials. However, optical gain related to an e-h plasma as been also observed in ZnO-films [19, 20, 21] at higher excitation intensities.

2.1.2. Excitonic processes

If the injected carrier density is still below the Mott density excitons can be treated as individual particles. However, if the system is sufficiently dense they can start to interact with each other and several scattering processes can take place, as illustrated in Figure 2.2. Because of its large Mott density, ZnO is predestinated in this regard. In principle, these interactions can lead very efficiently to optical gain, as it will be discussed in the following.

Exciton-exciton scattering

If the density of excitons is high enough, two excitons with state n = 1 and wave vector ($\vec{k}$) can scatter inelastically. One of the excitons is excited into a n = 2 state, while the other one decays into a photon with energy $\hbar\omega$, as shown in Figure 2.2 (a). The population factor for stimulated emission of exciton-exciton scattering is [17]:

$$Q_{\mathrm{stim}} \sim n_{\mathrm{x}}(1,\vec{k_1})n_{\mathrm{x}}(1,\vec{k_2}) - n_{\mathrm{x}}(2,\vec{k_1}+\vec{k_2})[1+n_{\mathrm{x}}(1,\vec{k_1})+n_{\mathrm{x}}(1,\vec{k_2})], \tag{2.3}$$

with $n_{\mathrm{x}}(\mathrm{n},\vec{k})$ being the thermal population function of excitons in state n. The gain increases roughly quadratically with the exciton density. Even a single scattering event is sufficient to generate optical gain if the excited state n = 2 is not thermally populated.

Exciton-LO-phonon scattering

The decay of an exciton by creation of a LO-phonon is illustrated in Figure 2.2 (b). In this case, the population factor for exciton-phonon scattering is [17]:

$$Q_{\mathrm{stim}} \sim n_{\mathrm{x}}(1,\vec{k_1}) - n_{\mathrm{LO}}. \tag{2.4}$$

A relatively low temperature is required in order to avoid reabsorption by thermally occupied phonons. Because of the linear dependence on the exciton concentration, lasing by exciton-exciton scattering is favored in the case of high photon losses of the system.

Exciton-electron scattering

An exciton can also recombine by scattering with free carriers (electrons or holes), as shown for the electron case in Figure 2.2 (c). The electron is scattered into a state with higher kinetic energy (inset in Figure 2.2 (c)) while the exciton decays radiatively. In this case energy and momentum conservation yields a continuum of possible photon energies. The population factor for stimulated emission is given by [17]:

$$Q_{\mathrm{stim}} \sim n_{\mathrm{x}}(1,\vec{k_1})n_{\mathrm{e}}(\vec{k_{\mathrm{e}}}) - n_{\mathrm{e}}(\vec{k_1}+\vec{k_{\mathrm{e}}})[1+n_{\mathrm{x}}(1,\vec{k_1})-n_{\mathrm{e}}(\vec{k_{\mathrm{e}}})], \tag{2.5}$$

with $n_{\mathrm{e}}(\vec{k_{\mathrm{e}}})$ being the thermal population function of electrons. This process requires a large amount of free electrons, which can be provided by ionized donors. The number of free carriers at higher energies as to be low to prevent reabsorption of photons. Normally, the effective mass of the electron is lower than that of the hole. Hence, this condition is easier fulfilled for electrons.

For more details about optical gain related to excitons in ZnO see [5] and references therein.

2.1.3. Quantum well structures and polarization fields

The above mentioned mechanisms are not restricted to bulk material but can also occur in QW structures. However, the heterostructure itself as well as the quantum confinement can lead to significant modifications. On the one hand, the density of states is modified from the square root dependence of the bulk material to a staircase dependence, accounting for the discrete energy levels of the QW. Further, the enhanced binding energy due to the quantum confinement makes the exciton stable up to higher temperatures and densities and increases the transition matrix element. On the other hand, QW structures usually suffer from inhomogeneous broadening. Alloy disorder in the well and/or barrier and interface roughness form a potential landscape in which excitons can localize. These factors give rise for novel lasing scenarios discovered first on ZnSe-based QWs.

Gain of localized excitons

Optical gain related to localized excitons has been observed on ZnCdSe/ZnSe-based QW structures [22]. If only one exciton can occupy a localization site, stimulated emission occurs when the fraction of occupied localizations sites is larger than that of unoccupied localization sites

$$2n_{\mathrm{x}} - 1 > 0. \tag{2.6}$$

For a single localization site this means that gain will emerge if it is occupied and absorption if it is not.

Gain of localized biexcitons

The above-described mechanism assumes that only one exciton can occupy a single localization side. However, if the spin of the excitons is opposite aligned an excitonic molecule (the biexciton) might be formed. It has been demonstrated on ZnCdSe/ZnSe-based QWs that optical gain of localized biexcitons can emerge [23]. For a positive net rate of stimulated emission, the fraction of localization sites occupied by biexcitons in the system has to be larger than that of occupied by excitons [24]

$$n_{\mathrm{xx}} - n_{\mathrm{x}} > 0. \tag{2.7}$$

Gain by negatively charged trions

Another exciton complex which has been observed is the trion. If negatively charged, it consists of two electrons and one hole. Optical gain and lasing related to the transition of such a trion state in n-doped ZnSe QWs has been also reported [25]. A positive net

rate of stimulated emission requires

$$n_{\mathrm{x}^-}(\vec{K}) - n_{\mathrm{e}}(\vec{k}) > 0, \tag{2.8}$$

with $n_{\mathrm{x}^-}(\vec{K})$ being the population function of trions. The distribution in $\vec{k}$-space is different for trion and electron because of a larger trion mass. Hence, gain does not require inversion in the total particle number.

Emission from Biexcitons has been also observed in ZnO/ZnMgO QW structures [26, 27] as well as trion-related emission [27] and lasing [28].
Of course, all these processes require the existence of excitons, i.e., the density of injected carriers must be lower than n_{m}. The Mott density of QW structures is usually higher compared to bulk material because of the quantum confinement. According to Schmitt-Rink *et al.* [29] the Mott density of an ideal 2-dimensional ZnO QW structure is in the range of $5 \cdot 10^{12}\mathrm{cm}^{-2}$. A real QW structure is somewhere in between a 2-dimensional and 3-dimensional system, which suggests a density between bulk ZnO and an ideal 2-dimensional QW.

Polarization fields in quantum well structures

Similar to III-Nitrides in wurtzite phase, ZnO is known to exhibit strong spontaneous and piezoelectric polarization effects [3]. Even when grown on the *a*-plane of sapphire, the growth direction of a ZnO-based QW structure is along the polar *c*-axis of the wurtzite lattice. As a consequence, the spontaneous polarization difference between QW and barrier as well as the strain-induced piezoelectric polarization of the well can create considerable polarization charges at the well-barrier interface [30]. If the difference in the *a*-lattice constant of QW and barrier material is large and the well is grown pseudomorphically, piezoelectric polarization charges can be expected.
For the ZnMgO alloy only a slight increase of the *a*-lattice constant with Mg content has been found [12, 31]. The change in the lattice constant is approximately $\Delta a = 0.30\%$ for a Mg content of $x = 0.30$. Consequently, ZnO/ZnMgO QWs should suffer only from relatively weak tensile strain. However, when alloying ZnO with Cadmium the *a*-lattice constant of the wurtzite-phase alloy rapidly increases reaching $\Delta a = 2.40\%$ already at a Cadmium content of $y = 0.21$ [13]. Such a huge difference in the *a*-lattice constant gives rise for strongly compressive strained ZnCdO/ZnO QW structures and hence large polarization charges. The generated built-in electric field (F), which is expected to increase linearly in the lowest order with the Cd concentration [$F(y) = F_0 \cdot y$], strongly affects the optical properties of the QW due to the quantum confined stark effect, as illustrated in Figure 2.3. In a high-field regime, the dominant contribution to the optical transition energy is given by the potential drop across the well [eFd_{w}] (see inset in Figure 2.3 (b)). Hence, the transition energy depends almost linear on the well width (d_{w}) (see Figure 2.3 (a)) and falls below the transition energy of a bulk crystal for wider wells. A more dramatic consequence is the spatial separation of electron and holes by the polarization charges, which is illustrated in Figure 2.3 (b). Especially for wider wells

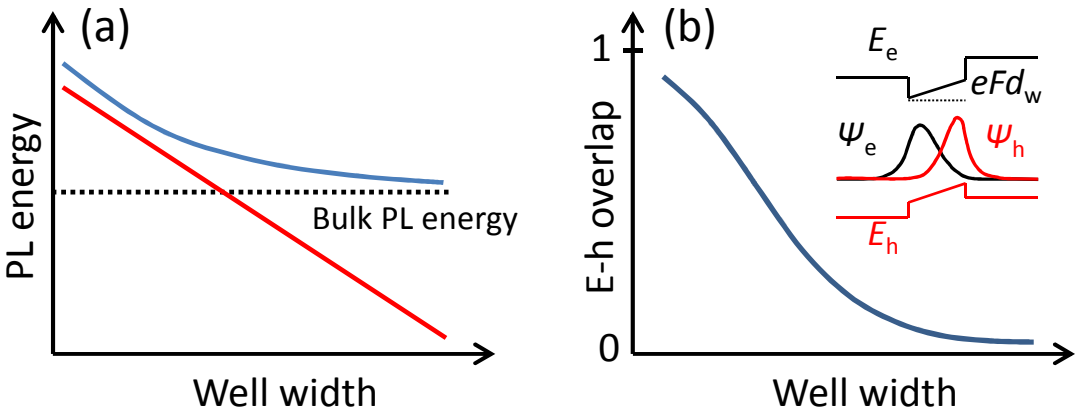

Figure 2.3: Illustration of the effect of built-in electric fields on the optical properties QW structures. (a) Transition energy versus well width for QW structures with (red) and without (blue) polarization fields. Transition energy of the bulk crystal is marked by the dotted line. (b) Electron-hole overlap ($\int \psi_e(z)\psi_h(z)dz$) versus well width. Inset: Conduction (E_e) and valence band (E_h) as well as wave functions of electron (ψ_e) and holes (ψ_h) of a QW structure under the influence of an internal electric field.

a decrease of the transition matrix element and of the excitonic binding energy appear due to the reduced e-h overlap. The carrier lifetimes can become significantly long and the amount of accessible gain very small as a result of the low transition probability. For this reason, screening of the polarization charges under carrier injection is an essential point for light-emitting applications.

Another contribution to the transition energy comes from localization of excitons at minima in the potential landscape, which also reduces the PL energy. Especially for ternary wells this contribution can be very large and might make the identification of polarization fields more difficult. However, for a set of QWs with fixed alloy concentration but different well width, this contribution can be approximated to be constant for all QWs. In particular, this is justified if the PL linewidth across such a sample set changes only smoothly. Moreover, the transition energy of a QW without polarization fields can never fall below that of the pure bulk crystal.

The impact of polarization fields and carrier localization on the optical properties of InGaN/GaN QWs structures has been extensively studied in the past (see, e.g., References [32, 33, 34]). The situation for present ZnO/ZnMgO QWs structures is less clear. Several publications report on the presence of internal electric fields, while there is also a large number of reports on pure quantum size effects in such QWs (see, e.g., [35] and references therein).

2.2. Laser resonators

2.2.1. Fabry-Perot Laser

The standard design of a laser is the Fabry-Perot laser. Here, the optical feedback for lasing is provided by two parallel adjusted mirrors with amplitude reflection coefficients r_1 and r_2, as illustrated in Figure 2.4 (a). In semiconductor lasers, this type of resonator is formed by the end facets of the crystal (produced, e.g., by cleaving or etching) and therefore the laser light comes out of the edge of the structure. The semiconductor-air interface typically provides a facet reflectivity in the range of 0.1 - 0.3. The round-trip condition of the electric field in such a Fabry-Perot cavity of lengths L can be written as:

$$r_1 r_2 e^{2i\tilde{n}k_0 L} = r_1 r_2 e^{gL} e^{2ink_0 L} = 1, \tag{2.9}$$

using the complex refractive index (RI) $\tilde{n} = n - ig/2k_0$ with n, k_0 and g being the real part of the RI, the vacuum wave number and the gain coefficient, respectively. The real part of Equation 2.9 yields the threshold gain condition of a Fabry-Perot laser:

$$g_{\mathrm{th}} = \frac{1}{L} \ln \frac{1}{r_1 r_2}. \tag{2.10}$$

A more precise threshold condition has to account for the optical mode overlap ($\Gamma = \frac{\int_{\mathrm{gain}} E(z)^2 dz}{\int_{-\infty}^{+\infty} E(z)^2 dz}$) with the gain region of the structure and for losses α_{a} in the active material as well as for losses α_{c} in the cladding layer (see Figure 2.4 (b)),

$$\Gamma g_{\mathrm{th}} = \Gamma \alpha_{\mathrm{a}} + (1 - \Gamma)\alpha_{\mathrm{c}} + \frac{1}{L} \ln \frac{1}{r_1 r_2}, \tag{2.11}$$

where Γg_{th} is the modal gain.
The phase condition of a Fabry-Perot laser is obtained from the imaginary part of Equation 2.9 and reads as

$$2nL = m\lambda, \tag{2.12}$$

where m = 1,2,3... is an integer. The mode spacing in the presence of dispersion follows from the phase condition:

$$\Delta\lambda = \frac{\lambda^2}{2L(n - \lambda \frac{\partial n}{\partial \lambda})}. \tag{2.13}$$

Equation 2.11 and 2.12 define the spectral range where lasing can occur. This is exemplified in Figure 2.4 (c). The spectral positions of the longitudinal modes of the Fabry-Perot cavity at which laser oscillation can take place are shown in the lower panel of Figure 2.4. Only those modes which lie in the spectral region of the optical gain and which experience a modal gain larger than the losses can start to lase (middle and upper

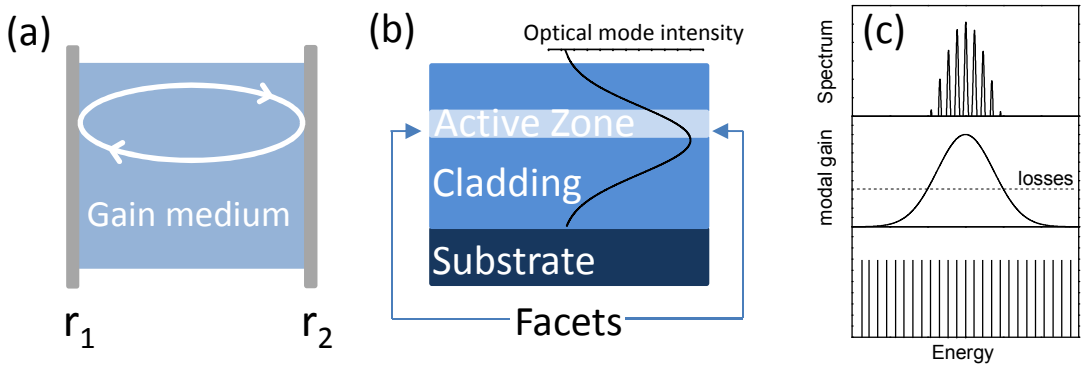

Figure 2.4: Semiconductor Fabry-Perot lasers. (a) Schematic design. (b) Cross section view with cladding layers for improvement of optical mode overlap with the active region. (c) Lower panel: Energies of longitudinal modes of a Fabry-Perot laser. Center panel: modal gain and losses of the same laser. Upper panel: spectrum of allowed laser modes.

panel). However, how many modes and which of the modes can be observed in the experiment depends on the excitation condition (pulsed or continuous wave excitation) as well as on the broadening mechanism of the optical gain (whether homogeneous or inhomogeneous).

2.2.2. Random Laser

The optical feedback for lasing of a random laser is not provided by mirrors but by scatterers. They are randomly distributed in a gain medium or act by themselves as optical amplifiers as illustrated in Figure 2.5. In the first case, the random laser is often constructed out of metal particles diluted in a laser dye. Here the metal particles just act passive by scattering of light. Scatterers which act by themselves as optical amplifier can be fabricated out of semiconductor nanoparticles or powders. Many examples of random laser materials can be found in Reference [36].
The parameters that mainly characterize a random laser are its volume, the number of scatterers as well as their scattering cross section. The scattering cross section of a particle defines the ratio of the rate of scattered energy to incidence irradiance. Therefore, it is a quantity with the dimension of an area. The simplest type of a scatterer is a passive and spherical one. Here, the scattering cross section depends on the wavelength of incident light, on the size and material of the particle as well as on the surrounding medium. The size of the particle influence also the spatial distribution of scattered light. Particles which are much smaller than the wavelength of incident light scatter isotropically, while for larger particles the amplitude of scattered light becomes anisotropic.
For two point scatterers separated by the distance L in a gain medium the threshold gain in a 2-dimensional setting can be derived [37]:

$$g_{\mathrm{th}} = \frac{1}{L} \ln \frac{2\pi L}{\sigma}. \tag{2.14}$$

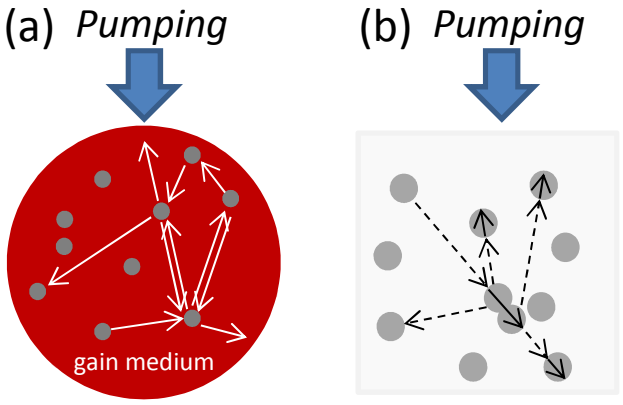

Figure 2.5: Random laser configurations. (a) Passive scatterers embedded in a gain material. (b) Random laser made out of active particles which scatter and amplify light. Arrows indicate manifold of possible light paths. Straight arrow: Propagation through gain material. Dashed arrow: Propagation without amplification.

This equation looks very similar to the threshold condition of the Fabry-Perot laser (Equation 2.10). The amplitude reflection coefficients are now replaced by σ which is the isotropic Rayleigh scattering cross section (in the 2-dimensional setting with dimension of a length). A significant difference is the L-dependence in the natural logarithm which is associated with an increase of the threshold. This dependence is caused by the fact that scattered waves are no longer plane waves but cylindrical waves (or spherical waves in a 3-dimensional system) with spatially decaying amplitude.
In a random laser with many scatterers a detail account for all losses is difficult. The same holds true for the phase of the electric field as the scatterers are randomly distributed. Therefore, the mode spectrum can become very complex and no longer described by simple formulas. A quite elaborated model is required to take these properties into account. For the same reason, the mode spectrum of a random laser can be very sensitive to tiny fluctuations of the excitation power under pulsed pumping. It also depends on the size and shape of the excitation region as well as on the spatial direction of detection. Reviews about random lasers can be found in References [38, 39, 40].

2.2.3. Vertical cavity surface emitting laser and microcavities

According to equation 2.10, the threshold gain of a Fabry-Perot laser can be reduced by either extending the cavity length or by an enhancement of the mirror reflectivity. Because of the relatively low facet reflectivity of a semiconductor Fabry-Perot laser, a long cavity is required (some 100 μm) to meet the threshold condition. Therefore, such a laser exhibits a large number of longitudinal modes.
A VCSEL is a structure which is designed the other way round, i.e., highly reflective mirrors ($R > 0.99$) combined with a very short cavity. A schematic design of a VCSEL structure is shown in Figure 2.6 (a). In such a device, the light is confined in the

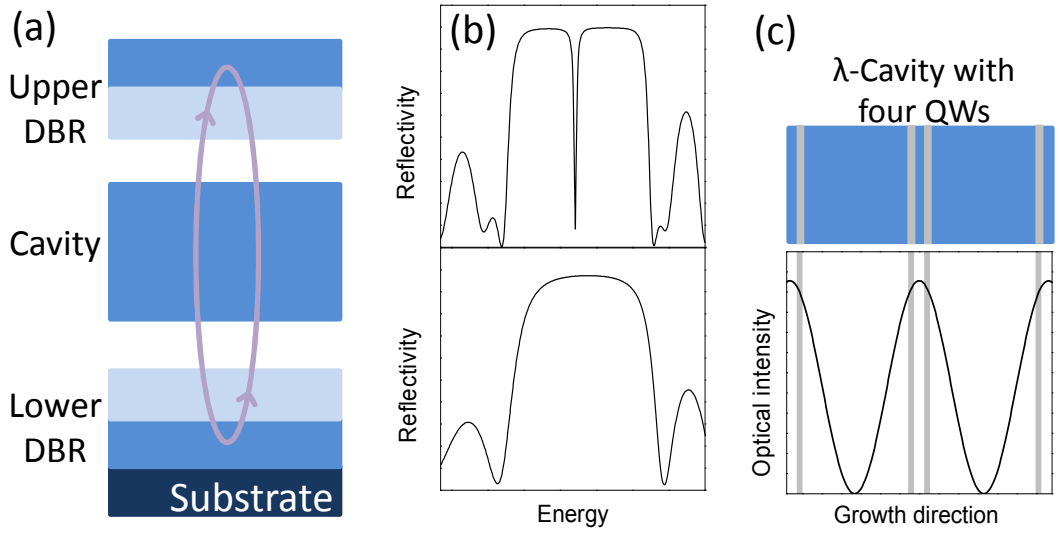

Figure 2.6: Properties of VCSEL devices. (a) Schematic design. (b) Lower panel: Reflectivity of a DBR mirror. Upper panel: Reflectivity of a VCSEL structure. If well designed, the cavity resonance appears in the stopband center. (c) Schematic design of the cavity. The active material is positioned close to the electric field antinodes.

direction parallel to the growth direction and the sample emits from the surface. The cavity which contains the active material, e.g., QWs, is placed in between two highly reflective DBRs. They consist of alternating layers of two materials with different RI. At each interface part of the light is reflected, however at the high RI material the phase of the reflected light is $\lambda/2$-shifted. If the optical thickness of each layer is about one quarter of the wavelength, all reflections interfere constructively and a spectral region of high reflectivity, the so-called stop band, is formed (lower panel in Figure 2.6 (b)). Typically, the length of the cavity is a multiple of λ/n. In this case, the cavity resonances are spaced far apart and there is only one resonance within the stop band of the DBR mirrors (upper panel in Figure 2.6 (b)). The gain material is positioned near the electric field antinodes in the cavity, as shown in Figure 2.6 (c). In general, devices such as the structure shown in Figure 2.6 (a) are called MCs, as the volume of the optical mode is very small. The term VCSEL is directly related to lasing applications of that device. More details about VCSEL devices can be found in many textbooks, e.g., in References [41, 42].

2.2.4. Strong exciton-photon coupling in microcavities

Close to the excitonic resonance (ω_0), the interaction of excitons with light can be well described in terms of a complex dielectric function $\epsilon(\omega) = \epsilon_\mathrm{b}(1+\frac{\Delta_\mathrm{LT}}{\omega_0-\omega-i\gamma_\mathrm{x}})$, with ϵ_b, Δ_LT and γ_x being the background dielectric constant, the longitudinal-transverse splitting and the damping of the exciton, respectively. When the exciton-photon coupling strength (V), which is related to $\Delta_{\mathrm{L}T}$, exceeds the damping of the exciton the system is in the strong coupling regime and a new quasiparticle, the polariton, is formed. Its dispersion exhibits an upper and lower polariton branch, as shown in Figure 2.7 (a). The splitting at the exciton-photon crossover is a direct measure of the coupling strength.
Microcavities are a very good tool to achieve the strong coupling regime even in the case of a relatively large excitonic damping. The reason for this is the reduced modal volume, which strongly enhances the exciton photon interaction, if the cavity mode is brought into resonance with the exciton. Figure 2.7 (b) illustrates the dispersion of the cavity polariton. An essential difference compared to the bulk case is the finite energy at zero in plane wave vector $k_{||}$.
The design of a MC, which shall operate in the strong coupling regime, is actually often identical with the design of a VCSEL. Wether the system is in the strong coupling regime or not depends on the damping of exciton and cavity (γ_c) as well as on the coupling strength, as it will be discussed in the following.
The exciton-photon interaction can be described by a 2×2 matrix Hamiltonian. The eigenvalues of this Hamiltonian in the case of resonance of exciton and cavity mode ($E_\mathrm{x} = E_\mathrm{c}$) are found to be [43]:

$$E_\mathrm{UP,LP} = E_\mathrm{x} - i\frac{\gamma_\mathrm{x}+\gamma_\mathrm{c}}{2} \pm \sqrt{V^2 - \frac{(\gamma_\mathrm{x}-\gamma_\mathrm{c})^2}{2}}. \tag{2.15}$$

From this equation, three different regimes can be defined.

Weak coupling regime:

If $V^2 < \frac{(\gamma_\mathrm{x}-\gamma_\mathrm{c})^2}{2}$ there is only a contribution to the imaginary part of the eigenvalues. Hence, only the damping of the states is affected (Purcell effect). This is the regime of operation of a VCSEL.

Intermediate coupling regime:

The upper (E_UP) and lower (E_LP) polariton branches are energetically split when the condition $V^2 > \frac{(\gamma_\mathrm{x}-\gamma_\mathrm{c})^2}{2}$ is fulfilled. However, this does not necessarily mean that the system is in the strong coupling regime because the condition can be always fulfilled by $\gamma_\mathrm{x} \approx \gamma_\mathrm{c}$ even for a very small exciton-photon coupling strength. If the damping is very large the two branches cannot be distinguished.

Strong coupling regime:

In order to be able to distinguish between the two polariton branches, a splitting larger than $\gamma_x + \gamma_c$ is required. This yields the condition for strong exciton-photon coupling $V^2 > \frac{\gamma_x^2+\gamma_c^2}{2}$.

Figure 2.7 (c) illustrates these three different regimes.
It was pointed out by Savona *et. al* [44] that the condition necessary to obtain an anticrossing in the dispersion relation is different for the transmission, reflectivity and absorption spectrum as well as for the eigenvalues of equation 2.15. While for the latter, the above-mentioned condition $V^2 > \frac{(\gamma_x-\gamma_c)^2}{2}$ has to be fulfilled, $V^2 > \frac{\gamma_c^2+\gamma_x^2}{2}$ is the necessary condition to obtain a splitting in absorption. Hence, an observable splitting in absorption is directly related to the existence of two distinct eigenstates with two distinguishable eigenvalues [45, 46]. The observation of a splitting in transmission alone does not ultimately mean that the system is in the strong coupling regime (see the dashed line in Figure 2.7 (c)).
The optical response of a MC in any of these regimes can be well reproduced by the Transfer-Matrix-Method (for details see Appendix A) using the complex RI of the active zone as the input parameter.
More details about strong exciton-photon coupling in MCs can be found in References [45, 47].

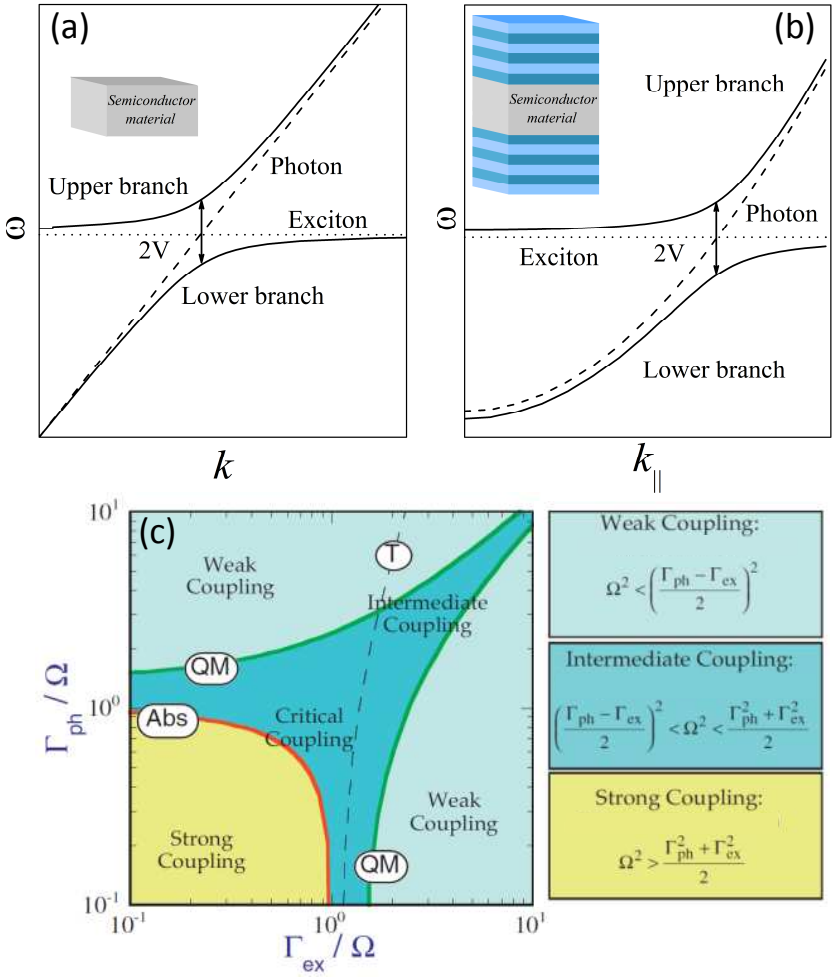

Figure 2.7: Strong coupling of excitons and photons. (a) Schematics of the bulk polariton dispersion $\omega(k)$. Dashed line: uncoupled photon. Dashed dotted line: uncoupled exciton. (b) Schematics of the cavity polariton dispersion $\omega(k_{||})$. Dashed line: uncoupled cavity mode. Dashed dotted line: uncoupled exciton. (c) Map of the weak, strong and intermediate coupling as a function of the linewidths of exciton and cavity. "Abs" denotes the condition to observe a splitting in absorption and "QM" denotes the limit of the weak coupling regime. The dashed line denotes the condition to observe a meaningless splitting in the transmission spectrum alone. For details see text. Note the different notation of the damping of exciton and cavity as well as of the coupling strength. Figure (c) is adapted from [46].

3. Experimental

In this chapter, the fabrication of samples as well as the experimental setups and components employed for their optical investigation are briefly described. Some basic features of the MBE apparatus used for sample growth are presented, followed by a short description of the applied growth procedure. Finally, the components used for optical investigation of the samples are summarized.
At this point, it should be mentioned that there is no direct contribution from the author to the fabrication of the samples. Most of the structures presented in this work were grown by Dr. Sergey Sadofiev and some by Dr. Matthias Brandt. Hence, a very detailed description of the specific MBE apparatus and the growth conditions can be found in the PhD thesis of Dr. Sergey Sadofiev entitled "Radical-source molecular beam epitaxy of ZnO-based heterostructures" [13].

3.1. Sample growth by molecular beam epitaxy

3.1.1. Molecular beam epitaxy apparatus

The MBE machine (DCA-450) used for fabrication of the sample is equipped with a cryo-pump, an ion-pump, and a Ti sublimation pump maintaining a residual gas background pressure in the 10^{-10} Torr range. The whole growth area is surrounded by two cryopanels for liquid nitrogen. The growth chamber itself contains DCA hot-lip effusion cells (eight cells can be mounted) for evaporation of elemental Zn (6N), Cd (6N) and Mg (5N), while Oxygen (5.5N) is provided via an Addon radio frequency plasma source after additional gas purification. Each effusion cell is equipped with a shutter to interrupt the beam between source and substrate. The gas flow rate is controlled by a leak valve (more recently this system has been switched to mass-flow control). The growth stoichiometry is adjusted by changing the metal molecular flux density. The beam equivalent pressures of these fluxes are measured by a nude ionization gauge placed in front of the substrate. Both sides polished, chemically degreased *a*-plane sapphire templates are used as substrates. They are attached by In to a Mo holder and degassed on a heating stage at 560° C for about 1 h and then exposed to oxygen plasma (5 min) prior to film deposition. The growth temperature (T_g) is controlled by a thermocouple placed behind the holder and by an infrared pyrometer. The growth process is monitored *in situ* by reflection high-energy electron diffraction (RHEED). The apparatus is equipped with a system for rotation of the sample during growth. However, all samples presented in the remainder of this thesis are grown without sample rotation.

3.1.2. Growth conditions for ZnMgO- and ZnCdO-based alloys and heterostructures

ZnMgO [48, 49]

It was found that growth temperatures between 310-370 °C and a slightly metal-rich environment provide optimum results for growth of ZnMgO-films. In this way layer by layer growth can be accomplished up to the phase-separation limit occurring at a Mg mole fraction of about $x = 0.40$. The surface morphology of an as-grown ZnMgO layer can be dramatically improved by short-time (∼5 min) annealing at about 560 °C. The annealing step can be carried out at any stage of the ZnMgO-film deposition. When the standard growth procedure is used, the deposition of ZnO/ZnMgO QWs starts from such a smoothed surface. Typically, the growth temperature of the QW can be varied in a range of T_g = (300-470)°C.

ZnCdO [50]

The epitaxial regime required for achieving high-quality ZnCdO material is quite different from that for ZnMgO or ZnO. It turned out that low growth temperatures in the range of T_g = (100-150)°C in combination with strong oxygen excess enable the growth of single-phase wurtzite-type ZnCdO-layers up to a Cd concentration of $y = 0.32$. Despite such low growth temperatures layer-by-layer growth occurs, and a smooth surface morphology is obtained making the fabrication of ZnCdO/ZnO QW structures possible. A post growth annealing step (5 h at 350 °C) is performed on epilayers or QW structures in order to enhance the radiative efficiency of the low-temperature grown structures by more than one order of magnitude.

3.2. Experimental setups

3.2.1. Excitation sources

Low density excitation

The low-density PL is excited by the 355 nm frequency tripled output of a Nd:YVO_4 laser which produces pulses of about 13 ps at a repetition rate of 80.6 MHz. The maximum average UV pump power is about 1 W.
The frequency doubled output of a 2 ps/80.6 MHz DCM dye laser (which is pumped by the second harmonic of the Nd:YVO_4 laser) is also used for excitation. The average UV pump power in a wavelength range from 310-350 nm is some mW.

High density excitation

Pulsed pumping at higher excitation levels is performed by an excimer laser pumped dye laser system. The LEXtra 50 excimer laser (XeCl-based) emits 20 ns long pulses at a wavelength of 308 nm with a maximum repetition rate of 30 Hz. Pumping of selective laser dyes (like p-Terphenyl, DMQ and QUI) enables excitation of the sample in a wavelength range from about 335 nm to 400 nm. Typically, the maximum energy per excitation pulse is some 100 μJ.
Another source for excitation is a 500 ps N_2-laser with an energy of 200 μJ per excitation pulse. The excitation wavelength is 337 nm and the maximum repetition rate is 60 Hz.

3.2.2. Detection systems

Time integrated detection

Time integrated emission spectra are recorded by a N_2 cooled charge coupled device (CCD) detector with a 1024x256 pixel array. Two different types of monochromators are used for dispersion of the detected light. Spectrally broad emission is dispersed by a 0.5 m focal-length monochromator, which is equipped with a 300 grooves/mm grating. If necessary the grating can be switched to a 1800 grooves/mm grating. The highest resolution is obtained by a 1.15 m focal-length monochromator equipped with a 1800 grooves/mm grating. In conjunction with the CCD detector a spectral resolution of 0.03 nm is achieved.

Time resolved detection

For performance of time resolved measurements a microchannel plate photomultiplier is mounted on a double-monochromator in subtractive configuration. The PL transients are obtained by a time correlated single photon counting system. Standardly, the 80.6 MHz system described above is used for low-density excitation of the sample. If the lifetime is too long to measure it with 80.6 MHz repetition rate, an acousto-optical modulator is used to lower the repetition rate.
In the high density excitation regime, i.e. the repetition rate is only some 10 Hz, the signal is detected by a microchannel plate photomultiplier and a digital oscilloscope.

Goniometer setup for transmission and reflectivity measurements

Angle resolved reflectivity and transmission are recorded by a home-built goniometer setup. The sample is mounted in a transmission helium flow cryostat which allows for temperature control between 4 K and 300 K. The cryostat is attached on a rotation stage (rotation angle θ) enabling precise rotation about the sample axis. The angular resolution is $\pm$ 1°. The reflected or transmitted light is collected (reflected light at 2θ and transmitted light at 180°) by an optical fiber which can be rotated around the sample axis at a fixed distance (some cm) as depicted in Figure 3.1. The light is coupled into a monochromator, and spectra are recorded by a CCD. The setup allows for simultaneous measurement of reflectivity and transmission at a given angle at identical

sample positions. The size of the cryostat windows limits θ to 40°. A halogen tungsten lamp is used as white-light source.

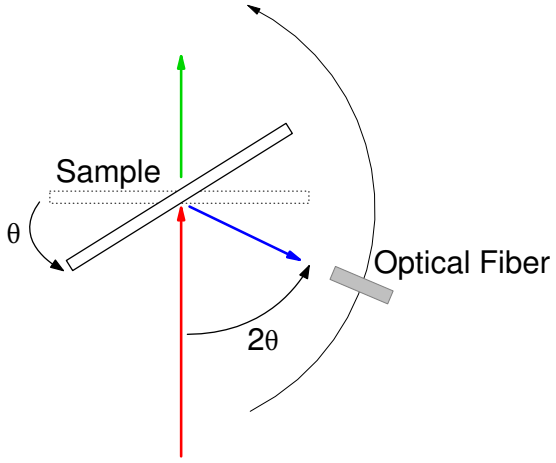

Figure 3.1: Functionality of the home-built goniometer setup. Arrows: incident light (red), reflected light (blue) and transmitted light (green).

4. Green-wavelength lasing of ZnCdO/ZnO multiple quantum well structures

4.1. Introduction

Despite a huge potential market for a green semiconductor laser, such a laser is not yet commercially available. Possible applications include laser television and laser based micro-projectors, which can create a bright, full color and high-resolution image by combining blue, green and red laser light [51]. So far, laser based mobile micro-projectors (e.g., the "Laser Pico Projector") use blue and red semiconductor lasers as well as a green laser source based on second harmonic generation. Here, the radiation is created by frequency doubling of the infrared output from a solid-state laser in a nonlinear medium. Beside the substantial energy loss, the difficulty to reach high degrees of miniaturization and integration represents a serious disadvantage of the frequency doubling scheme.
For a while, in the 1990s, ZnSe-based heterostructures have been investigated with regard to laser emission in the blue/green spectral range. Though electrically driven laser action succeeded, defects appearing during operation limited the device lifetime so that a commercial level was never reached [52]. In parallel, group-III nitrides went into the focus. The InGaN alloy has made it possible to manufacture light-emitting devices covering the whole visible spectral range [53].
When this work was started, lasing of InGaN stopped for quite a long time at about 488 nm even under optical pumping and an extension to longer wavelengths seemed to be very challenging. Considerable efforts have been undertaken by market-leading companies like Nichia and Osram Opto Semiconductors to shift the emission to longer wavelengths. In 2009/10 lasing of InGaN/GaN heterostructures in the green spectral range under current injection has been demonstrated. A prerequisite was the growth of high-quality InGaN/GaN QWs on non- and semi-polar plane GaN substrates, avoiding strong build-in electric fields [54, 55, 56]. However, demonstration of green-wavelength lasing succeeded also for optimum designed QWs with improved material quality grown on polar *c*-plane GaN substrates [57, 58]. Nevertheless, a commercially availably green laser made of InGaN is still elusive.
In this chapter, it is shown that the ternary ZnCdO is another semiconductor capable of green-wavelength lasing. Lasing of ZnCdO/ZnO QW structures, grown on standard *a*-plane sapphire substrates, is demonstrated up to a wavelength of 510 nm. A prerequisite is the fabrication of high-quality QW structures combined with the understanding of their polarization properties enabling optimized sample design. Most of the results of this chapter have been already published in References [7, 59, 60, 61].

4.2. ZnCdO/ZnO quantum well structures

The QW structures are grown by MBE on the *a*-plane of sapphire as described in Section 3.1. During growth, the nominal layer thickness is precisely controlled by the number of RHEED oscillations, as shown in Figure 4.1 (a). Therefore, the well width is very accurately known. Moreover, growth under strong O-rich conditions allows for the direct determination of the ZnCdO ternary alloy composition in the QW region from the variation of the growth rate between ZnO and ZnCdO (see the number of oscillations per second for ZnO and ZnCdO) [60]. However, the relative error in the Cadmium concentration is about 5-10 % as it follows from a comparison with the composition of reference epilayers elaborated by energy-dispersive X-ray analysis. In this way, fabrication of single QW (SQW) and MQW structures in a wide range of structural designs is possible. Figure 4.1 (b) shows exemplarily a transmission electron microscopy image of a 10-period MQW structure. The presence of continuous wells with a high degree of uniformity is clearly visible.

At the low temperatures required for growth of ZnCdO, lattice imperfections created by limited desorption of adatoms and restricted migration lengths can degrade the radiative efficiency of the structures. As known from other heteroepitaxial systems, post-growth annealing is a useful procedure to improve the crystalline quality and to enhance the radiative efficiency (see, e.g., Ga(As,N) [62] and ZnCdSe [63]). Care has to be taken when applying such a procedure to ZnCdO alloys because the wurtzite phase might not be stable up to very high temperatures. For annealing of QW structures, the removal of defects is also accompanied with a widening of the wells through the diffusion of Cd into the ZnO barriers. The problem of Cd diffusion at higher temperatures is also known from other low-dimensional heterostructures (see, e.g., Reference [64] for CdTe/ZnTe quantum dots and Reference [65] for ZnCdSe/ZnSe QWs).

The impact of annealing under ultra-high-vacuum conditions on the PL properties of a ZnCdO/ZnO SQW structure is shown in Figure 4.1 (c). Annealing at $T_A = 350$ °C for 5 h enhances the band gap-related emission by more than one order of magnitude. At the same time, defect emission pre-existing in the as-grown sample is suppressed. Higher annealing temperatures further increase the quantum yield. However, the high-energy shift of the emission maximum manifests the decrease of the Cd concentration in the well through interdiffusion. This shift is only about 30 meV at moderate annealing temperatures, but it can reach several hundred meV at higher temperatures (red curve in Figure 4.1 (c)). When aiming at QW structures emitting in the green-wavelength range or at even longer wavelengths, the increase of the quantum yield and the high-energy shift of the QW emission must be balanced. In this regard, a temperature of $T_A = 350$ °C seems to be a good trade-off. No signature of a wurtzite-cubic phase transition is found on samples annealed for 5 h at $T_A = 520$ °C, demonstrating stability of the wurtzite-phase up to at least this temperature level.

More details about growth of ZnCdO/ZnO QWs and the impact of annealing can be found in Reference [60]. Studies on the influence of rapid thermal annealing on the PL of ZnCdO/ZnO MQWs and annealing studies on ZnO/ZnCdO/ZnO double heterostructures are found in Reference [66] and [67], respectively.

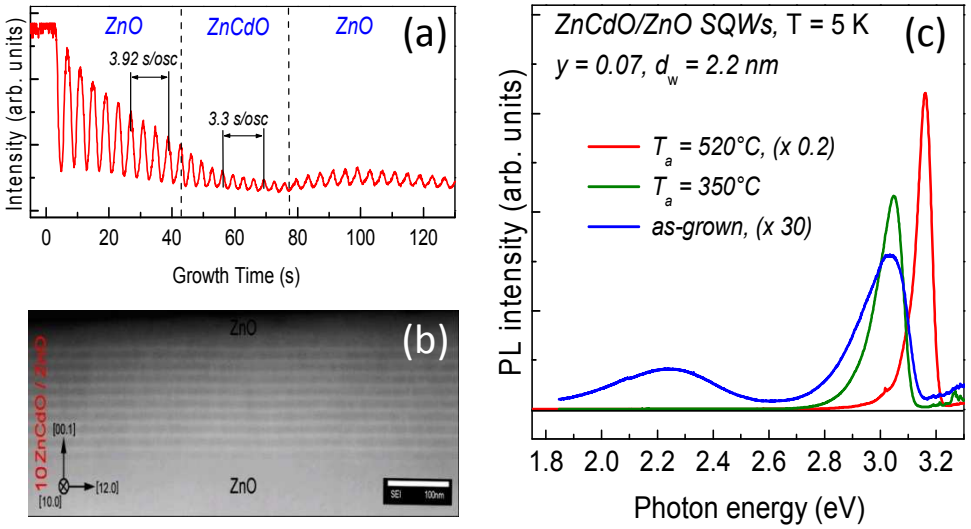

Figure 4.1: Fabrication of ZnCdO/ZnO QW structures. (a) RHEED oscillations recorded during growth of a typical SQW structure at a growth temperature of 150 °C. Figure is taken from Reference [60]. (b) Transmission electron microscopy image of a 10-period $d_w = 2.4$ nm and $y = 0.15$ ZnCdO/ZnO MQW (Figure is provided by I. Häusler, H. Kirmse, and W. Neumann, Humboldt Universität zu Berlin). (c) PL of a 2.2-nm-thick ZnCdO/ZnO SQW structure ($y = 0.07$) before (blue) and after annealing at $T_A = 350$ °C (green) and 520 °C (red).

Optical properties: Polarization fields

The optical properties of ZnCdO/ZnO QWs are investigated on a set of SQWs with Cd concentrations in the range of $y = 0.06$ - 0.23 and a well width between $d_w = 1.2$ - 5.4 nm at a temperature of $T = 5$ K. The QW is embedded between a 500-nm-thick ZnO buffer and a 30-nm-thick ZnO cap layer. The excitation is always above the ZnO band gap energy. The low-density PL is excited by the frequency tripled output of the Nd:YVO_4 laser, while time resolved transients are excited by the frequency doubled DCM dye laser output. PL data at higher excitation intensities in time-integrated mode are acquired by the excimer laser pumped dye laser system. Time-resolved measurements in this regime are performed with 0.5 ns pulses of the N_2-laser.
Time integrated PL data in the low-density excitation regime are collected in Figure 4.2. The PL spectrum of the SQW structures consists of emission features from the ZnO barrier material and the spectrally broader well emission situated on the low-energy side, as depicted in Figure 4.2 (a) and (c). Though the excited ZnO volume is at least one order of magnitude larger, the total yield of the well PL is clearly stronger signifying efficient carrier capture by the SQW. The spectral position of the emission can be tuned by both, well width (a) and Cadmium content (c). The PL is spectrally broad (100-200 meV) indicating that localized excitons are involved in the radiative recombination, which is, in view of the small excitonic Bohr radius, naturally expected. The fact that even the PL of ZnCdO epilayers is broadened by more than 100 meV and markedly red-shifted with respect to the absorption edge [50] signifies that most likely compositional fluctuations

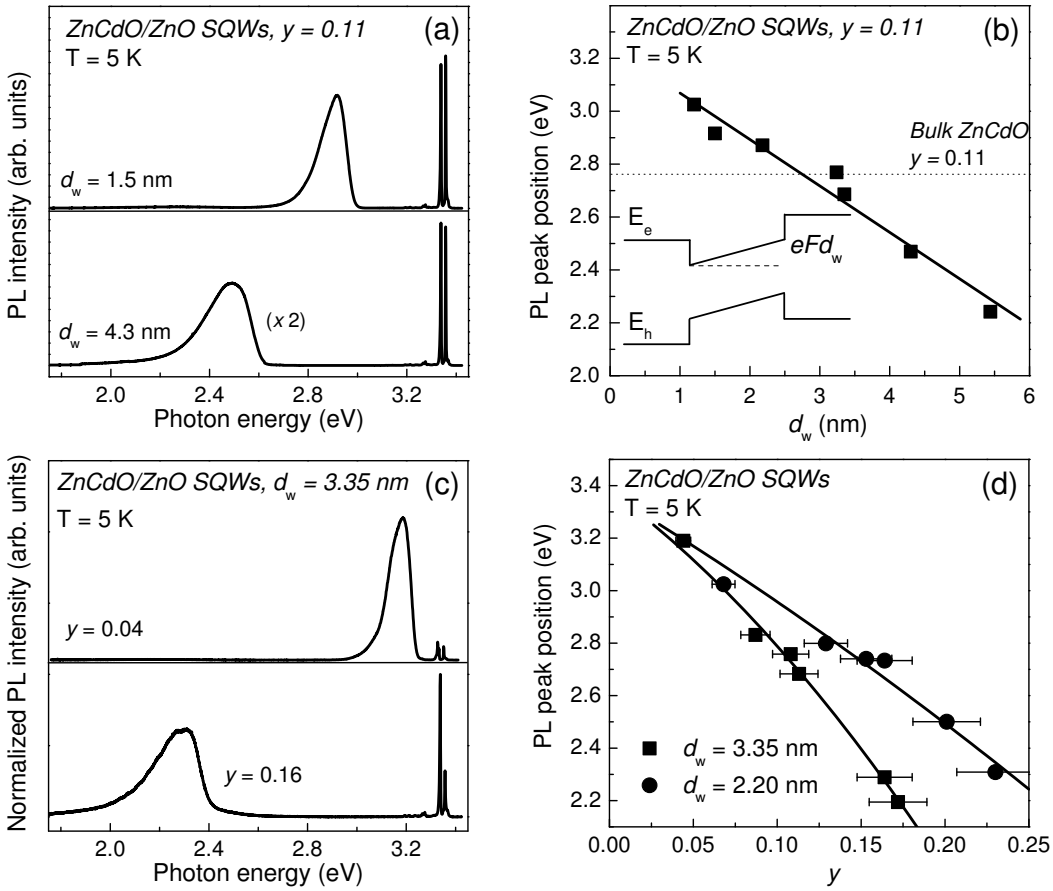

Figure 4.2: PL data of ZnCdO/ZnO SQW structures. (a) Overview spectra of two structures with a Cd content of $y = 0.11$ and different well width of $d_\mathrm{w} = 1.5$ and 4.3 nm, respectively. (b) Steady-state PL peak energy versus well width of a set of SQWs ($y = 0.11$). The line represents the slope given by the potential drop across the SQW $eF = 1.75{\cdot}10^8$ eV/m as schematized in the inset. (c) Overview spectra of two structures with a well width of $d_\mathrm{w} = 3.35$ nm and different Cd content of $y = 0.04$ and 0.16, respectively. (d) PL peak energy versus Cd concentration at fixed well width of $d_\mathrm{w} = 2.2$ and 3.35 nm, respectively. The lines are to guide the eye. The excitation intensity is $I = 500$ mW/cm^2 in (a) and (c) and 10 mW/cm^2 in (b) and (d).

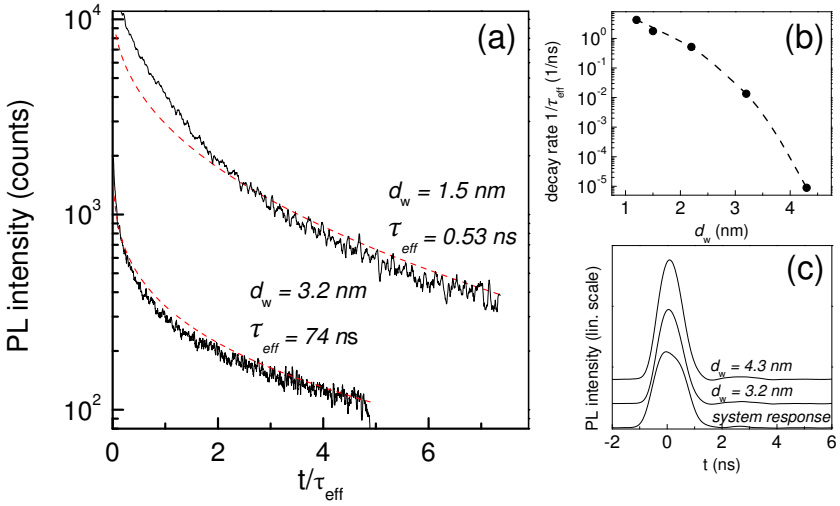

Figure 4.3: Time-resolved PL data of ZnCdO/ZnO SQW structures ($y = 0.11$) in the low- and high-density excitation regime. (a) Exemplary PL transients in the low-density excitation regime plotted in units of characteristic time τ_{eff} (see text). (b) Inverse lifetime versus well width extracted from these transients. (c) Transients taken at the PL peak in the high-density regime in comparison with the system response. The decay transients can be hardly separated from the experimental response to the 500-ps pulses of the N_2 laser used for excitation.

play a leading role. However, micro-optical studies with a resolution of 1 μm^2 have not uncovered discrete emission features, on both epilayers and QW structures.
In the low-density excitation regime ($I = 10$ mW/cm^2), a huge red-shift of the spectral position of the QW PL is observed when the well width is increased from 1.2 to 5.4 nm. The shift is in good approximation a linear function of d_{w}, as can be seen from the plot in Figure 4.2 (b). A similar behavior is observed when plotting the PL position versus the Cd concentration at fixed well width (Figure 4.2 (d)), albeit a weak nonlinearity at higher y appears. Results of time-resolved measurements are collected in Figure 4.3. They reveal that the red-shift of the QW emission is accompanied by a strong increase of the carrier lifetime from about 500 ps up to the 100 μs range (panel (a) and (b)). The PL decays non-exponentially, which is generally observed in heterostructures with strong internal fields and has been attributed to a time shift of the transition energy or a quite complex localization dynamics [34, 68]. When fitting the PL transients with a stretched exponential function $I(t)/I(0) = \exp(-t^\kappa/\tau^\kappa)$ the characteristic lifetime can be determined from the area under the curve $\tau_{\text{eff}} = \int_0^\infty \mathrm{d}t\ I(t)/I(0) = \Gamma(1/\kappa)\ \tau/\kappa$. Despite the extremely long lifetime, non-radiative processes are obviously not notably enhanced. As can be seen in Figure 4.2 (a), the yield of the 4.3 nm wide SQW is only reduced by a factor of 1.5 relative to the 1.5 nm structure.
When the pump intensity is increased, the PL of wider wells undergoes a blue-shift of several hundred meV, as shown in Figure 4.4. The shift begins already at low excitation intensities, but it is much stronger in the 10 kW/cm^2 excitation range. Even in this regime, the PL lines are inhomogeneously broadened at a 100-meV scale (see inset in

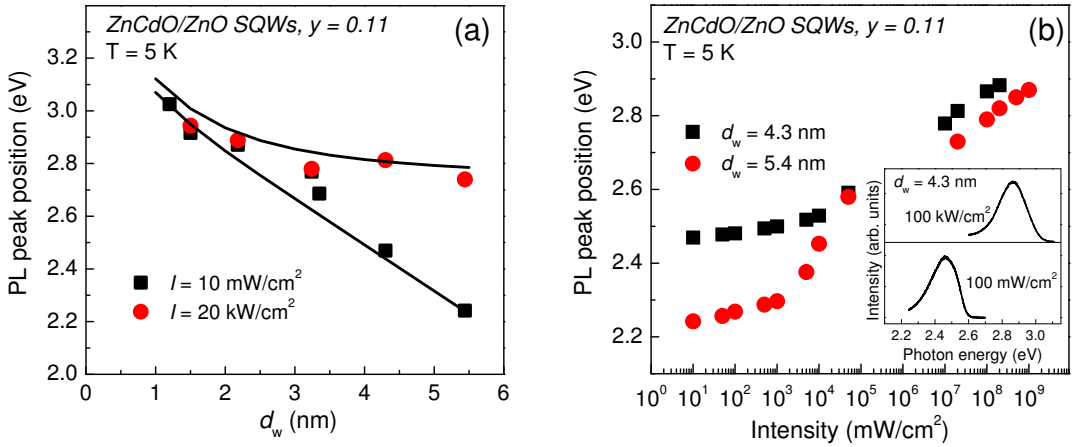

Figure 4.4: The effect of optical excitation on the PL from ZnCdO/ZnO SQWs ($y = 0.11$). (a) PL peak position at low and high excitation versus well width. The lines are calculated energies for wells with (lower) and without (upper) polarization field. (b) Peak position versus excitation intensity for structures with $d_w = 4.3$ nm and 5.4 nm. Pulsed pumping is used at about 10 kW/cm^2 and beyond. Inset: PL of the $d_w = 4.3$ nm SQW at $I = 100$ mW/cm^2 and $I = 100$ kW/cm^2.

Figure 4.4 b). Carrier localization is thus an inherent feature of the ZnCdO/ZnO QW structures. No saturation of the high-energy shift appears up to excitation levels of 1 MW/cm^2. At the same time, the PL decay speeds up by orders of magnitude and approaches the 100-ps time scale (Figure 4.3 (c)).
All these findings are fully consistent with the presence of strong built-in electric fields, where the dominant contribution to the PL energy is given by the potential drop across the well. Therefore, irrespective of the band structure details, the built-in electric field can be directly estimated from the experimental data. The slope of the line in Figure 4.2 (b) provides $F/y = (1.6 \pm 0.2) \cdot 10^9$ V/m. The long carrier lifetimes of wider wells appear due to the strongly reduced e-h overlap. Screening of the polarization fields, and hence, recovery of strong overlap between electron and hole wave function, is manifested by the pump induced blue-shift of the PL as well as by the speed up of the radiative decay. Quite similar values for F have been found for the InGaN/GaN heterosystem [32, 33, 34]. Recently, a slightly lower value for the built-in electric field of ZnCdO/ZnO QWs has been found [69].
For detailed understanding, the system of coupled Schrödinger and Poisson equations:

$$[-\frac{\hbar^2}{2m_\alpha}\frac{\partial^2}{\partial z^2} + E_\alpha(z) + e_\alpha\phi(z)]\psi_{\alpha i}(z) = E_{\alpha i}\psi_{\alpha i}(z) \tag{4.1}$$

$$-\frac{\partial^2}{\partial z^2}\phi(z) = F[\delta(z-d) - \delta(zd)] + \sum_\alpha \frac{e_\alpha n_\alpha(z)}{\epsilon_0\epsilon} \tag{4.2}$$

$$n_\alpha(z) = N_\alpha \sum_i |\psi_{\alpha i}(z)|^2 \ln[1 + \exp\frac{\mu_\alpha - E_{\alpha i}}{k_B T}] \tag{4.3}$$

is solved numerically [70] with boundary conditions $\phi'(\pm\infty) = 0$ (charge neutrality) for the electrostatic potential. The index α = e,h refers to electron or hole, while i enumerates the quantum-confined states of the respective carrier type with $N_\alpha = \nu_\alpha m_\alpha k_\mathrm{B} T/\pi\hbar^2$, mass m_α, band degeneracy ν_α, and chemical potential μ_α. A quantitative comparison with the experimental PL energies requires knowledge of the discontinuities of the band edges which are not precisely known. For the excitonic band gap of wurtzite ZnCdO, quite conflicting relations have been put forward so far [12, 71]. Photoelectron spectroscopy has provided a relative band-offset of $\Delta E_\mathrm{h}/\Delta E_\mathrm{e} = 36/64$ for a composition of $y = 0.05$ [72]. Further uncertainties result from the carrier masses and localization effects. In addition, the theoretical model ignores the electron-hole Coulomb interaction and assumes rectangularly shaped wells. However, all these factors drop behind the huge field-induced energy changes in wider wells at sufficiently high Cd concentrations making an analysis in the above frame meaningful.

First, the ground-state transition energies of the unexcited well ($n_\mathrm{e} = n_\mathrm{h} = 0$) are calculated with and without the experimentally determined polarization field ($\phi = 0$ or $\phi = F(y)z$ in the well). For the relative band edge offset of $\Delta E_\mathrm{h}/\Delta E_\mathrm{e} = 36/64$ and the ZnO masses ($m_\mathrm{e} = 0.28m_0$ and $m_\mathrm{h} = 0.59m_0$) [8], a good agreement with the experimental results in Figure 4.4 (a) is achieved using a band gap of $E_\mathrm{g}(0.11) = 2.9$ eV and subtracting from the calculated transition energies $E_{00} = E_{\mathrm{e}0} + E_{\mathrm{h}0}$ a constant value of 160 meV comprising both localization and exciton binding energy. Such assumption, also used for explaining findings for InGaN/GaN heterostructures [34], is justified by the fact that the PL linewidth changes only smoothly across the sample set.

Results of the full numerical solution are collected in Figure 4.5. The sheet density

$$N = \int_{-\infty}^{\infty} \mathrm{d}z \; n_\alpha(z) \tag{4.4}$$

of photoexcited carriers (or the total chemical potential $\mu = \mu_\mathrm{e} + \mu_\mathrm{h}$) is the parameter determining the excitation level in the calculations. The plots in Figure 4.5 (a) show that E_{00} high-energy shifts initially steeply, but approaches a saturation level when N exceeds the sheet density $N_\mathrm{p} = \epsilon\epsilon_0 F/e$ of polarization charges. At low densities before saturation, there is only one bound state for both electron and hole. The wavefunctions are located in the narrow triangular potential dips at the well edges, their overlap is thus very small, as shown in Figure 4.5 (c). E_{00} undergoes the anticipated low-energy drop as a function of the well width (Figure 4.5 (b)). At high densities ($N > N_\mathrm{p}$), the polarization charges become rapidly screened and a flat-band situation with several occupied subbands is established (Figure 4.5 (d)). Figure 4.5 (b) shows that E_{00} at high densities resembles indeed very well the energy of a fictive SQW with no polarization field under low-excitation.

For light-emitting applications, the recovery of flat-band conditions under carrier injection is an essential point. The densities of some 10^{13} cm^{-2} predicted theoretically are high. However, the long lifetimes at low injection levels admit the generation of such densities even under moderate excitation. Thus, effective screening of the polarization fields by photogenerated carriers occurs already at excitation in the 10 kW/cm^2 range.

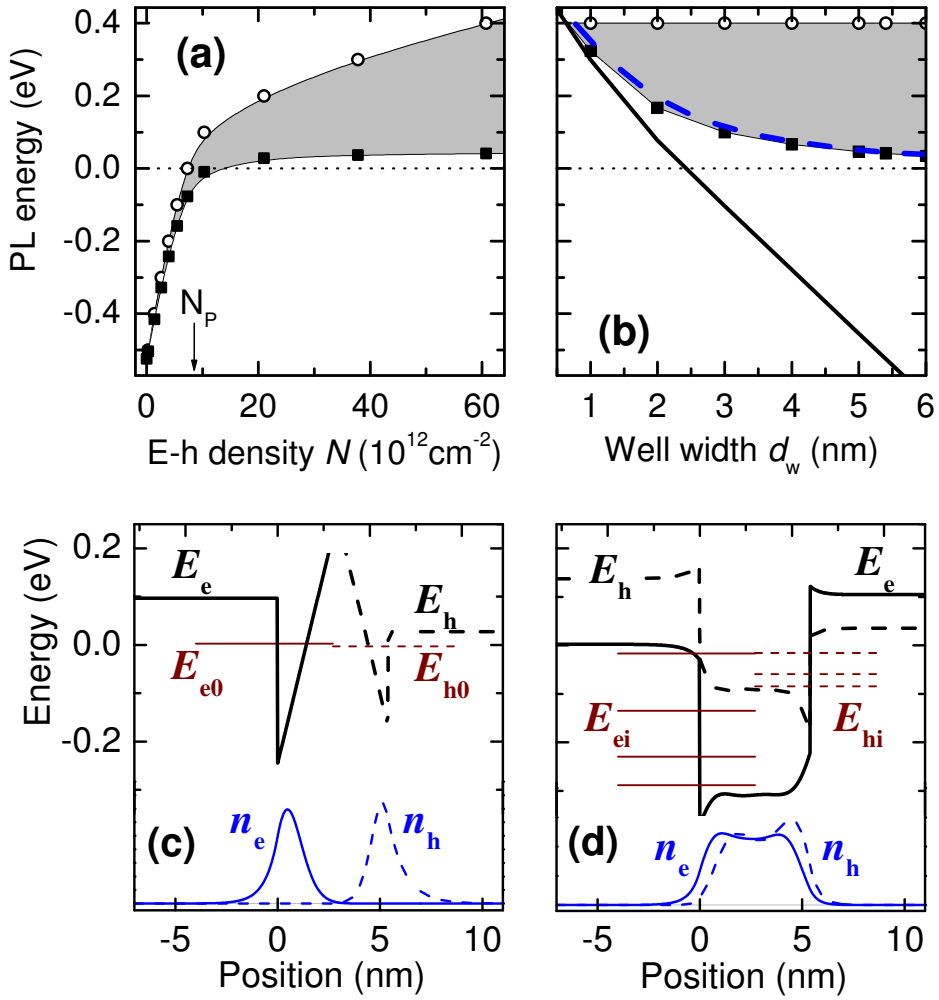

Figure 4.5: Screening scenario calculated by self-consistent numerical solution of the Schrödinger-Poisson equations. (a) Ground-state transition energy E_{00} (squares) and chemical potential μ (circles) versus density N of photoexcited carriers of a $d_{\mathrm{w}} = 5.4$ nm SQW. The energy origin is defined by the bulk energy-gap of the well material. (b) Ground-state transition energy versus well width without excitation (solid black) and under high excitation (squares) with $\mu = 0.4$ eV (circles). For comparison the dashed blue curve represents E_{00} at zero-field and no excitation. (c) and (d) band diagrams E_α, particle densities n_α, and occupied subband levels $E_{\alpha i}$ for electrons (solid) and holes (dashed) of a $d_{\mathrm{w}} = 5.4$ nm SQW. Energies are measured relative to the respective chemical potential μ_α. Densities are in arbitrary units. Parameters: $\epsilon = 8.75$ and $F = 1.75 \cdot 10^8$ V/m, (c) $N = 10^8$ cm^{-2} and (d) $N = 6 \cdot 10^{13}$ cm^{-2}.

Consideration for green-wavelength lasing of ZnCdO/ZnO quantum well structures

In contrast to LEDs, the injected carrier density for LDs has to be very high in order to achieve population inversion and to meet the gain loss condition. Obviously, a Cd concentration of $y = 0.11$ is not sufficient for an emission of a ZnCdO/ZnO QW in the green spectral range at higher injection levels. In order to shift the PL to longer wavelengths, the Cd concentration in the well has to be increased, making the influence of the polarization charges even more critical. In this context, the question arises of how to design a green emitting ZnCdO/ZnO QW structure, which provides a strong e-h overlap at minimized carrier densities. For this reason, a screening scenario of a fictive set of ZnCdO/ZnO SQWs is investigated theoretically by the model presented above. As mentioned already before, several parameters of the heterosystem are not precisely known, which makes an exact calculation of the transition energy impossible. However, the dominant field-induced energy change can be treated adequately, giving rise for a good qualitative picture of the overall situation. This should allow for exclusion of deficient designs.
In the calculations, a Cd concentration of $y = 0.20$ is chosen resulting in an electric field of about $F = 3.2 \cdot 10^8$ V/m. A reasonable value of $E_g(0.20) = 2.6$ eV and a constant value of 200 meV comprising both localization and exciton binding energy is assumed (see transmission and PL data of a ZnCdO epilayer with $y = 0.21$ in Reference [50]). The remaining parameters are identical to the previous case.
In Figure 4.6 (a) the sheet density of excited carriers (left axis) necessary to recover an electron-hole overlap of 0.6 is plotted for ZnCdO SQWs of different width together with the corresponding transition energies of these wells (right axis). The unexcited transition energies of potential non-polar structures are also drawn in Figure 4.6 (a) (right axis). An overlap of 0.6 is chosen because it should represent a situation where the transition probability is no longer dominated by the presence of polarization fields. For wells thinner than 2 nm, the e-h overlap is already larger than 0.6 even without screening of the polarization charges. Hence, for a 2 nm well the required carrier density of $6{\cdot}10^{12}$ cm^{-2} is relatively low. For wider wells, the density increases only moderately, especially when the injected carrier density exceeds the polarization charge density (marked by the arrow). The required carrier density of a 5 nm well is five times larger than that of the 2 nm well.
At this point, one could conclude that wells thinner than 2.5 nm are well suited. However, their emission is blue-shifted compared to thicker wells. The total difference in transition energy between a 2 nm and a 5 nm well is about 65 meV (13 nm). Even the emission of the 3.5 nm SQW is still red-shifted by about 50 meV (10.5 nm). In this context, such a well seems to be a good trade-off between a reduced transition energy and a lower carrier density of $2{\cdot}10^{13}$ cm^{-2} necessary for robust e-h overlap. Of course, a higher Cd content in thinner wells can compensate the difference of the transition energies. However, even the growth of single-phase epilayers with Cd concentrations beyond 20 % is a challenge in itself and degradation of material quality and an enhancement of the inhomogeneous broadening are a natural consequence. Following the compositional dependence of the band gap energy in Reference [12] it can be calculated that a red-shift

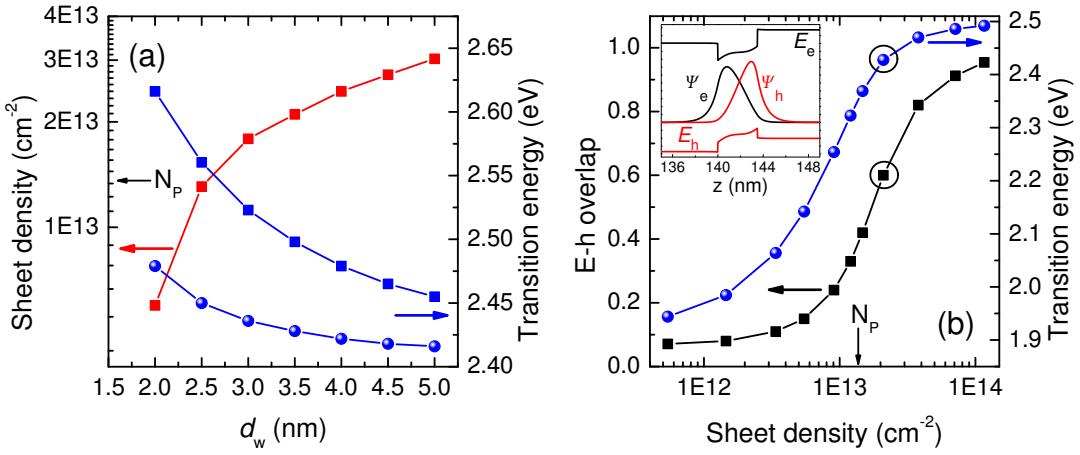

Figure 4.6: Screening scenario of ZnCdO/ZnO SQWs with a large Cd content of $y = 0.2$. (a) Density of photoexcited carriers (red-squared line, left axis) required for regeneration of an electron-hole overlap of 0.6 and the corresponding ground-state transition energy (blue-dotted line, right axis) versus well width. The ground-state transition energies of potential non-polar SQWs are also shown (blue-squared line, right axis). (b) Electron-hole overlap (black-squared line, left axis) and ground-state transition energy (blue-dotted line, right axis) versus density of photoexcited carriers of a $d_w = 3.5$ nm ZnCdO/ZnO SQW. The inset shows conduction and valence band as well as the wavefunctions of electron and hole at the injection level marked by black circles.

of the emission of the 2 nm well by 60 meV requires an enhancement of the Cd mole fraction by about 0.04.

For the same reason, the presence of polarization fields has also a positive effect. Comparing the emission energies of QWs with partly screened polarization charges (blue-dotted line) and without polarization charges (blue-squared line) in Figure 4.6 (a), it follows that green-emitting non-polar ZnCdO/ZnO QW structures require a higher Cd content. Even for the 5 nm well the Cd mole fraction has to be increased by about 0.03. Non-polar QW structures with reduced quantum confinement, i.e., wells thicker than 5 nm, might be possible. However, the large strain caused by the different lattice constants of the barrier and well material can produce additional defects in thick wells.

The relatively large difference of the emission energies between polar and non-polar structures shown in Figure 4.6 (a) becomes clearer by examination of the band structure of a 3.5 nm well with partly screened polarization charges (inset in Figure 4.6 (b)). Although a strong e-h overlap of 0.6 has been restored, a potential drop across the well is still present reducing the overall transition energy by almost 100 meV. The full screening scenario of this well is shown in Figure 4.6 (b). At low injection levels, the e-h overlap is below 0.1 and the QW emits in the red spectral range. When the density of injected carriers approaches the polarization charge density, the transition energy as well as the e-h overlap increase rapidly. If the carrier density is about five times larger than the polarization charge density, the e-h overlap is almost totally restored and the high-energy shift of the emission stops, signifying a flat-band situation.

To conclude here, in the context of polarization fields, ZnCdO/ZnO QW structures with a well width of about 3.5 nm and an adequate Cd content ($y \approx 0.2$) appear most suitable for green-wavelength lasing. At first glance, the carrier density in the range of 10^{13} cm^{-2} necessary for regeneration of a strong electron-hole overlap seems to be very high. However, population inversion itself naturally requires high carrier densities. For ZnO/ZnMgO QW structures for example, where polarization fields do not play a dominant role, this density is found to be in the $4{\cdot}10^{12}$ cm^{-2} range [28]. Moreover, the presence of a polarization field might be also beneficial for long-wavelength application, as it reduces the overall transition energy. In particular, this holds true for emitters based on ternary alloys where the alloy concentration is already critical with respect to material quality and/or phase segregation and a red-shift of the emission can only be achieved by further alloying. In this regard, a prominent example is the InGaN/GaN heterosystem where an extension of the laser emission to green wavelength is challenging, too. Here, the pros and cons of polarization fields have been investigated theoretically and experimentally [2] supporting the results gained in this section.

4.3. Visible-wavelength laser action up to green wavelengths

Based on the findings above, optimized MQW structures have been fabricated. The active area of these structures consists of stacks of seven to ten QWs separated by 10-nm-wide ZnO barriers, which are embedded in ZnMgO claddings in order to improve the optical mode overlap, as illustrated in Figure 4.7. The bottom layer (500 - 600 nm) is about 3 times thicker than the upper cap. Note that the ZnMgO bottom layer of the MQWs might change the strain situation compared to the SQWs with ZnO buffer layers. The samples are excited by the excimer pumped dye laser system described in Section 3.2 at a wavelength of 360 nm. Thus, the laser photon energy is chosen below the absorption edge of the ZnMgO claddings but above the absorption edge of the ZnO barriers. The excitation spot is transformed into a stripe which can be tuned in length and height with an accuracy of about ± 50 μm. The surface emission, which is recorded in a backward geometry, is excited by a small spot of 300×300 μm^2 in order to minimize distortion by stimulated emission. In the lasing measurements, the stripe is extended to $L = 1500$ μm and the emission signal is detected in the direction along the stripe from the edge of the sample. Emission spectra are always averaged over 100 excitation pulses.
Low-temperature data of two blue-emitting samples with a well width of $d_{\mathrm{w}} = 2.1$ nm but different Cadmium content are collected in Figure 4.8. Radiative recombination of localized carriers is signified by the spectrally broad spontaneous emission (see upper panels). The shape and the spectral position of the emission are almost independent of the excitation intensity. No signatures of emission from trions or localized biexcitons have been observed. The sublinear power dependence of the surface PL rules out in general many-particles effects (see inset in Figure 4.8 (b)). In the 10 kW/cm^2 range distinct laser action emerges in the edge configuration (lower panels). As discussed in the previous section, the polarization fields of such QW structures are largely screened at these excitation levels. The presence of a comb of modes (see also Figure 4.9) is con-

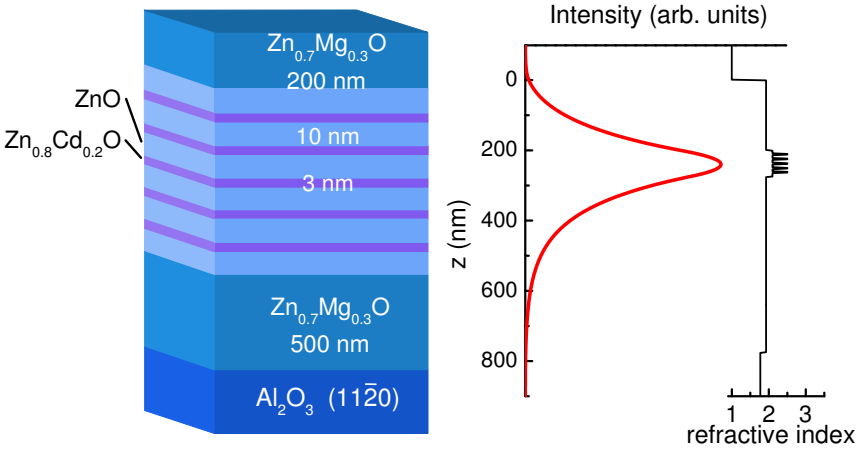

Figure 4.7: Design of ZnCdO/ZnO MQW laser structures. Left: schematics (not true to scale). Right: RI profile as well as intensity distribution of the guided wave ($\lambda = 500$ nm). Index of refraction for ZnO, ZnMgO and ZnCdO is taken from Reference [8], [73] and [74], respectively.

sistent with an inhomogeneously broadened laser transition. The laser band appears on the high-energy side of the spontaneous emission maximum. While the shift between the spontaneous emission peak and the laser transition is only some 10 meV for a relatively small Cd content (Figure 4.8 (a)), it can reach some 100 meV for higher concentrations (Figure 4.8 (b)). In view of the processes presented in Section 2.1, such an emission characteristic cannot be explained.

On the other hand, the excitation level could be already strong enough to create an e-h plasma. In order to estimate the carrier density at threshold more precisely, the QWs are directly pumped. If excited at a wavelength of 370 nm, an absolutely identical emission behavior at a two times higher threshold is observed. The experimentally determined absorbance for a very similar MQW structure (7-period $d_w = 2.6$ nm and $y = 0.1$ MQW) is about 0.2. The carrier lifetime, which is the main uncertainty, is estimated to be about 300 ps [1]. This gives roughly a carrier density of $n = 6 \cdot 10^{12}\text{cm}^{-2}$ at threshold, which is definitely in the range of the theoretical predicted Mott density.

At this point, a final statement about the electronic origin of the optical gain cannot be made. The carrier densities at threshold are most likely high enough to create an degenerated e-h plasma, while the emission characteristic rather excludes this scenario. The interplay of carrier localization and screening of the electric fields makes it very difficult to correctly interpret the time-integrated emission spectra. Maybe the emission pattern under pulsed pumping is altered by a rather complex screening dynamics, which could mean that the spontaneous emission appears in fact at higher photon energies while excitation. In this regard, further contributions might result from a lower carrier density at the borders of the excitation stripe as well as carrier diffusion out of the excitation region. However, these effects alone can hardly produce such large shifts between laser transition and spontaneous emission maximum, observed at higher Cd concentrations.

[1] The plots shown in Figure 4.3 give rise for a lifetime shorter than 500 ps at such high injection levels.

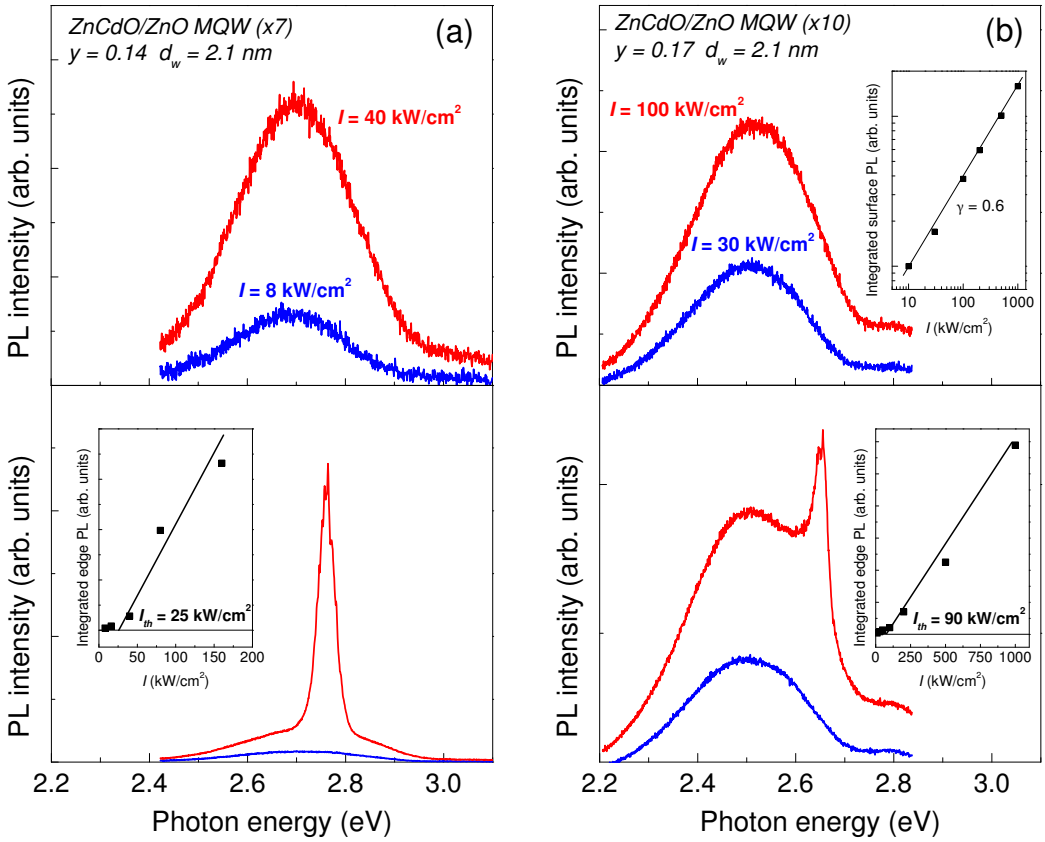

Figure 4.8: Spontaneous emission and lasing from two ZnCdO/ZnO MQW structures. Temperature is 5 K. Upper panel in (a) and (b): Spontaneous emission taken in backward geometry. Inset in (b): Integrated spontaneous emission versus excitation intensity (double logarithmic scale). The slope (γ) of the line is 0.6. Lower panel in (a) and (b): Laser action observed from the sample edges at the same excitation intensity. Inset: Lasing threshold.

It might be possible that the lasing is related to a band to band transition, while the spontaneous emission is still dominated by localized carriers. They start to saturate, which enables the built-up of a sufficiently large population inversion necessary to meet the gain loss condition. Such a scenario could explain the observed emission characteristic.

However, in order to understand the nature of the optical gain in ZnCdO/ZnO MQW structures pump-probe measurements are required, which provide direct access to the gain. Furthermore, the spontaneous emission has to be monitored while excitation, for example by a gated CCD system.

The lasing threshold of the sample of Figure 4.8 (a) is as low as 25 kW/cm^2, which compares reasonable well with lasing thresholds obtained on ZnO/ZnMgO QW structures [28]. Of course, the properties of the resonator have to be taken into account in order to adequately evaluate the lasing threshold. The present samples are unstructured

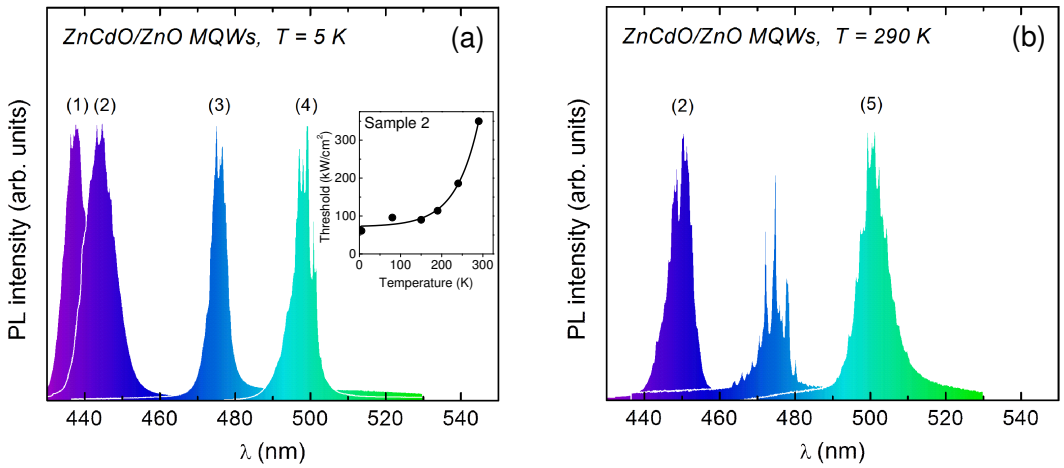

Figure 4.9: Variation of laser emission with structure design of ZnCdO/ZnO MQWs. Edge emission at $T = 5$ K (a) and room temperature (b). The excitation intensity is always 1 MW/cm^2. Inset in (a): Temperature dependence of the threshold of sample (2). Line is to guide the eye.

and the feedback is not related to a Fabry-Perot cavity, as it will be discussed in the next chapter. However, irrespective of the details of the resonator such a low threshold is an indicator of material quality as well as proper sample design.

Figure 4.9 summarizes further characteristics of the laser action. The MQW lasing wavelength can be systematically tuned by the design of the structure (sample parameters are found in Table 4.1). Consistent with the weaker quantum confinement, the wider well lases at lower photon energy at a given Cd concentration (curves 1 and 2 in Figure 4.9 (a)). A higher concentration shifts, at a given well width, the lasing to longer wavelengths (curves 3 and 4) and the sample with the highest Cd concentration starts to lase at about 500 nm. However, while the lasing threshold of violet/blue-emitting samples is some 10 kW/cm^2, it increases with the Cd concentration and reaches 350 kW/cm^2 for the green-emitting sample.

Laser action is present up to room temperature (see Figure 4.9 (b)) with an increase of the lasing threshold by about a factor of 5 (see inset in Figure 4.9 (a)). Despite the higher temperature and threshold intensity, no qualitative change in the appearance of the laser action is observed. The room temperature lasing threshold is comparable to blue-emitting InGaN/GaN MQW structures [75].

Interestingly, sample 4 does not start to lase at room temperature even at an excitation intensity of 1.5 MW/cm^2. However, green-wavelength lasing can be achieved at room temperature when the Cd concentration in the well is decreased by a mole fraction of 0.05 and the well width is extended to 3.3 nm (Sample 5), which indicates proper sample design according to the results of the previous section. The room temperature lasing threshold of 450 kW/cm^2 is only moderately higher compared to blue-emitting samples. The lasing modes on the long-wavelength tail of the broad inhomogeneous envelope band appear at a wavelength of 510 nm, which is indeed fully in the green spectral range.

Sample	y	d_{w}
1	0.10	2.6 nm (x7)
2	0.10	3.2 nm (x7)
3	0.17	2.1 nm (x10)
4	0.24	2.1 nm (x7)
5	0.19	3.3 nm (x10)

Table 4.1: Sample parameters of laser structures shown in Figure 4.9. Number of QWs is given in parenthesis.

4.4. Conclusion and outlook

In conclusion, well-defined ZnCdO/ZnO QW structures in a wide range of structural design have been investigated. They exhibit polarization fields similarly huge as known for the InGaN/GaN heterosystem. Effective screening of these polarization fields by photogenerated carriers occurs already at excitation in the 10 kW/cm^2 range. In the same excitation range, distinct laser action of ZnCdO/ZnO MQWs emerges. In this regard, it has been demonstrated that ZnCdO is indeed a potential candidate for making a semiconductor laser operating in the green-wavelength range. It turned out that, even in the presence of strong polarizations fields, wells with a relatively large width of about 3.5 nm but a reduced Cd concentration are most suitable for long-wavelength applications. The longest lasing wavelength achieved on these appropriately designed MQW atructures is 510 nm. If needed, operation at violet and blue wavelengths is also assured.
The nature of the optical gain has to be identified by further studies in order to optimize laser gain and threshold, as well as to shift the spectral range to even longer wavelengths. Obviously carrier localization plays an essential role here. The nature of this localization (alloy fluctuations, segregation and so on) as well as the length and energy scales are not yet known.

5. Random Semiconductor Lasers: Scattered versus Fabry-Perot Feedback

5.1. Introduction

Laser action relies on the amplification of light combined with optical feedback. A simple realization of this concept is a gain medium embedded between two parallel mirrors. Such a Fabry-Perot cavity is commonly used in today‘s semiconductor devices. Hereby, most of the operational parameters (threshold, mode spectrum, directionality) of the laser are determined by the specific arrangement of the cavity.
Recently, random lasers have attracted much attention. Here, the feedback is not provided by an external resonator, but by scatterers which are randomly distributed in a gain medium or which by themselves act as optical amplifiers. For practical applications, random lasing of semiconductor nanostructures is of particular interest. Demonstrations in this area include nanoparticles in powders [76, 77, 78], nanorods [79, 80], etched porous networks [81, 82], and textured QW structures [83]. In this context, the question arises of how the operational parameters of the random laser compares with those of the standard Fabry-Perot cavity. Imagine that a Fabry-Perot laser cavity is randomly filled with an increasing number of passive scatterer. The scatterers induce extra losses and, as one might simply conclude, the laser threshold increases. On the other hand, random lasing is expected to emerge when number and strength of the scatterer exceed certain levels. The interplay between these two processes is the subject of this chapter.
The nanostructures under study are again ZnCdO/ZnO MQWs. They are capable of low-threshold visible wavelength lasing under optical pumping, as demonstrated in the previous chapter. The details of the optical feedback responsible for laser action have not been discussed so far. In this chapter, it will be shown that these QW structures actually act as random lasers, as a result of growth imperfections. The fabrication of micro-resonators enables to directly study and compare cavity and scattered feedback. The results of this chapter have been published in Reference [84].

5.2. Random Lasing of ZnCdO/ZnO multiple quantum well structures

The ZnCdO/ZnO MQW structures are fabricated by MBE under the conditions described in Section 3.1. The overall design is identical with the MQW structures presented in the previous chapter (see Figure 4.8). A relatively low cadmium content in the wells is chosen for low-threshold lasing in the violet/blue spectral range. The source for optical excitation of the samples is again the excimer pumped dye laser with a pulse duration of 20 ns. The pump wavelength is 360 nm and the sample temperature is 5 K (only for the spectra shown in Figure 5.1 (b) the temperature is 290 K). The excitation is along a stripe of constant width $w = 300$ μm and variable length $L = 0.3$-3 mm. The edges of the sample are very rough, as they are in the as-grown state, so that any reflection of light is quite diffusive. To further suppress possible feedback, the excitation region is positioned at sufficient distance from the sample edge. The high resolution setup (spectral resolution of 0.03 nm) described in section 3.2.2 is used to record the emission spectra (except the spectra shown in Figure 5.1 (a) and (b)).
Typical data on the laser action of the ZnCdO/ZnO MQW structures are summarized in Figure 5.1. The transition from spectrally broad spontaneous emission to narrow laser action at sufficient optical excitation is shown in Figure 5.1 (a). There is a well defined lasing threshold decreasing down to some 10 kW/cm^2 for the longest L (see inset). Lasing is achieved independent of the position or the orientation of the excitation stripe on the sample. In Figure 5.1 (b) selected lasing spectra, obtained by rotation of the sample around its axis (see inset) are shown. There is also no correlation between the mode spacing and the length of the sample or the excitation stripe. Excitation with a radially symmetric spot yields qualitatively identical mode spectra at a slightly increased threshold (see Figure 5.1 (c)). The number and relative intensity of the modes are very sensitive to the excitation level. This is exemplified in Figure 5.1 (d). Far above threshold, single mode features become less distinctive and an envelope-type spectrum develops (upper panel). For the same reason, averages taken over 100 excitation pulses produce apparently smoother mode spectra as a result of power fluctuations (center and lower panel).
All these findings exclude that the laser action is related to feedback from a Fabry-Perot-type cavity and rather hint at a type of random lasing. Verification is found when inspecting the light emerging from the top surface of the sample, i.e., perpendicular to the propagation of the laser emission, with a microscope. Figure 5.2 (a) reveals the existence of discrete scattering centers on a macroscopic length scale with densities of some 100 per mm^2. Examination by scanning electron microscopy (SEM) shows that these scatterers are related to holes in the surface of the nanostructure with typical diameters between 0.5 and 1 μm. An atomic force microscopy (AFM) image of such a hole is shown in the upper panel of Figure 5.2 (b) together with the height profile taken from the image (lower panel). The depth of the holes is found to be approximately 300 nm, which means that they pass the upper cap as well as the active zone MQW part (see Figure 4.7). Most probably they originate from locally impaired nucleation at the

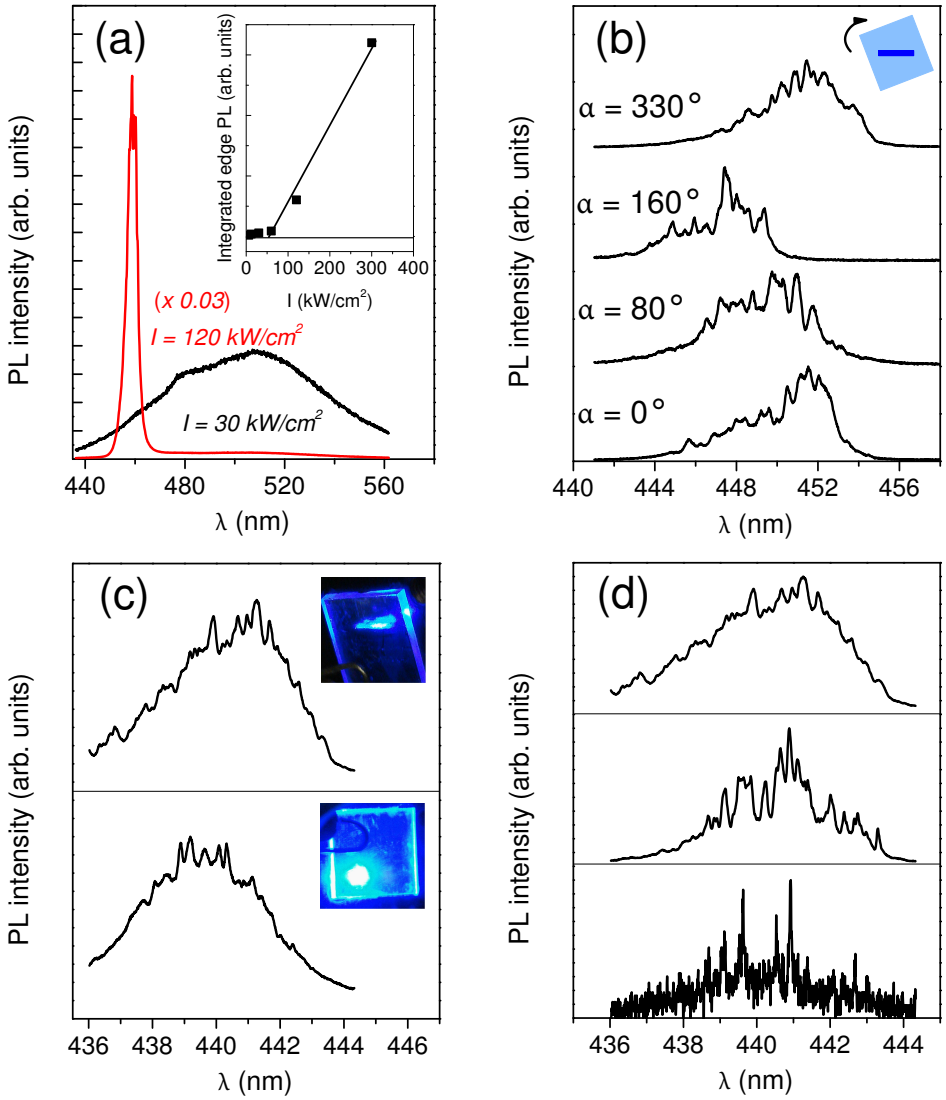

Figure 5.1: Laser action of ZnCdO/ZnO QW structures. (a) Spectral shape of the edge emission at low and high excitation intensity I (7 wells of width $d_w = 3.1$ nm and Cd concentration $y = 0.16$). Inset: Spectrally integrated emission yield versus I. (b) Spectra obtained under rotation of the sample around its axis ($d_w = 2.1$ nm, $y = 0.14$) as shown in the inset at $T = 290$ K and $I = 500$ kW/cm^2. (c) Emission excited by a stripe or a spot. Upper panel: Average spectrum over 100 excitation shots at $I = 300$ kW/cm^2 excited with a stripe of $L = 3$ mm. Lower panel: Average spectrum over 100 excitation shots at $I = 300$ kW/cm^2 excited with a radially symmetric spot of diameter 1 mm. Insets: Photographs at laser action. (d) Spectrum of lasing modes ($L = 3$ mm). Upper panel: Average spectrum over 100 excitation shots at $I = 300$ kW/cm^2. Center panel: The same at $I = 120$ kW/cm^2. Lower panel: Spectrum under single-shot excitation at $I = 120$ kW/cm^2. Sample parameters in (c) and (d): $d_w = 3.2$ nm, $y = 0.10$.

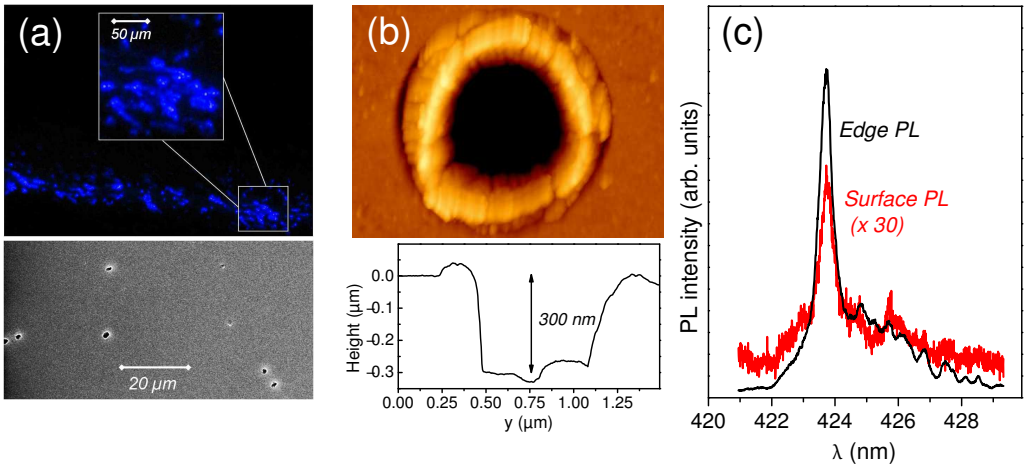

Figure 5.2: Optical feedback by growth imperfections. (a) Upper panel: Scattered light detected under laser action from the sample surface, i.e., perpendicular to the propagation of the laser emission. Lower panel: SEM image of the sample surface. (b) Upper panel: AFM image of a hole. Lower panel: Height profile taken from the AFM image. (c) Averaged lasing spectra collected from the sample edge (black) and from the surface (red) ($L = 3$ mm, $d_w = 2.2$ nm, $y = 0.06$).

sapphire surface when starting the low-temperature growth of the QW structure. The emission above threshold collected from the edge and surface of a sample is depicted in Figure 5.2 (c). Both spectra are almost identical albeit a much weaker intensity of the surface emission. Thus, the light shown in Figure 5.2 (a) is indeed out of plane scattered laser light. From these findings, it can be concluded that irregularities of such type do not simply worsen the optical properties as one might naively expect, but can give rise for random lasing.
The semiconductor random laser of this study is essentially different from those frequently found in literature, as the active material is a well-defined QW structure. Here, propagation of light takes place in two dimensions. In contrast to nanoparticles in powders or nanorods, the feedback for lasing is provided by passive scatterers. Moreover, the average distance between two scatterers is much larger than the wavelengths of light.

5.3. Scattered versus Fabry-Perot Feedback

In order to compare random versus Fabry-Perot lasing, micro-resonators have been fabricated. Grooves with a depth of about 300 μm and a spacing of 300 μm, 500 μm, and 900 μm are defined in the reverse side of a 500-μm-thick sapphire substrate by ultraviolet laser light. Subsequently, the ZnCdO/ZnO MQW structure ($d_w = 3.1$ nm, $y = 0.16$) is grown on the front side and micro-resonators are produced by cracking the sample along the grooves into stripes. Scanning electron microscopy with a resolution better than 0.2 μm revealed flat facets in the active region. Their natural facet reflectivity

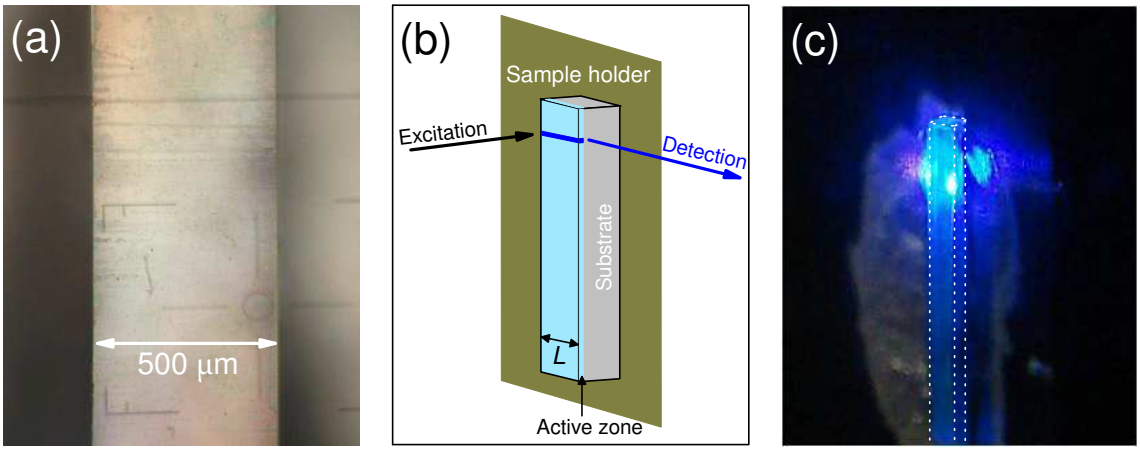

Figure 5.3: ZnCdO/ZnO MQW micro-resonators. (a) Microscope image of a $L = 500$ μm micro-resonator (top-view). (b) Schematics of the experiment. (c) Photograph of laser action ($L = 500$ μm). The white-dotted line indicates the edges of the micro-resonator.

is about $R = 0.1$. In Figure 5.3 (a), a microscope image of a $L = 500$ μm resonator stripe is shown. In the experiment, the resonators are homogeneously excited across their width, and the signal is detected from the facet of the resonator, as illustrated in Figure 5.3 (b). A photograph of the 500 μm resonator stripe at laser action is shown in Figure 5.3 (c). Figure 5.4 (a) depicts the lasing threshold of the micro-resonators as a function of their inverse length along with the same dependence for stripe excitation of an unstructured part taken from the same wafer. In both cases, the relation is in good approximation linear; however, the thresholds of the micro-resonators are about 2-3 times lower. The feedback from the facets is also manifested in the far-field emission pattern where the beam divergence decreases by about a factor of 5 (Figure 5.4 (b)). The fact that the threshold depends on the size of the excitation region excludes that localized modes are predominantly involved in the laser action. This is consistent with the large free-path to wavelength ratio in these samples. Such localized modes have been observed in nanocrystalline ZnO powder, and it was shown that they can co-exist with extended modes [78].

Further information is contained in the mode spectra of resonator structures, which are presented in Figure 5.5. The Fabry-Perot mode spacing of the $L = 300$ μm and $L = 500$ μm is estimated to be approximately $\Delta\lambda = 0.14$ nm and 0.08 nm, respectively. Instead, the averaged emission spectra expose features with roughly one order of magnitude larger separation and a spectral width of about 1-2 nm (Figure 5.5 (a, c)). Strikingly, these super modes resolve indeed in sharp peaks with exactly the estimated Fabry-Perot spacing in the single-shot excitation regime (Figure 5.5 (b, d))). However, compared to a standard Fabry-Perot laser without scatterers, where all modes should exhibit a similar threshold gain, the random feedback of the scatterers obviously creates a subtle modal gain distribution.

While the overall appearance of the super modes is very similar for all cavity lengths

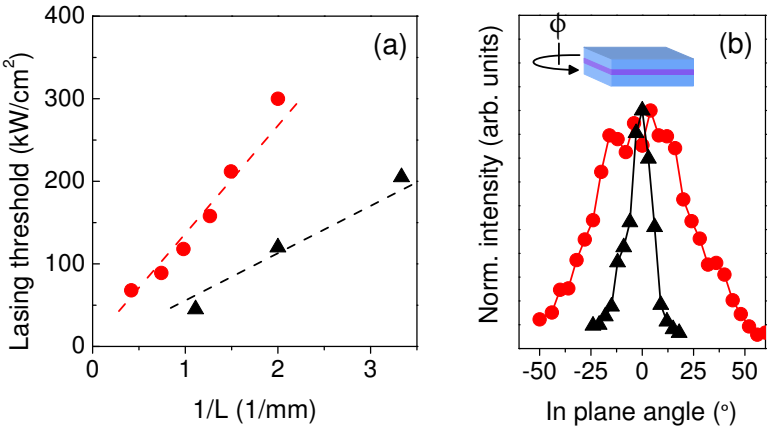

Figure 5.4: Laser action of micro-resonators (triangles) and unstructured samples (dots). (a) Lasing threshold versus inverse length of the resonator (width of cracked stripe) and of the excitation stripe, respectively. (b) Far-field pattern of the laser emission taken in the plane of the QWs as shown in the inset.

studied, their number and relative intensity are again strongly power dependent. This is exemplarily displayed for the $L = 500$ μm resonator structure in Figure 5.5 (c). Once more an envelope-type spectrum develops far above threshold. The weakly structured average spectrum of the lowest threshold $L = 900$ μm resonator far above threshold is displayed in Figure 5.5 (e). However, the Fourier decomposition even of such smooth average spectra uncovers clearly a periodicity (Figure 5.5 (f)). The gained mode spacing $\Delta\lambda$ matches the resonator length as shown in Figure 5.5 (g), providing a reasonable effective index of refraction ($n - \lambda\frac{\partial n}{\partial \lambda}$) of about 2.35 (see Equation 2.13). These findings indicate a subtle mode organization resulting from the interplay between cavity and random feedback.

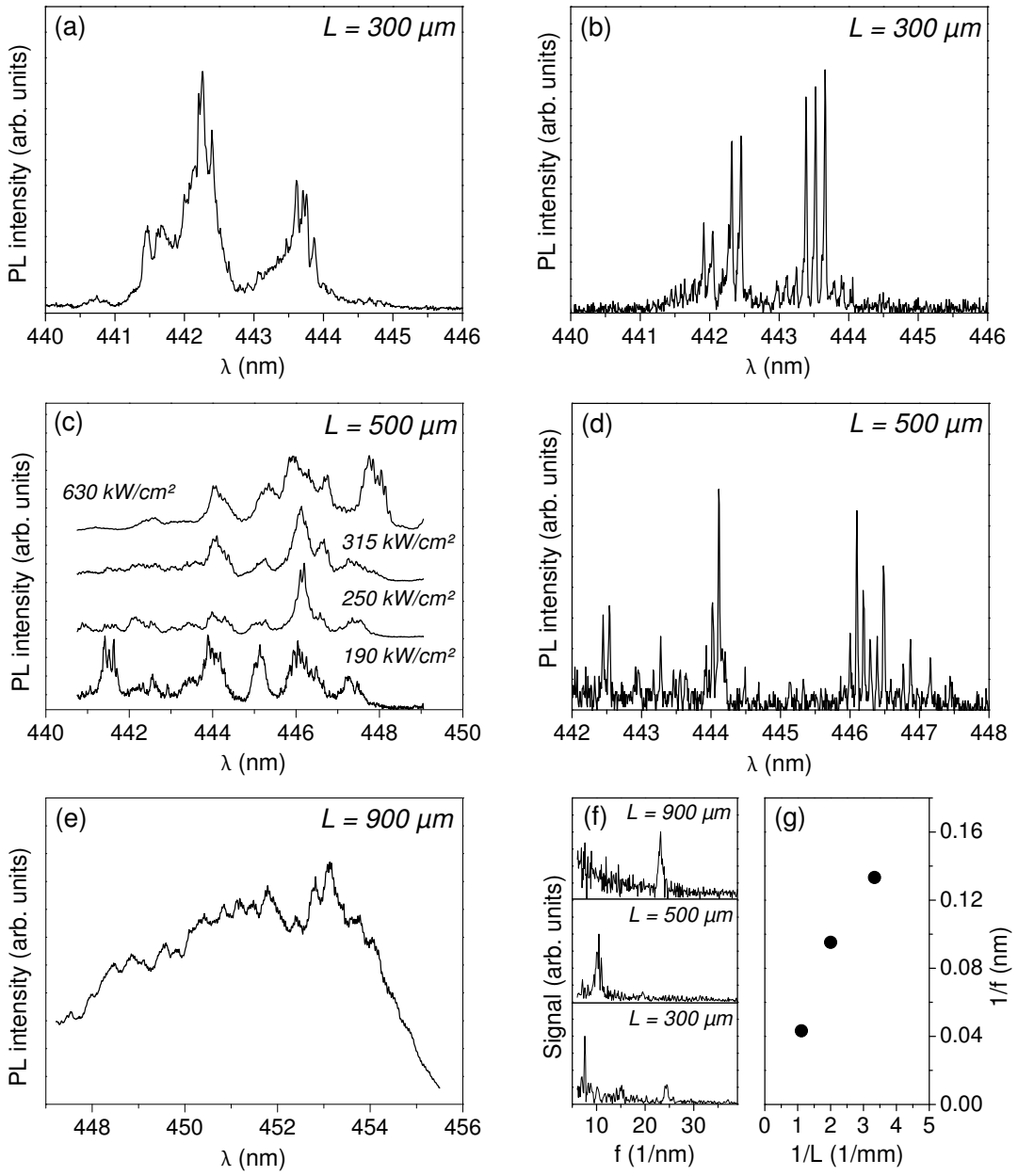

Figure 5.5: Mode organization in micro-resonator structures ($d_w = 3.1$ nm, $y = 0.16$). (a) Average mode spectrum of a $L = 300$ μm resonator at $I = 250$ kW/cm^2. (b) The same taken for 5 excitation shots. (c) Intensity dependent averaged emission spectra of a $L = 500$ μm resonator. (d) Single shot emission spectrum of a $L = 500$ μm resonator ($I = 250$ kW/cm^2). (e) Average mode spectrum of a $L = 900$ μm resonator ($I = 620$ kW/cm^2). (f) Fourier decomposition of envelope-type average spectra well above threshold for different resonator lengths. (g) Mode separation $\Delta\lambda$ deduced from (f) versus inverse resonator length.

5.4. Theoretical analysis

Many aspects of light propagation in random media can be adequately treated in terms of point scatters (see, for example, Reference [85]). For weak scatterers embedded in a host of extension L and gain coefficient g, that pair with the largest separation dominates the laser action and the threshold gain in a two-dimensional setting is easily derived [37],

$$g_{\mathrm{th}}^{\mathrm{RL}} L = \ln\left(2\pi L/\sigma\right) \tag{5.1}$$

where σ denotes the isotropic Rayleigh cross section (with dimension of a length). When compared with the threshold of the standard Fabry-Perot laser $g_{\mathrm{th}}^{\mathrm{FP}} L = \ln(1/R)$, it follows that $g_{\mathrm{th}}^{\mathrm{FP}} \ll g_{\mathrm{th}}^{\mathrm{RL}}$ for typical semiconductor-air reflection coefficients, as per definition $\sigma \ll \lambda \ll L$. In contrast, the threshold increase for the random laser shown in Figure 5.4 is only quite modest, indicating scattering markedly stronger than accountable in the Rayleigh limit. The theoretical analysis has thus to be extended to Mie scattering taking into account the finite size of the entities. So far, only the case up to six Mie scatterers located in a small μm-sized gain region has been addressed by finite-difference time-domain calculations [37]. Within our group a different approach has been developed. This approach is based on a direct calculation of the complex mode spectrum by solving the nonlinear eigenvalue problem for the scatterer amplitudes allowing for a systematic treatment of much larger configurations. In the following, the traits of this method will be presented and the numerical results will be discussed in context with the experiment. Further details can be found in Reference [84] and its supplemental part.

In analogy to the experiment, a two-dimensional material of index of refraction n between two parallel plane mirrors with reflectivity R and separation L is considered. A constant gain coefficient $g > 0$ is provided in an orthogonal stripe of width w. Within the gain stripe, N identical circular dielectric scatterers with radius a numbered by s are randomly distributed. The field acting on a particular scatterer s at planar position $\vec{r_s} = (x_s, y_s)$ is the superposition of partial fields outgoing from all other scatterers at position $\vec{r_{\bar{s}}}$ and from the mirrors at $x_m = mL/2$ with $m = \pm$. The distances r_{sq} between the scatterers ($q = \bar{s}$) as well as between the scatterers and the mirrors ($q = m$) obey $r_{sq} \gg \lambda, a$. Hence, the partial fields incidence from q on s can be approximated by transverse plane waves with scalar amplitudes E_{sq} and propagation unit vectors $\vec{n}_{sq}$. This yields a system of $N(N+1)$ linear homogeneous equations:

$$E_{sq} = \sum_{\bar{s},\bar{q}}^{\bar{q}\neq\bar{s}} S_{sq,\bar{s}\bar{q}} E_{\bar{s}\bar{q}} \tag{5.2}$$

$$S_{sq,\bar{s}\bar{q}} = \begin{cases} G(k, r_{sq}) A(\vec{n}_{sq}\vec{n}_{\bar{s}\bar{q}})\delta_{q\bar{s}} & (q \in \text{scatterers}) \\ Q_{sq,\bar{s}\bar{q}} & (q \in \text{mirrors}) \end{cases}.$$

The upper line stands for direct coupling between $\bar{s}$ and s, while reflection on a mirror before the field from $\bar{s}$ arrives at s is accounted for in the lower line. $A(\vec{n}_{\mathrm{out}}\vec{n}_{\mathrm{in}})$ represents the angle-dependent plane-wave scattering amplitude taken for a cylinder with both

polarization as well as propagation direction of incoming and outgoing field perpendicular to its axis [86]. The far-field Green function $G(k,r) = \exp(ikr + i\pi/4)/\sqrt{8\pi kr}$ of the two-dimensional Helmholtz equation describes the propagation of the outgoing wave in the gain region with wavenumber $k = k_0 - ig/2$. Inclusion of the mirror feedback is not straightforward as the scatterers couple on and off cavity axis propagating light yielding unlimited amplification. To overcome this problem the waveguide character of a gain region with finite transverse width w is used. Expanding scattered waves in series of the waveguide modes ν solving $[\nabla_y^2 + k^2(y)]\phi_\nu(y) = \beta_\nu\phi_\nu(y)$ under radiative boundary conditions yields:

$$Q_{sm,\bar{s}\bar{q}} = \frac{\sqrt{R}}{2ik}\sum_\nu \phi_\nu(y_s)\phi_\nu(y_{\bar{s}})e^{i\beta_\nu r_{sm}} \tag{5.3}$$
$$\times \frac{A(\vec{n}_{m\bar{s}}\vec{n}_{\bar{s}\bar{q}})e^{i\beta_\nu r_{m\bar{s}}} - A(\vec{n}_{-m\bar{s}}\vec{n}_{\bar{s}\bar{q}})\sqrt{R}e^{i\beta_\nu(L+r_{-m\bar{s}})}}{1 - Re^{2i\beta_\nu L}}.$$

Already accounting for the fundamental mode has provided sufficient precision in the calculation presented below. Solving $\det[\delta_{s\bar{s}}\delta_{q\bar{q}} - S_{sq,\bar{s},\bar{q}}(k)] = 0$ for complex wave number k provides the spectral position of the lasing modes (real part) as well as their threshold gain (imaginary part).

In the numerical analysis, the positions of the scatterers are set by a random number generator. Unrealistic configuration, where, e.g., the separation between two scatterers is smaller than the wavelength are disregarded. Searching for some 10 modes of lowest threshold gain within a few nanometer wide spectral interval around a center wavelength $\lambda = 500$ nm is sufficient to obtain representative results. While detailed position and threshold gain depend on the specific configuration under study, there are a number of general features that are commonly found in all configurations. Figure 5.6 summarizes such features calculated for the parameters of a ZnCdO/ZnO QW structure. Black solid curves in Figure 5.6 (a) represents the threshold gain as a function of the scatterer radius a. In the Rayleigh limit $a \ll \lambda$, as already argued above, the threshold of the pure random laser with no mirrors is much larger than that of the untainted Fabry-Perot laser (dash-dotted line). Consistently, the threshold of the Fabry-Perot laser with scatterer is here practically identical with $\ln(1/R)$. An initially distinct lowering of the RL threshold for increasing radius devolves into a plateaulike behavior when $a \gtrsim \lambda/n$. For the Fabry-Perot laser with scatterer, there is merely a slight increase of the threshold. Both curves are superimposed by modulations caused by interference effects, which becomes clear in what follows.

Interestingly, though a becomes significantly larger than λ/n, the scattering is still weak in the sense that couplings involving more than pairs of scatterers can be neglected. In this case, approximation formulas for the threshold gain can be analytically derived. Indeed, these approximations (circles) reproduce very well the full numerical curves. The weak-scattering RL threshold reads as formula 5.1, but with the isotropic σ replaced by the Mie backscattering cross section $\sigma_b = |A_\pi|/4k_0$ [37]. The modulations of the threshold are due to resonances of this cross section. Maxima occur when waves reflected at the front and back side of the scatterer interfere destructively, i.e., approximately at

radii being integer multiples of $\lambda/2$. The approximation for the Fabry-Perot laser with scatterer is:

$$g_{\mathrm{th}}^{\mathrm{FPS}} L = \ln(1/R) + N\sigma_{\mathrm{ext}}/w \tag{5.4}$$

where $\sigma_{\mathrm{ext}} = \mathrm{Im}A_0/k_0$ is the Mie extinction cross section. The correction to the pure Fabry-Perot term is due to forward scattering of the wave circulating in the cavity. The extinction cross section of a large object is twice its geometrical cross section so that $g_{\mathrm{th}}^{\mathrm{FPS}}$ is an increasing function of a. The weak modulations are due to interference between waves crossing and bypassing the scatterer.
The difference in the thresholds of random laser and Fabry-Perot laser with scatterers agrees reasonable well with the experimental data in the relevant scatterer size range. Fluctuations of the scatterer size average out the modulations predicted theoretically. The right-hand side of formula 5.1 is only a smooth function of the stripe length, explaining why the threshold of both random laser and Fabry-Perot laser with scatterers follow closely a $1/L$ dependence in the experiment.
The modal threshold gain versus spectral mode position is depicted in Figure 5.6 (b). As $g = \mathrm{const.}$, all modes are exhibiting the same threshold in the pure Fabry-Perot laser, and variations are thus a consequence of random feedback. Unlike steady state, a large number of modes contribute to the time-integrated emission under pulsed excitation. However, those with the lowest threshold are dominant and form the super modes in the experiment. While the random laser threshold gain can be well estimated by two scatterers at distance L, the presence of other scatterers results in a significant fluctuation of the spectral mode spacing (Figure 5.6 (c)). In contrast, the modes of the Fabry-Perot laser with scatteres are practically pinned to the positions of the pure Fabry-Perot cavity, fully consistent with the measurement (Figures 5.5 (g) and 5.6 (d)).

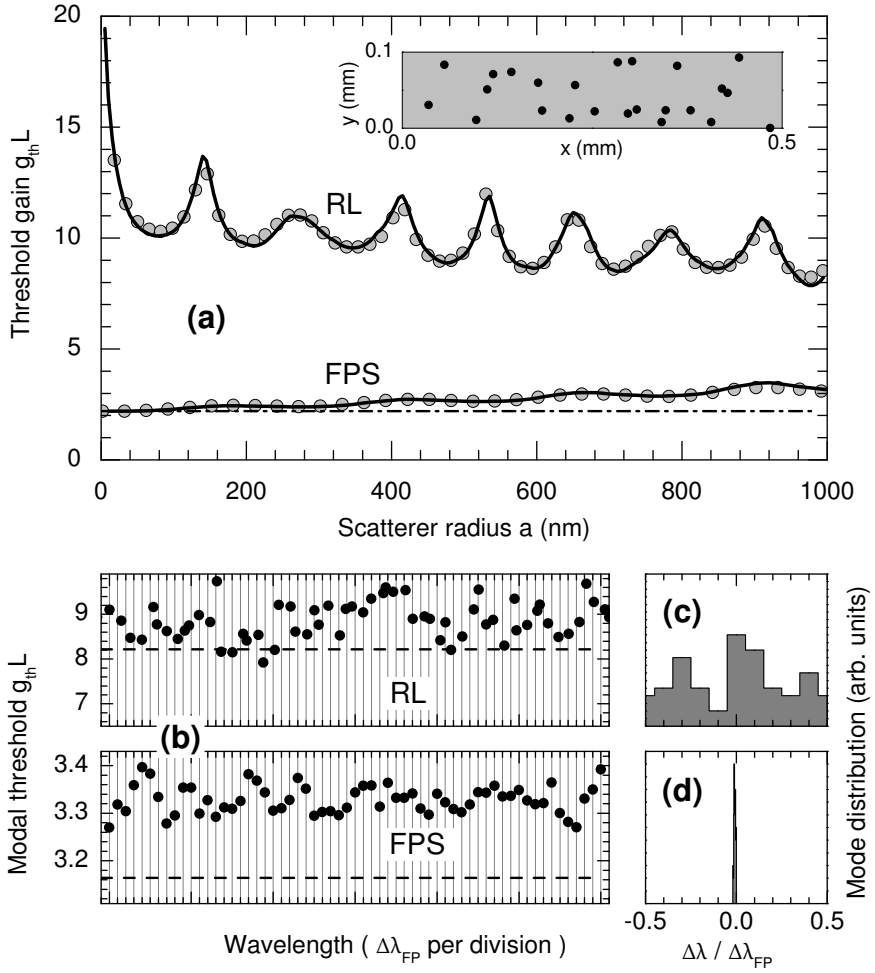

Figure 5.6: Laser action of randomly distributed Mie scatterers for a semiconductor-hole system. RL: Scatterers only ($R = 0$), FPS: Scatterers with Fabry-Perot cavity. (a) Threshold gain $g_{\rm th}L$ versus scatterer radius a. Inset: Position of the scatterers within the gain stripe. Black solid: Full solution of eqs. (5.2) and (5.3). Circles: weak-scattering approximations (see text). Dash-dotted line: $\ln(1/R)$. (b) Modal thresholds versus spectral position ($a = 480$ nm). Note enlarged vertical scale. Dashed horizontal lines: $g_{\rm th}L$ from (5.1) with σ_b and (5.4), respectively. Vertical lines: mode positions $\lambda_{\rm FP}$ of the pure Fabry-Perot laser. Right panels (c) and (d): Corresponding distribution of deviations from $\lambda_{\rm FP}$. Parameters: $N = 24, c = v_{\rm g} = c_0/n, n = 2, L = 500$ μm, $w = 100$ μm, mirror reflectivity $R = 0.11$.

5.5. Conclusion and outlook

In this chapter, various aspects of random feedback in semiconductor nanostructures have been revealed:

1. Pure random lasing typically requires a larger gain than under standard Fabry-Perot feedback, even if only the relatively small natural facet reflectivity is utilized. Obviously, ZnO-based nanostructures are predestined in this regard because of their large optical gain.

2. The presence of scatterers does not substantially deteriorate the overall lasing threshold of a Fabry-Perot cavity, as long as $N\sigma_{\mathrm{ext}}/w < \ln R$.

3. The random feedback creates a subtle modal gain distribution that might be of particular importance for the dynamical properties with and without cavity.

So far, the random feedback is created by growth imperfections making it probably impossible to control the spatial distribution as well as the size of the scatterers. Very recently, it was found that focused ion beam (FIB) milling is a well-suited tool for fabrication of artificial holes with almost no size dispersion in ZnO-based heterostructures. As an example artificial holes milled in a ZnO-based test structure are shown in Figure 5.7. In (a) the scatterers are arranged in a circle while in (b) the position of each hole randomly deviates from that in (a) in a radius of 0 to 5 μm. The fabricated holes are almost perfectly cylindrical as shown by the magnified SEM image in Figure 5.7 (c). Interesting configurations might be pairs of scatterers, isolated or interacting groups of scatterers, or semiconductor-hole systems with different degree of disorder (for example, the arrays shown in Figure 5.7 (a) and (b)).

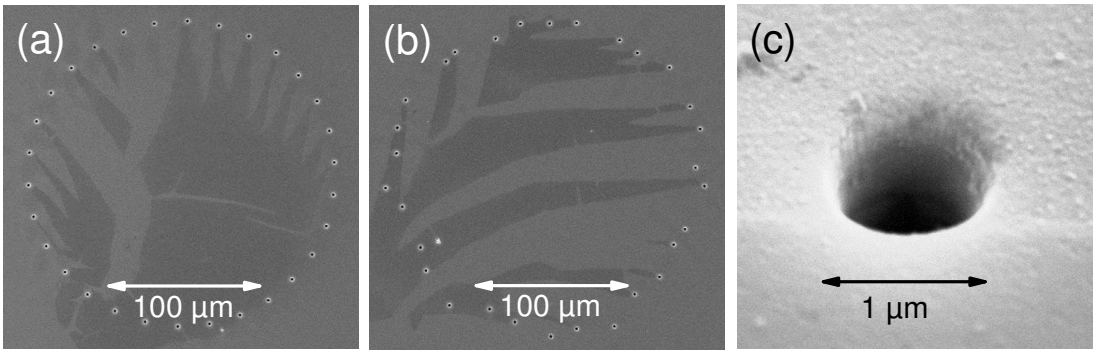

Figure 5.7: SEM images of artificial holes produced by FIB milling in a ZnO-based sample. (a) Circularly ordered holes. (b) Same as in (a) but the position of the holes deviates randomly (see text). (c) bird's eye view of a single hole

6. ZnO-based distributed Bragg reflectors

6.1. Introduction

Metal-based mirrors are part of our daily life and component of many optical elements. For some applications, however, their optical properties are not sufficient. The handling of light beams with large intensities, for instance, is difficult as the metal starts to heat up through absorption of energy. Furthermore, the reflectance of such mirrors typically does not exceed $R = 0.99$ in the infrared spectral range (silvered mirror) and is even less in the visible wavelength range. But low-threshold VCSEL devices, which have an amplification length of only some tens of nanometers, require mirrors with a reflectivity larger than $R = 0.99$.
Such a high reflectivity can be provided by DBR mirrors. In the case of a large RI contrast between the two different DBR layers, the stop band is spectrally very broad and a small number of mirror pairs can create a very high reflectivity. In this regard dielectric DBRs like SiO_2/HfO_2 [87], ZrO_2/MgO [88] or Ta_2O_5/SiO_2 [89] are reported in literature. However, dielectric DBRs are polycrystalline or amorphous and surface roughening with increasing mirror pair number can lead to a lowering of reflectivity. The growth of a semiconductor based active layer on top of a dielectric DBR requires a new processing step and the crystalline quality of this layer is deteriorated.
Another possibility is the realization of DBRs based on layers of a semiconductor and its alloy. Here the RI-contrast is typically smaller resulting in a spectrally narrower stop band and a larger number of mirror pairs for highly reflective DBR structures. However, in general, these materials can be grown single crystalline with monolayer precision forming an atomically flat surface even after growth of several hundreds of nanometers. The *in situ* growth of an active zone and the possibility to finally fabricate monolithically MCs is a major advantage.
In this regard, near- and mid-infrared operating DBRs are technologically well established. For example, layer pairs of (Al,Ga)As are a key component of VCSELs used for fiber-optical interconnections and communication [90]. More recently, GaN-based alloys enabled the fabrication of laser diodes covering a spectrum from UV to green wavelengths [91, 92]. Hence, DBRs based on (Al,In,Ga)N [93] went into focus which are the basis for manufacturing of VCSELs or resonant cavity LEDs in this spectral range.
In what follows it is demonstrated that highly reflective DBRs suitable for application in the UV and blue/green spectral range can be also fabricated out of ZnO- and ZnMgO-layers. Although the growth regime for the ternary ZnMgO has been already established [13], realization of such a DBR is not straightforward as the RI dispersions of the ternary materials are not precisely known. Starting from available material parameters, the objective is to design different DBRs for the entire relevant spectral range,

to measure their optical transmission spectra and finally to theoretically reproduce all spectra with the same set of material parameters. Further, the structural properties of these DBRs have to be evaluated.
The results of this chapter have been published in Reference [94].

6.2. Growth and structural properties

Two types of ZnO-based DRBs have been realized: ZnO/$Zn_{0.65}Mg_{0.35}O$ (type 1) and $Zn_{0.92}Mg_{0.08}O$/$Zn_{0.65}Mg_{0.35}O$ (type 2) for blue/green-emitting ZnCdO and UV-emitting ZnO active layers, respectively. The samples are fabricated in the MBE system described in section 3.1 on the *a*-plane of sapphire. The layers are grown without interruption at T_g = 340 °C with an oxygen limited growth rate of 330 nm/h, which was previously determined from the specular beam intensity oscillations in RHEED. Individual layer thicknesses are defined via growth time.
The growth rate depends on the position of the sample on the Mo holder due to the geometrical arrangement of the effusion cells in the growth chamber. Therefore, a thickness gradient of the layers across the sample occurs. The variation of the layer thickness is found to be approximately 3 % across a 8 x 8 mm^2 wafer. In order to fabricate DBRs (and also MCs) reproducible, the substrates are always fixed at the same position on the Mo holder.

DBR type 1

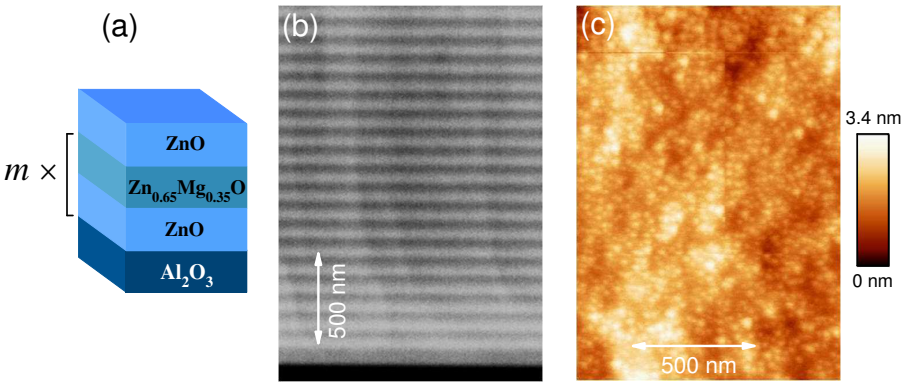

Figure 6.1: Structural properties of ZnO-based DBRs type 1. (a) Schematic layout (not true to scale). (b) Cross section SEM image (m = 27). (c) Surface AFM image (m = 24).

The schematic layout of DBRs type 1 is illustrated in Figure 6.1 (a). The samples consist of m pairs of $\lambda/4$-layers of ZnO/$Zn_{0.65}Mg_{0.35}O$ capped by an additional $\lambda/4$-thick ZnO layer. A Mg content of x = 0.35 slightly below the solubility limit was chosen for the low RI layer in order to reach a large RI contrast while still allowing for stable two-dimensional growth. The cross section SEM (backscattered electrons) image of the bottom part of a type 1 DBR shows periodic layers with abrupt interfaces (Figure 6.1 (b)). Note that the vertical streaks visible in Figure 6.1 (b) are related to the topology of the breaking edge. The surface morphology is investigated by AFM. Even after growth of 2.85 μm (m = 24), a smooth surface is obtained. As can be seen in Figure 6.1 (c) the surface is flat within a few nanometers and the root mean square roughness over a scan area of 2 x 2 μm^2 is 0.5 nm.

DBR type 2

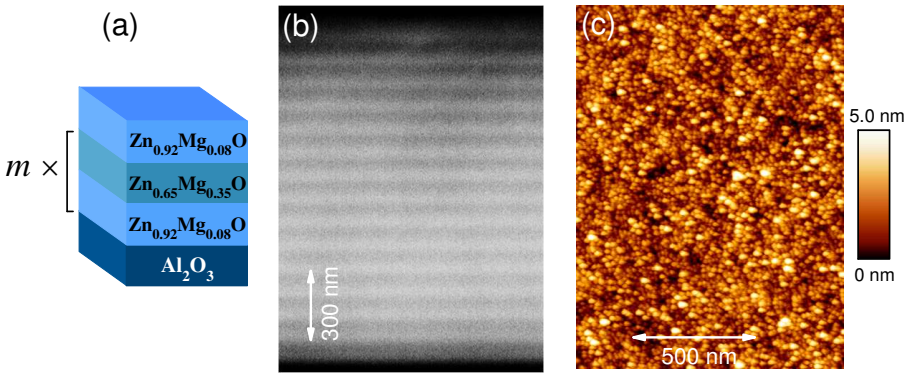

Figure 6.2: Structural properties of ZnO-based DBRs type 2. (a) Schematic layout (not true to scale). (b) Cross section SEM image ($m = 15$). (c) Surface AFM image ($m = 18$).

For type 2 DBRs, the high RI ZnO layers are replaced by $Zn_{0.92}Mg_{0.08}O$ layers as shown in the schematic layout in Figure 6.2 (a). In order to achieve a stable and continuous growth, the Mg-flux for these layers is provided by a second Mg-effusion cell. Again, periodic layers with abrupt interfaces are found in the cross section SEM (backscattered electrons) image shown in Figure 6.2 (b) and a smooth surface morphology is obtained as shown in Figure 6.2 (c). The root mean square roughness over a scan area of 2 x 2 μm^2 is 0.8 nm.

6.3. Optical properties

In this section, normal incidence optical transmission spectra of ZnO-based DBRs type 1 and 2, recorded at room temperature, are presented. Transmission instead of reflection is chosen for experimental convenience, since it allows the determination of $R = 1 - \mathcal{T}$ with high accuracy in a simple way. However, this only holds true if absorption is negligible in the investigated spectral range. Whenever absorption is expected to play a role, complementary reflectivity measurements are performed. The spectra are acquired at the center of the sample with a spot of about 200 μm in diameter.

DBR type 1

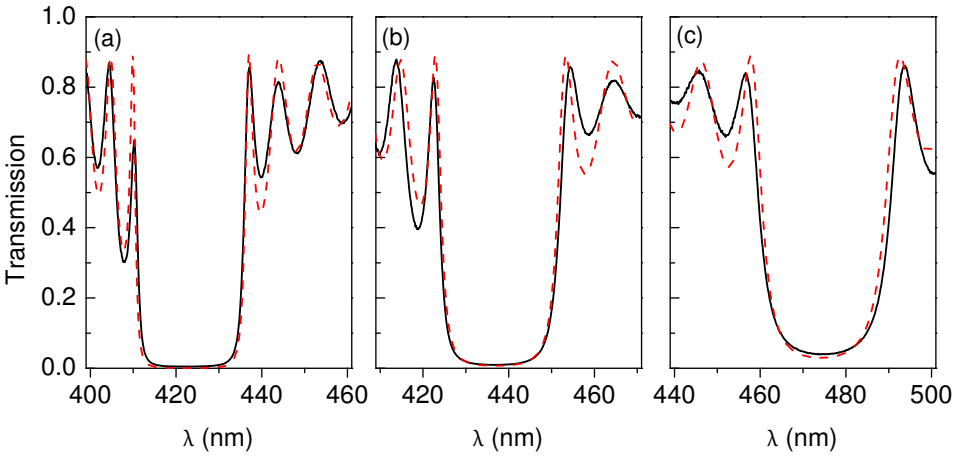

Figure 6.3: Optical properties of DBRs type 1. Transmission spectra (solid lines) and calculated transmission (dashed lines) of DBRs type 1 with (a) $m = 35$ and $\lambda_{SC} = 422$ nm, (b) $m = 27$ and λ_{SC}= 436 nm, and (c) $m = 24$ and $\lambda_{SC} = 475$ nm.

Figure 6.3 collects transmission spectra of type 1 DBRs with different layer thicknesses and mirror pair number. In (a) the transmission of a $m = 35$ DBR designed for violet wavelengths (stop band is centered at $\lambda_{SC} = 422$ nm) is shown. The spectral width of the stop band is about 180 meV and the number of mirror pairs is sufficient to reduce the transmission through the stack at λ_{SC} to $\mathcal{T} = 5{\cdot}10^{-3}$. The stop band center wavelength λ_{SC} is systematically tunable by thickness variation of the $\lambda/4$-layers. For wider layers λ_{SC} shifts into the blue and aquamarine spectral range as demonstrated in Figure 6.3 (b) and (c), respectively. While extension to longer wavelengths is straightforward, operation in the near UV-spectral range is hampered by the onset of absorption of the ZnO layers at approximately 385 nm at room temperature. Neglecting absorption, the transmission spectra can be well reproduced by the transfer matrix model (see red-dashed lines) with the RI parameters for ZnO and $Zn_{0.65}Mg_{0.35}O$ presented in the next section.

DBR type 2

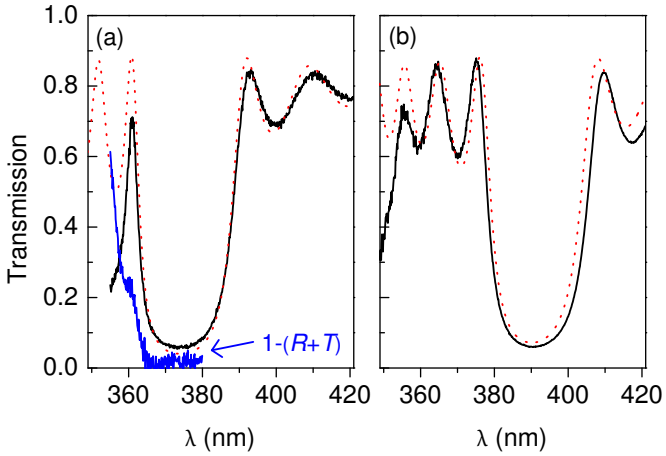

Figure 6.4: Optical properties of DBRs type 2. Transmission spectra (solid lines) and calculated transmission (dotted lines) of DBRs type 2 with (a) $m = 15$ and $\lambda_{SC} = 375$ nm, (b) $m = 17$ and $\lambda_{SC} = 390$ nm. In (a), absorption A = 1-(R+$\mathcal{T}$) is added (see arrow).

As mentioned before, absorption in the ZnO layers of DBRs type 1 excludes their application in the near UV spectral range. Therefore, in type 2 DBRs aimed for ZnO devices, the high RI material has to contain a few percent of Mg to avoid absorption in the mirrors. It turned out that 8% of Mg is a good choice to keep $\Delta n/n$ as large a possible. Figure 6.4 summarizes transmission spectra of type 2 DBRs. The transmission of a $m = 15$ pair sample is reduced to $\mathcal{T} = 0.055$ at $\lambda_{SC} = 375$ nm as shown in Figure 6.4 (a). To ensure that absorption is negligible in the relevant spectral range, a complementary reflectivity spectrum is recorded. The absorption A = 1-(R+$\mathcal{T}$) of the DBR is drawn as a blue line (see arrow in (a)). The sharp onset of absorption at about 364 nm for the ternary $Zn_{0.92}Mg_{0.08}O$ is an essential feature of the DBR functionality. It allows to operate at wavelengths close to the excitonic resonance and therefore, to achieve a large index contrast. The sophisticated design establishes also a small gap between absorption and stop band for non-resonant excitation of a ZnO active layer in a potential MC. As before, the spectral position of the stop band is shifted to longer wavelengths for thicker $\lambda/4$-layers (Figure 6.4 (b)). In the transparent region, the spectra can be again well modeled by transfer matrix calculations (see red-dashed lines) using the RI parameters for $Zn_{0.92}Mg_{0.08}O$ presented in the next section.

6.4. Theoretical description and range of operation

To model the experimental data by transfer matrix calculations (details can be found in Appendix A), the RI dispersion is described by a first-order Sellmeier equation,

$$n(\lambda) = \sqrt{A + \frac{B\lambda^2}{\lambda^2 - C^2}}, \tag{6.1}$$

and absorption is neglected. The RI dispersion for ZnO is well established and the parameters A, B, and C shown in Table 6.1 result from a least-squares fit of Equation 6.1 to the data of Reference [8]. For ZnMgO alloys the situation is less clear. The available RI literature data differ strongly and cover only a part of the relevant spectral range [73, 95]. The Sellmeier parameters from Reference [73] were used as a starting point for the $x = 0.35$ ZnMgO-layer of DBR type 1. The RI parameters were then varied in a way to obtain maximum agreement between experiment and theory. This was done simultaneously for all experimentally realized DBRs of type 1 (six different DBRs). The resulting dispersion curve is in reasonable agreement with Reference [73].
For DBRs of type 2, the situation is more difficult, as no RI parameters for the high RI layer ($x = 0.08$) are reported in literature. However, the parameters for the low RI layer are now available by the above-described procedure. To find parameters for the second layer, the Sellmeier resonance (parameter C) of ZnO is shifted by an amount similar to the band gap change of an $x = 0.08$ ZnMgO alloy, which produces already reasonable agreement between experiment and theory. Using this as a starting point, the high RI parameters were again varied to obtain maximum agreement between experiment and theory for all realized DBRs of type 2 (four different DBRs).
The ZnO RI parameters at 5 K result from a least-squares fit of Equation 6.1 to the data of Reference [96] in a wavelength range from 400 nm to 500 nm. For the ZnMgO alloys, the room temperature parameters were used as a starting point. They were then varied in a way to obtain maximum agreement between the experimental results (obtained at 5 K) and theory for all realized DBRs. Table 6.1 summarizes the obtained Sellmeier parameters.

x	A	B	C (nm)
0.00	3.21 (3.16)	0.550 (0.568)	337.4 (331.5)
0.08	3.13 (3.15)	0.530 (0.529)	317.4 (312.4)
0.35	1.00 (0.98)	2.290 (2.275)	180.0 (177.0)

Table 6.1: Sellmeier values A, B and C for DBR layers with Mg content x at $T = 295$ K ($T = 5$ K in parentheses).

As demonstrated in the previous section, the transfer matrix model reproduces the transmission spectra for all DBRs in the particular spectral range very well. However, it is worth to mention that the description of the RI dispersion by a first-order Sellmeier equation is only accurate in a limited spectral range. Especially close to the excitonic

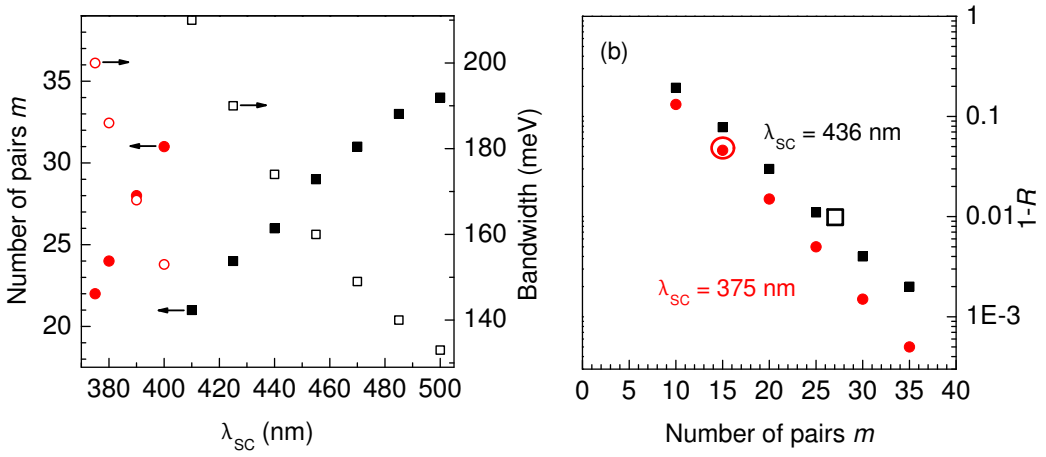

Figure 6.5: Calculated properties of DBR types 1 (black squares) and 2 (red circles). (a) Number of mirror pairs m required to achieve $R = 0.99$ (full symbols, left axis) and width of the stop band (open symbols, right axis) as a function of λ_{SC}. (b) Variation of reflectivity with mirror pair number at fixed λ_{SC}. Experimental results for DBRs shown in Figure 6.3 (b) and Figure 6.4 (a) are marked by open symbols.

resonance, this range can be very narrow. Therefore, validity of the parameters A, B, and C is only given in the investigated wavelength range (see Figure 6.3 and 6.4). Moreover, the central aim of the procedure presented above is to describe the obtained spectra as well as to be able to design more complex structures and not to give exact values of RI parameters for ZnMgO alloys. There are other techniques available to obtain the RI parameters with high accuracy.

The range of operation of DBR types 1 and 2 can be explored theoretically with the help of the RI dispersion curves. Figure 6.5 collects results of respective calculations using the room temperature parameters. The number of mirror pairs m required for $R = 0.99$ and the spectral width of the stop band of such a DBR are depicted in Figure 6.5 (a) as a function of λ_{SC}. On the high-energy side, the application of a given DBR is limited by the onset of absorption. An increasing number of mirror pairs is required for longer wavelengths as a result of a decreasing RI contrast between the layers. This is also manifested by a reduction of the stop band width. However, with less than 35 mirror pairs (equivalent to a DBR thickness $\lesssim 4$ μm), high reflectivity DBRs can be realized, which cover a wavelength range from 375 nm up to 500 nm and exhibit a stop band spectrally broader than 130 meV. For a small λ_{SC}, i.e., DBRs that do not work too far off the excitonic resonance of the high RI material, the index contrast is large enough to generate DBRs with a stop band width $\gtrsim 200$ meV. In such a case, a very high reflectivity can be achieved with only a moderate number of mirror pairs. As shown in Fig. 6.5 (b), a 35 mirror pair type 1 DBR operating at $\lambda_{SC} = 436$ nm can theoretically exhibit a reflectivity of 0.998, and a type-2 DBR with $\lambda_{SC} = 375$ nm reaches approximately the same value with only 30 mirror pairs.

6.5. Conclusion and outlook

The fabrication of high-quality DBRs based on ZnO and $Zn_{1-x}Mg_xO$ layers grown by MBE has been accomplished for the first time. The key is the ability for growth of high-quality single-phase wurtzite-type ZnMgO-layers with a Mg concentration of $x = 0.35$ under non-equilibrium growth conditions. The refractive index of such an alloy is already significantly reduced compared to that of ZnO which allows to realize highly reflective DBRs with only a moderate number of mirror pairs in the wavelength range from 375 to 500 nm.
In principle, the stop band can be shifted to higher energies if the amount of magnesium in the high RI layer of DBR type 2 is enhanced ($x > 0.08$). However, in this case the index contrast between the layers is smaller and the overall reflectivity as well as the width of the stop band are reduced. For DBRs of type 1 the decrease of the RI contrast in the green spectral range can be overcome by using ZnCdO with an adequate Cd concentration instead of ZnO as the high RI material.
The optical properties of all fabricated DBRs can be well described by the transfer matrix model using the obtained material parameters. This makes the design of MCs possible and allows for prediction of their optical properties, as it will be demonstrated in the next chapter. However, verification of the material parameters by other experimental techniques, e.g., ellipsometry, should be carried out.

7. All monolithic ZnO-based microcavities

7.1. Introduction

During the past decades, semiconductor based MCs have been a subject of extensive research [45]. They have become of enormous technological importance, e.g., in VCSEL devices. Further they allow to study fundamental aspects of the strong coupling between photons and excitons. In this regard, pioneering work has been done on GaAs-based MCs by Weisbuch *et al.* [97]. The quest has led to the discovery of many fascinating effects in CdTe and GaAs based MQW MCs, such as optical parametric oscillation [98, 99, 100], Bose-Einstein condensation [101, 102], and polariton suprafluidity [103]. However, the relatively small exciton binding energy of these materials limits the effects to cryogenic temperatures. Hence, wide band gap semiconductors like GaN and ZnO with large oscillator strength and excitonic binding energy went into focus. VCSELs based on GaN and its alloys have reached a promising stage of development [104] and strong exciton-photon coupling at room temperature has been demonstrated in GaN-based MCs [105, 106]. In principle, with ZnO-based alloys a quite similar spectral range can be covered as with the (Al,In,Ga)N heterosystem (see Figure 1.1). Room temperature lasing of ZnO/ZnMgO (see, e.g., [5] and references therein) and ZnCdO/ZnO (see Chapter 4) MQW structures has been demonstrated from UV to green wavelengths. In the strong coupling regime, ZnO was predicted to be even superior due to its high oscillator strength and binding energy [107, 108]. While in the GaAs and CdTe systems all monolithic MCs with QWs as active zone are frequently employed; strong coupling in ZnO has so far only been reported for hybrid MCs consisting of, e.g., an epitaxially grown GaN-based bottom DBR, a top dielectric DBR and a ZnO bulk active layer [87, 109, 110]. However, MQW structures can offer various advantages over bulk material, such as an enhanced binding energy and oscillator strength, tunability of the exciton resonance, and the possibility to position the QWs at the electric field antinodes of the MC. Their growth is more challenging though, since QWs usually suffer from inhomogeneous broadening.
In the following, it will be shown that, based on the results of the previous chapter, excellent all monolithic ZnO-based MCs with QWs as active zone can be fabricated by MBE. They are of high structural quality and the optical properties of the QWs keep up with those of standard ZnO QW structures. It will be further demonstrated that strong exciton-photon coupling is obtained in such a MC up to a temperature of about 150 K. The temperature range is just limited by the design of the particular sample and can be extended if the number of QWs is increased. At room temperature, VCSEL action in the near UV spectral range is demonstrated for appropriately designed MCs.
The results of this chapter have been published in Reference [94, 111].

7.2. Design and basic properties

The MCs under study are grown on the *a*-plane of sapphire under the growth conditions described in Section 6.2. No additional annealing steps are performed and the whole sample is grown without interruption. Again, the substrates are always positioned at the same place on the Mo holder before growth of a MC. Any deviation from this position results in a different growth rate and hence undesired optical properties. However, growth on a larger wafer (larger than 8 x 8 mm^2) or a second substrate attached to the Mo holder, allow for a larger detuning range of the MC emission which might be of interest in some particular cases.
As depicted in Figure 7.1 (a) the MCs consist of type 2 DBRs (without the $\lambda/4$-thick

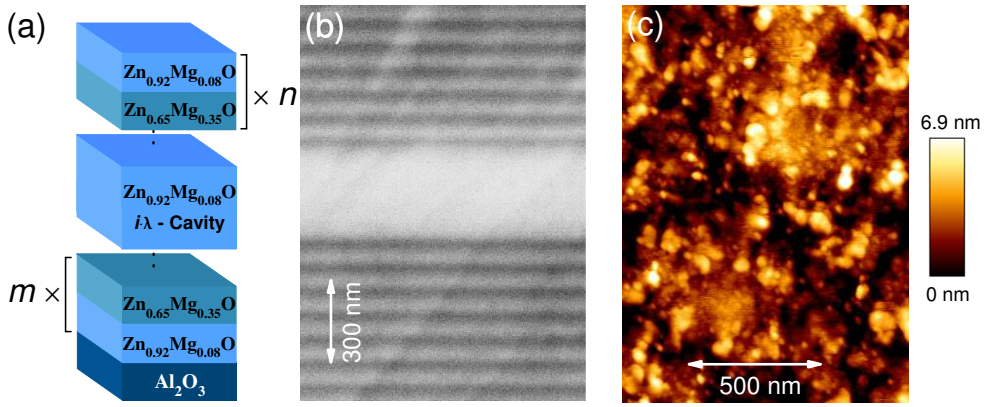

Figure 7.1: Basic design and structural properties of ZnO-based MCs. (a) Schematic layout (not true to scale). (b) Cross section SEM image. (c) Surface AFM image ($m = 28$, $n = 25$, $i = 2$).

cap layer) with n and m layer pairs as upper and lower mirrors, respectively. The $Zn_{0.92}Mg_{0.08}O$ cavity of length $i \cdot \lambda$ ($i = 1, 2$) contains $4{\cdot}i$ ZnO QWs which are symmetrically positioned in the cavity near the electric field antinodes (see Figure 2.6 (c)). The cross section SEM image of a $2{\cdot}\lambda$ cavity and some layer pairs of upper and lower DBR is shown in Figure 7.1 (b). The interface between cavity and DBR layers is flat and well defined (the streaks visible in the SEM image are related to the topology of the breaking edge). Note, that the resolution of the microscope prevents visibility of the QWs. The surface of the 5 μm-thick MC is flat within some nanometers as shown in Figure 7.1. The root mean square roughness over a scan area of 2 x 2 μm^2 amounts to 1.4 nm, which strongly suppresses scattering of light.

Quantum well photoluminescence and microcavity inhomogeneities

Figure 7.2 summarizes basic optical properties of a $m = 28$, $n = 25$ and $i = 2$ MC. The MQW PL is excited by the 355 nm line of a Nd:YVO_4 laser. The emission at low and room temperature recorded from the edge of the MC is drawn in Figure 7.2 (a). At $T = 7$ K the full width at half maximum (FWHM) of the MQW PL is 10 meV.

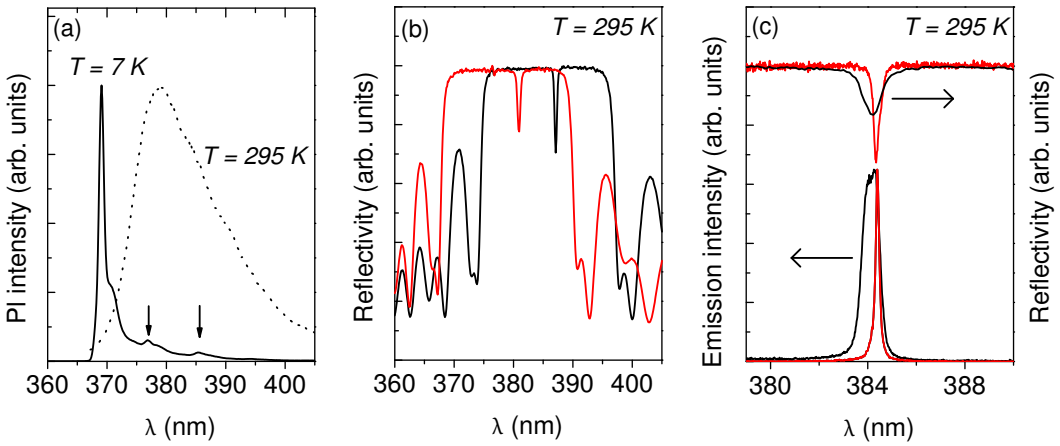

Figure 7.2: Optical properties of a ZnO-based MC with $m = 28$, $n = 25$ and $i = 2$. (a) MQW edge PL at $T = 7$ K and $T = 295$ K (dotted line). Phonon replica are marked by arrows. (b) Maximum detuned reflectivity across the sample. (c) Reflectivity (right axis) and PL (left axis) obtained for a spot of 500 x 500 μm (black curves) and excitation through a microscope objective (red curve). Excitation is performed with the 355 nm line of the Nd:YVO_4 laser. In (a) the excitation intensity is 1 W/cm^2 and in (c) 1 W/cm^2 and 100 W/cm^2 for macroscopic and microscopic excitation, respectively.

This value is comparable to similar MQWs grown on a 600 nm ZnMgO buffer layer [49], implying that the optical quality of the MQW did not deteriorate notably by growth on the 2.6 μm thick lower DBR. Phonon replica appearing 70 meV and 141 meV below the maximum PL peak energy are also found in the low temperature edge emission (marked by arrows in Figure 7.2 (a)). At room temperature, a FWHM of 135 meV of the MQW PL is found. Note that the room temperature MQW PL can still be excited by the 355 nm line, although the absorbance of DBRs type 2 is already large at this wavelength (see Figure 6.4 in section 6.3).
The influence of sample inhomogeneities on the optical properties of the ZnO-based MC is exemplified in Figure 7.2 (b) and (c). Figure 7.2 (b) shows normal incidence reflectivity spectra obtained from opposite corners of the 8 x 8 mm^2 sample. As a result of the growth related layer thickness gradient λ_{SC} as well as the cavity resonance wavelength are shifted by approximately 8 nm. The large-area reflectivity and PL spectra (size of the excitation spot: 500 x 500 μm^2) shown as black curves in Figure 7.2 (c) therefore indicate an inhomogeneous broadening of the cavity mode with a FWHM of $\triangle E = 7$ meV and hence a quality factor of Q $= \frac{E}{\Delta E} \approx 460$. Using a microscope objective with a 20x magnification the probed area in PL and reflectivity can be strongly reduced (red curves in Figure 7.2 (c)). A FWHM of the cavity mode of $\triangle E = 2$ meV is found when investigating the reflected light from a 40 x 40 μm^2 sized spot. A similar value is found in micro PL where the excitation region is further substantially reduced to 2 x 2 μm^2, indicating that homogenous broadening of the cavity mode prevails for excitation areas in the 40 x 40 μm^2-size range. Thus, a quality factor of Q $\approx$ 1600 is found.

7.3. Strong exciton-photon coupling

In this section, it is demonstrated that strong exciton-photon coupling is obtained in a ZnO-based MC up to a temperature of $T \approx 150$ K. Angle resolved reflectivity and transmission spectroscopy is used to determine the MC dispersion in absorption between 5 K and 300 K. For reference, absorption spectra of a similar MQW structure without cavity are recorded and the results are used to simulate the MC properties with the Transfer-Matrix-Method (see Appendix A).
Both samples are grown on the *a*-plane of sapphire under similar conditions. The MC sample (Sample A) contains a λ-cavity which includes four ZnO/$Zn_{0.92}Mg_{0.08}O$ QWs with a width of 3.5 nm. The cavity is sandwiched between $n = 18$ and $m = 20$ layer pairs of DBR type 2. The reference MQW structure (Sample B) consists of five 3.7 nm wide ZnO QWs with 11 nm wide $Zn_{0.92}Mg_{0.08}O$ barriers grown on a 670 nm $Zn_{0.92}Mg_{0.08}O$ buffer and capped by 37 nm of the barrier material.
Angle resolved reflectivity and transmission of Sample A are recorded with the goniometer setup described in Section 3.2. The spectra collected at 5 K from a 80 x 80 μm^2 spot with transverse-electric (TE) polarized light are depicted in Figure 7.3 (a) and (b). It is confirmed that $R + \mathcal{T} = 1.00 \pm 0.02$ holds in the transparent spectral region of the MC. The calculated absorption $A = 1 - R - \mathcal{T}$ is shown in Figure 7.3 (c). At the given sample position, resonance of the photon cavity mode with the exciton is achieved at an angle of $\theta = 32°$ ($\sin\theta = 0.53$). An anticrossing in the dispersion relation with the occurrence of both upper and lower polariton branches is observed in R, as well as in A. The minimum energy splitting between the branches in A equals $\Omega_R = 26$ meV.
With the help of the Transfer-Matrix-Method, a detailed account of the MC response can be given. The refractive index dispersion $n(E)$ of the DBR layers is again described by first-order Sellmeier relation (parameters are found in Table 6.1). For the ZnO QWs, the imaginary $\kappa(E)$ of the complex index of refraction near the exciton resonance is taken from the absorption spectrum $\alpha(E)$ of sample B at 5 K (see Figure 7.4). The real part $n(E)$ is obtained by modeling $\alpha(E)$ with a single Voigt profile (see Appendix B) and a band edge, assuming a (in)homogeneous linewidth of $2\gamma_h = 2$ meV ($2\gamma_i = 17$ meV), a longitudinal-transverse splitting of $\Delta_{LT} = 6.5$ meV and a background refractive index of $n_b = 2.4$. Very good agreement between experiment (Figs. 2(a), (b), and (c)) and Transfer-Matrix-Method (Figs. 2(d), (e), and (f)) is achieved for R, $\mathcal{T}$, and A, respectively. The calculated polariton branches shown in Figure 7.3, for example, agree with experiment within 5 meV or less.
While at low temperature for a properly designed sample, lower and upper polariton branches can clearly be resolved, identification of strong coupling at higher temperature is more challenging. The polariton branches near the exciton resonance are broad, and the upper branch is strongly damped by higher excitonic states. In Figure 7.4 the continuous evolution of the MC dispersion and its transition from strong to weak coupling is carefully studied between 5 K and 200 K in steps of 50 K. To begin with, the normal incidence absorption of the bare MQW (sample B) is measured, see Figure 7.4 (a). At 5 K, the dominant peak in the spectrum is attributed to the B exciton, while the A exciton positioned 8 meV below is visible as a shoulder. The second shoulder appearing at

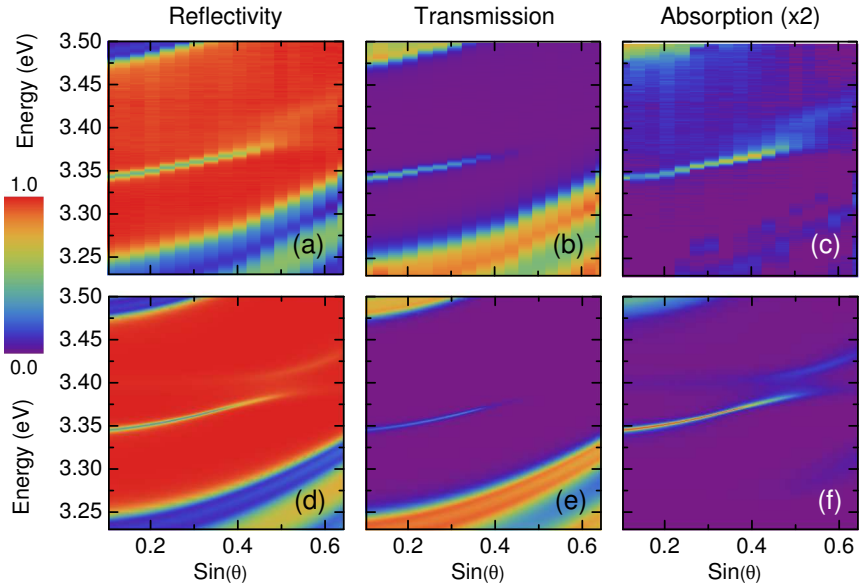

Figure 7.3: Angle resolved reflectivity, transmission and absorption spectra of the MC in TE polarization a $T = 5$ K. Experimental and simulated results are shown in (a), (b), (c), and (d), (e), (f), respectively. Absorption data are multiplied by a factor of 2 for better visibility

3.379 eV is attributed to negatively charged trions [27]. Both A and B excitons exhibit an inhomogeneous broadening due to QW thickness and barrier composition fluctuations with a FWHM of about 10 meV each. At higher T, phonon induced homogeneous broadening becomes dominant. It is confirmed that the excitonic ground-state absorption is well-described by a single Voigt profile, when assuming a constant inhomogeneous linewidth $2\gamma_\mathrm{i} = 17$ meV and the temperature dependent homogeneous linewidth $2\gamma_\mathrm{h}(T)$ from Reference [112] (see Figure 7.4 (b), dash-dotted and dashed lines, respectively). Microcavity absorption spectra at angles around the exciton-photon resonance are shown in Figure 7.4 (c), (d), and (e) for $T = 5$ K, 100 K, and 200 K, respectively. The dashed lines indicate the spectral position of the uncoupled excitonic absorption maximum $E_\mathrm{x}(T)$. $E_\mathrm{x}(5\,\mathrm{K})$ is set to the center between the upper and lower polariton branches at the resonance angle $\theta_\mathrm{r} = 32°$, and for higher T, it is red-shifted by an amount obtained from Figure 7.4 (a). The absorption spectra closest to resonance are highlighted in bold. To correctly interpret the MC data, the different origin of the excitonic linewidth $2\gamma_\mathrm{x}$ at low and high temperatures has to be taken into account. At 5 K, a pronounced splitting Ω_r is observed in absorption, so strong coupling is present in the MC, but inhomogeneous broadening prevails $\gamma_\mathrm{x} \approx \gamma_\mathrm{i}$. Homogeneous broadening dominates the exciton linewidth $\gamma_\mathrm{x} \approx \gamma_\mathrm{h}$ at $T \geq 200$ K. Ω_R can then be described by [45]:

$$\Omega_\mathrm{R} = 2\sqrt{V^2 - (\gamma_\mathrm{x}^2 + \gamma_\mathrm{c}^2)/2} \tag{7.1}$$

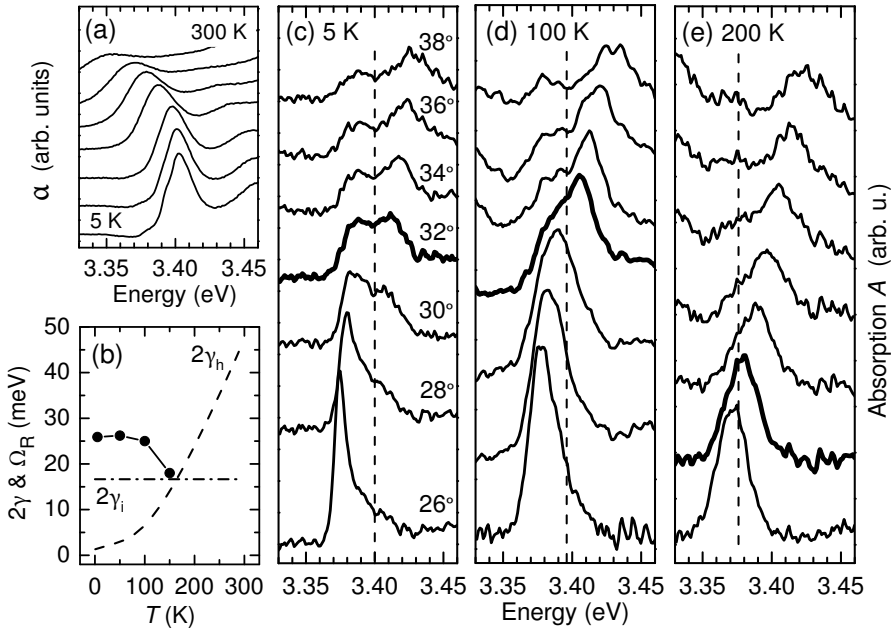

Figure 7.4: Transition from strong to weak exciton-photon coupling in the MC. (a) Temperature dependent excitonic absorption of the bare ZnO MQW (sample B) in steps of 50 K. (b) Inhomogeneous ($2\gamma_\mathrm{i}$, dash-dotted line) and homogeneous ($2\gamma_\mathrm{h}$, dashed line) Voigt model linewidths to describe the bare MQW absorption, as well as splitting Ω_R between the MC polariton branches at resonance (circles) vs. T. (c-e) Angle resolved MC absorption spectra in the vicinity of the exciton-photon resonance at $T = 5$ K, 100 K, and 200 K, respectively. The dashed lines mark the uncoupled exciton resonance.

where V and γ_c are the exciton-photon coupling strength and the homogeneous cavity mode broadening, respectively. The condition for strong exciton-photon coupling $V^2 > (\gamma_\mathrm{x}^2 + \gamma_\mathrm{c}^2)/2$ is then identical to a finite splitting in absorption Ω_R. Hence, from the observation of vanishing Ω_R at 200 K in Figure 7.4 (e), it can be concluded that the strong coupling regime is lost at this temperature. Interestingly, the transition from strong to weak coupling is far from being abrupt: At angles $\theta < \theta_\mathrm{r}$, the visibility of the upper branch continuously diminishes with T, while for $\theta > \theta_\mathrm{r}$ the lower branch remains visible, but shifts onto the bare exciton absorption. The temperature dependence of Ω_R is included by circles in Figure 7.4 (b).

As shown in Figure 7.5 (a), no signs of the strong coupling regime remain at 300 K, only the unsplit cavity resonance is observed. Using the room temperature MQW absorption spectrum from Figure 7.5 (a), experimental results can again be well reproduced by the Transfer-Matrix-Method. For this purpose, the MQW dielectric function at 300 K is determined in the same way as for 5 K. The background refractive index is set to $n_\mathrm{b} = 2.18$. In order to estimate the potential of the monolithic MC for strong coupling at room temperature, the QW number is increased for the Transfer-Matrix-Method by a reasonable factor of 3, and thereby the coupling strength by a factor of $\sqrt{3}$ [45]. From

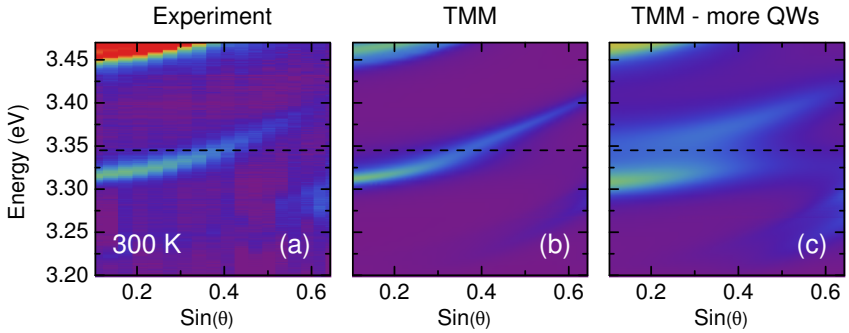

Figure 7.5: Microcavity absorption at 300 K. (a) Experimental results. (b) Calculation by Transfer-Matrix-Method. (c) Transfer-Matrix-Method calculation for a MC containing three times more QWs. The dashed line indicates the uncoupled exciton resonance, the color scale is identical to Figure 7.3.

the reappearance of the two polariton branches in Figure 7.5 (c), it can be concluded that the all monolithic approach is in fact suited to reach the strong coupling regime, even though the effective cavity length is larger than in an analogous design involving dielectric DBRs with a higher refractive index contrast. Moreover, the optical quality of the QWs is such that both polariton branches should be observable, allowing for direct experimental access to the splitting of the branches, and hence to the coupling strength.

7.4. Room temperature vertical cavity surface emitting laser action

Based on the results presented in Chapter 6 a design for a ZnO-based VCSEL with a realistic threshold gain can be defined. The sample under study consists of a 2·λ MC containing eight 4 nm wide ZnO/$Zn_{0.92}Mg_{0.08}O$ quantum wells. As upper and lower mirrors $n = 25$ and $m = 28$ type 2 DBRs are used. Previous studies [28] on the room temperature laser action of such MQW structures have revealed that the bandwidth where significant gain occurs is more than 50 meV and material gain values of some 10^3 cm^{-1} can be obtained for excitation intensities in the 100 kW/cm^2 range. Typically, the optical gain emerges on the low-energy side of the spontaneous emission PL band at about 380 nm. The individual layer thicknesses of the MC are designed for that spectral range. The number of DBR layer pairs as well as the total thickness of the active material result in a threshold gain of approximately $g_{th} = 2200$ cm^{-1}, as calculated by the Transfer-Matrix-Method.
The structure is grown on two 8 x 8 mm^2 *a*-plane sapphire substrates. Sample 1 is placed on the standard position on the Mo holder, while Sample 2 is attached at a slightly different position. No indication of strong exciton-photon coupling at room temperature is found in angle dependent absorption measurements. Optical pumping is performed under normal incidence by the excimer pumped dye laser system described in Section 3.2.1. The excitation spot is 60 μm in diameter and the sample is pumped at a wavelength of 364 nm.
In the beginning, the optical spectra acquired at the center of Sample 1 are discussed. Figure 7.6 (a) collects the normal incidence large area reflectivity (right axis), surface emission spectra at excitation intensities of $I = 100$ kW/cm^2 and $I = 200$ kW/cm^2, as well as the low-density PL (left axis) of the MQW collected from the edge of the sample. The reflectivity spectrum confirms successful growth of the MC. As can be seen in Figure 7.6 (a), the cavity resonance appears at 384 nm on the low-energy side of the spontaneous emission PL band.
Comparing the emission at $I = 100$ kW/cm^2 and $I = 200$ kW/cm^2, two strong indications for emergence of VCSEL action are worth to notice: First the emission intensity increases by more than two orders of magnitude and second, its FWHM decrease abruptly by a factor of 4. The evolution of both quantities with excitation power is depicted in Figure 7.6 (b), signifying a well-defined threshold at $I = 190$ kW/cm^2. Above threshold, the emission is restricted to a narrow cone about the surface normal with an angular FWHM of 4 ° only, as can be seen in Figure 7.6 (c). Additionally, it is found that the emission above threshold becomes strongly linearly polarized, probably due to the anisotropy of the sapphire substrate. The slight shift observed between the emission peaks below and above threshold might be due to changes in the RIs.
The inhomogeneities of the MC should allow for observation of VCSEL action in a relatively broad spectral range (compare Figure 7.2 (b) in Section 7.2). However, a spectral overlap of the optical gain of the MQW and the cavity mode is required. While a layer thickness deviation in the order of some percent strongly affects the optical properties

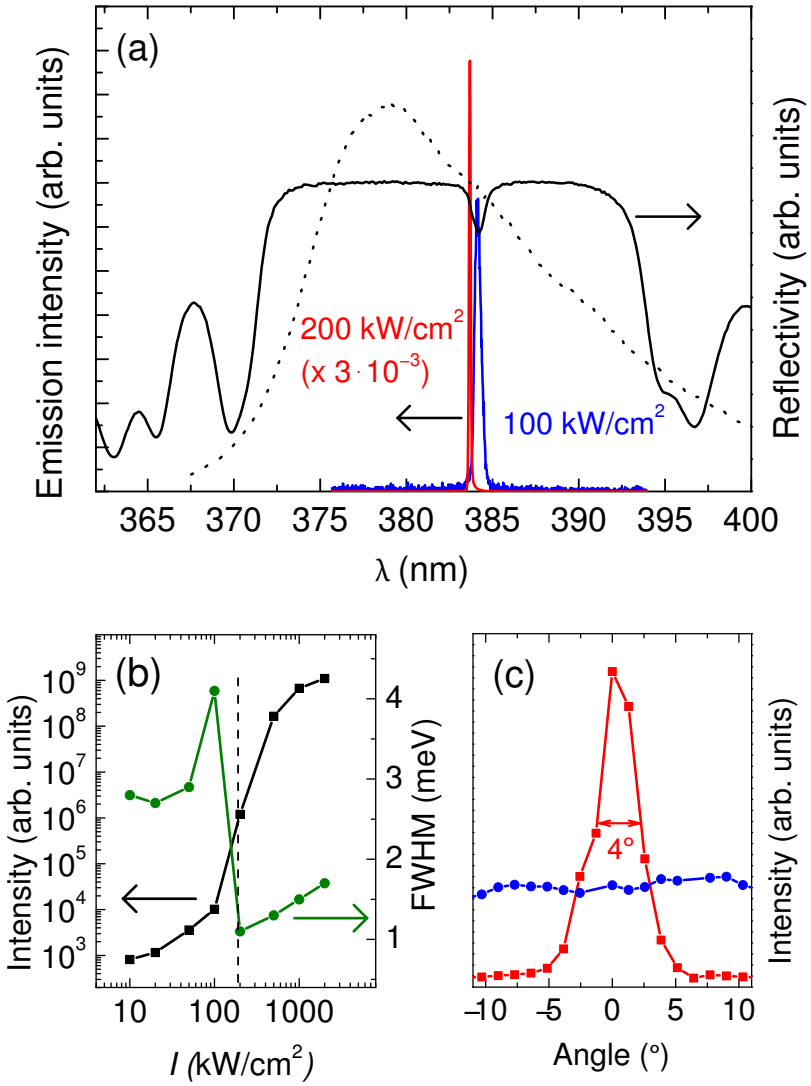

Figure 7.6: Optical properties of a ZnO-based VCSEL device with parameters $m = 28$, $n = 25$ and $i = 2$. (a) Normal incidence reflectivity (black curve, right axis), surface emission (left axis) for $I = 100$ kW/cm^2 (blue curve) and $I = 200$ kW/cm^2 (red curve), and low-density MQW edge PL (black dotted curve). (b) Integrated surface emission intensity (black curve, left axis) and FWHM (green curve, right axis) as a function of I. The lasing threshold $I_{\mathrm{th}} = 190$ kW/cm^2 is marked by a dashed line. (c) Angle dependent, spectrally integrated emission intensity at $I = 100$ kW/cm^2 (blue curve) and $I = 200$ kW/cm^2 (red curve).

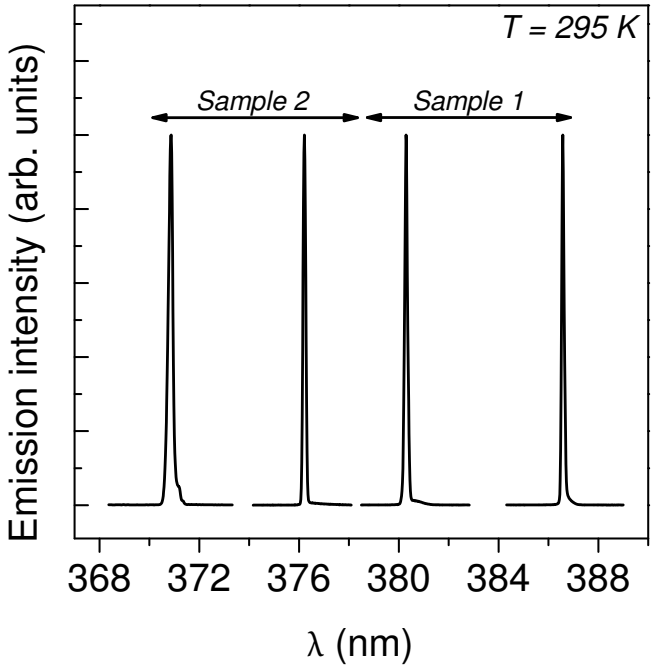

Figure 7.7: VCSEL emission above lasing threshold for various MC resonance wavelengths. The arrows indicate the accessible wavelength range of the respective sample. The pump level is always slightly above threshold. Excitation intensity I and pump wavelength λ_{exc} from left to right: ($I = 2500\text{kW/cm}^2$, $\lambda_{\text{exc}} = 358$ nm); ($I = 750\text{kW/cm}^2$, $\lambda_{\text{exc}} = 360$ nm); ($I = 240\text{kW/cm}^2$, $\lambda_{\text{exc}} = 362$ nm); ($I = 260\text{kW/cm}^2$, $\lambda_{\text{exc}} = 364$ nm).

of a MC, the effect on the spectral position of the optical gain of a 4 nm wide QW is negligible.

Figure 7.7 depicts selected emission spectra of Sample 1 and 2 recorded slightly above threshold. It is possible to tune the laser emission of each sample by approximately 8 nm via excitation of different positions. The blue-shifted emission of Sample 2 is obviously a result of a lower growth rate at the particular position in the growth chamber. Making use of both samples, VCSEL action in a wavelength range from 371 nm to 387 nm is demonstrated. However, the excitation intensity necessary to achieve lasing is very high for emission wavelengths smaller than 380 nm, although the DBR reflectivity in this spectral range increases (see Figure 6.5 in Section 6.4). It is not clear whether the larger pump power reflects a decaying optical gain in the particular spectral range or is just a result of the onset of absorption of the excitation laser by the DBR mirrors for $\lambda_{\text{exc}} < 364$ nm[1].

[1]Tuning of the excitation laser to shorter wavelengths is necessary in order to avoid excitation into the stop band.

7.5. Conclusion and outlook

In this chapter, it has been demonstrated that all monolithic ZnO-based MCs containing ZnO/ZnMgO-based QWs as active zone can be fabricated by MBE. The MCs exhibit a high structural quality, and a Q factor of approximately 1600 has been found for the sample with the largest number of mirror pairs. It was further shown that these MCs are capable of strong exciton-photon coupling. For the present design, the strong coupling regime is limited to cryogenic temperatures where inhomogeneous broadening of the exciton state is predominant. The temperature-induced homogeneous broadening destroys the strong coupling above 150 K. Increasing the number of QWs or their oscillator strength will allow to overcome this limitation. At room temperature VCSEL action in the near UV spectral range is achieved for appropriately designed MCs. The extension of VCSEL action to the visible wavelength range should be possible for MCs containing ZnCdO/ZnO QWs as active zone.

8. Summary

This thesis has demonstrated that ZnO and its alloys are indeed materials with considerable potential for semiconductor laser devices operating in the UV as well as in the visible spectral range. The ternary ZnCdO alloy allows to tune the lasing wavelength of ZnCdO/ZnO MQW structures from violet to green wavelengths. These QW structures suffer from large built-in electric fields, and the low-density PL is governed by the quantum-confined Stark effect. However, at moderate excitation intensities in the 10 kW/cm^2 range screening of the polarization charges sets in, and for appropriately designed ZnCdO/ZnO MQW structures lasing at 510 nm at room temperature has been demonstrated. Further investigations show that the optical feedback for lasing is provided by growth imperfections on a macroscopic length scale, and the structures actually exhibit random laser action. Fabrication of micro-resonators allows to study the interplay between cavity and random feedback. The experimental and theoretical analysis show that random feedback generally requires a larger gain than under cavity feedback. Obviously, ZnO-based structures are predestined in this regard because of their large optical gain. The random feedback creates a subtle modal gain distribution that might be of particular importance for the dynamical properties, both with and without cavity. In the second part of this work, it has been shown that DBRs can be fabricated out of ZnO and ZnMgO layers. They are highly reflective in a wavelength range from 375 to 500 nm. The refractive index dispersion of the employed materials has been elaborated allowing for a very good theoretical description of their optical properties by means of the Transfer-Matrix-Method. Based on these efforts, the design and the realization of all monolithic ZnO-based MCs with ZnO QWs as active zone has become feasible. These MCs are of good structural quality and the optical properties of the cavity quantum wells can keep up with those of standard samples. At temperatures below 150 K, strong exciton photon coupling is observed in such MCs. The homogeneous broadening of the QW excitons destroys the strong coupling at higher temperatures. Increasing the number of QWs will allow to overcome this limitation. The cavity dispersion in both regimes can again be well described using the elaborated complex index of refraction of the ZnO QWs. At room temperature, VCSEL action in the near UV spectral range is demonstrated for appropriately designed MCs.

Appendix

A. The Transfer-Matrix-Method

The Transfer-Matrix-Method is a very powerful tool for calculation of the optical properties of multi-layered systems such as transmission and reflection. Here, the equations necessary to calculate the optical properties of DBRs and MCs, are briefly summarized. A full derivation of this method can be found in [113].
Let us consider a TE polarized wave propagating in a homogeneous and non magnetic medium with complex index of refraction $\tilde{n} = n + i\kappa = n + i\alpha/2k_0$. The plane of incidence is taken to be the yz-plane and φ is the angle of incidence. The transverse electric and magnetic field components at $z = 0$ and $z =$ constant are linked through:

$$\begin{pmatrix} E(0) \\ H(0) \end{pmatrix} = M \begin{pmatrix} E(z) \\ H(z) \end{pmatrix} \tag{A.1}$$

by the characteristic matrix M

$$M = \begin{pmatrix} m_{11} & m_{12} \\ m_{21} & m_{22} \end{pmatrix} = \begin{pmatrix} \cos kz & \frac{-i}{p}\sin kz \\ -ip\sin kz & \cos kz \end{pmatrix}$$

with $p = \tilde{n}\cos\varphi$ and $kz = \frac{2\pi}{\lambda}\tilde{n}z\cos\varphi$. If the medium is bounded on both sides by a semi-infinite medium a and b (with index of refraction n_a and n_b) the reflection and transmission coefficients can be calculated by means of the elements of matrix M:

$$r = \frac{(m_{11} + m_{12}p_\mathrm{b})p_\mathrm{a} - (m_{21} + m_{22}p_\mathrm{b})}{(m_{11} + m_{12}p_\mathrm{b})p_\mathrm{a} + (m_{21} + m_{22}p_\mathrm{b})} \tag{A.2}$$

$$t = \frac{2p_\mathrm{a}}{(m_{11} + m_{12}p_\mathrm{b})p_\mathrm{a} + (m_{21} + m_{22}p_\mathrm{b})}. \tag{A.3}$$

For multi-layered systems equation A.1 can be generalized to:

$$\begin{pmatrix} E(0) \\ H(0) \end{pmatrix} = M_1(z_1)M_2(z_2)...M_N(z_N) \begin{pmatrix} E(z_N) \\ H(z_N) \end{pmatrix} = M_{Multi} \begin{pmatrix} E(z_N) \\ H(z_N) \end{pmatrix} \tag{A.4}$$

where r and t can be calculated according to A.2 and A.3.
In order to calculate the threshold gain of the VCSEL sample, α is replaced by a variable gain coefficient $\tilde{n} = n + i\kappa = n - ig/2k_0$. The real part of the RI is taken from the room temperature reference data of Sample B (see Section 7.3). The threshold gain is then numerically found by searching the zero of the denominator in Equation A.3 as a function

of the gain coefficient as well as of λ.

B. Complex index of refraction of ZnO/ZnMgO multiple quantum wells

In Section 7.3, the experimental absorption data of sample B are used in order to get excess to $\kappa(E)$ and $n(E)$ of the microcavity QWs. While $\kappa(E)$ is directly taken from $\alpha(E) = 2\frac{w\kappa}{c}$, $n(E)$ is obtained by modeling the absorption data with a single Voigt profile and a band edge. The effect of inhomogeneous broadening is then taken into account by a Gaussian distribution of the excitonic energies around ω_0. The resonant dielectric susceptibility $\tilde{\chi}(\omega)$ is given by [114]:

$$\tilde{\chi}(\omega) = \frac{i\sqrt{\pi}\Delta_{\mathrm{LT}}\sqrt{\ln 2}}{\gamma_{\mathrm{i}}} e^{-z^2} \mathrm{erfc}(-iz), \tag{B.5}$$

where $\mathrm{erfc}(x)$ is the complementary error function and $z = (\omega - \omega_0 + i\gamma_{\mathrm{h}})(\gamma_{\mathrm{i}}/\sqrt{\ln 2})^{-1}$. The contribution of the band edge is modeled by a series of homogeneously broadened oscillators:

$$\chi_{\mathrm{Band}}(\omega) = A \int_{E_1}^{E_1+\Delta_{\mathrm{Band}}} \frac{dw_0}{\omega_0 - \omega - i\gamma_{\mathrm{Band}}} + C = A \ln(1 - \frac{\Delta_{\mathrm{Band}}}{\omega + i\gamma_{\mathrm{Band}} - E_1}) + C. \tag{B.6}$$

The real and imaginary part of the complex index of refraction are given by:

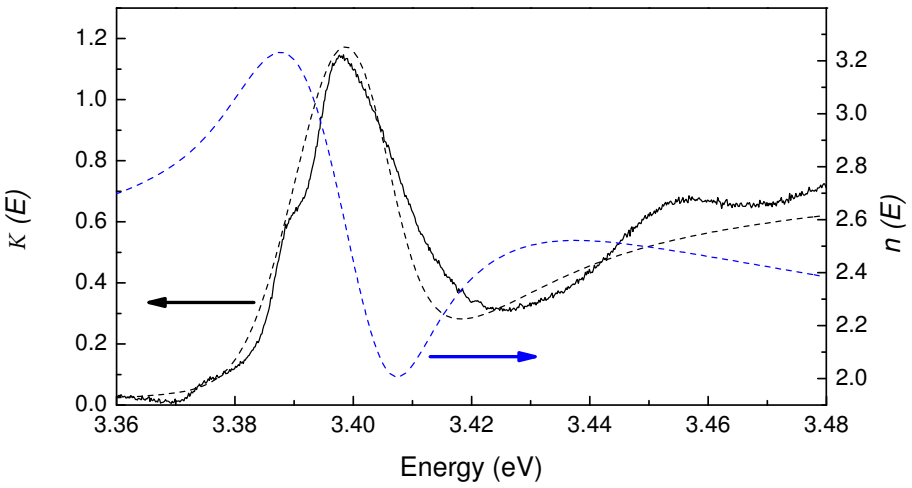

Figure B.1: Complex index of refraction of the reference ZnO/ZnMgO QW structures at 5 K. Experimentally determined $\kappa(E)$ (black solid line) and fit by Equation B.8 (black dashed line) as well as the real part of the index of refraction obtained by Equation B.7 (blue dashed line). Fit parameters are found in Table B.1.

$$n(\omega) = n_{\mathrm{b}}\mathrm{Re}\sqrt{1 + \tilde{\chi}(w) + \chi_{\mathrm{Band}}(w)} \tag{B.7}$$

$$\kappa(\omega) = n_{\mathrm{b}}\mathrm{Im}\sqrt{1 + \tilde{\chi}(w) + \chi_{\mathrm{Band}}(w)}. \tag{B.8}$$

The individual contributions of A- and B-exciton are ignored in this model as well as higher excitonic states. However, the fit parameters for the band gap related part account at least partly for the contribution of higher excitonic states. Figure B.1 summarizes the experimental absorption spectrum at $T = 5$ K and the results obtained by the fitting procedure. The parameters are found in Table B.1.

Δ_{LT}	6.5 meV
γ_{i}	8.5 meV
γ_{h}	1 meV
ω_0	3.396 eV
n_{b}	2.4
A	0.203
C	-0.2
Δ_{Band}	200 meV
γ_{Band}	20 meV
E_1	ω_0+30 meV

Table B.1: Model parameters for the complex index of refraction of the reference ZnO/ZnMgO QW structure at 5 K.

Abbreviations

Abbreviation	Explanation
AFM	Atomic force microscopy
CCD	Charge coupled device
DBR	Distributed Bragg reflector
DFB	Distributed feedback
e-h	Electron-hole
FWHM	Full width at half maximum
LD	Laser diode
LED	Light emitting diode
MBE	Molecular beam epitaxy
MC	Microcavity
MQW	Multiple quantum well
PL	Photoluminescence
QW	Quantum well
RHEED	Reflection high energy electron diffraction
RI	Refractive index
SEM	Scanning electron microscopy
SQW	Single quantum well
UV	Ultraviolet
VCSEL	Vertical cavity surface emitting laser

Bibliography

[1] K. Iga. Vertical-Cavity Surface-Emitting Laser: Its Conception and Evolution. *Japanese Journal of Applied Physics*, **47**:1, 2008.

[2] U. Strauß, A. Avramescu, T. Lermer, D. Queren, A. Gomez-Iglesias, C. Eichler, J. Müller, G. Brüderl, and S. Lutgen. Pros and cons of green InGaN laser on c-plane GaN. *Physica Status Solidi (B)*, **248**:652, 2010.

[3] Ü. Özgür, Ya. I. Alivov, C. Liu, A. Teke, M. A. Reshchikov, S. Doğan, V. Avrutin, S.-J. Cho, and H. Morkoç. A comprehensive review of ZnO materials and devices. *Journal of Applied Physics*, **98**:041301, 2005.

[4] S. Blumstengel, S. Sadofev, J. Puls, and F. Henneberger. An Inorganic/Organic Semiconductor Sandwich Structure Grown by Molecular Beam Epitaxy. *Advanced Materials*, **21**:4850, 2009.

[5] C. F. Klingshirn, B. K. Meyer, A. Waag, A. Hoffmann, and J. Geurts. *Zinc Oxide From Fundamental Properties Towards Novel Applications*. Springer, 2010.

[6] D. Hofstetter, Y. Bonetti, F. R. Giorgetta, A.-H. El-Shaer, A. Bakin, A. Waag, R. Schmidt-Grund, M. Schubert, and M. Grundmann. Demonstration of an ultraviolet zno-based optically pumped third order distributed feedback laser. *Applied Physics Letters*, **91**:111108, 2007.

[7] S. Kalusniak, S. Sadofev, J. Puls, and F. Henneberger. ZnCdO/ZnO - a new heterosystem for green-wavelength semiconductor lasing. *Laser & Photonics Reviews*, **3**:233, 2009.

[8] The Landolt-Börnstein Database:
Semiconductivity: II-VI, I-VII and Semimagnetic Compounds.
Online available at: http://www.springermaterials.com/navigation/.

[9] A. Janotti, D. Segev, and C. G. Van de Walle. Effects of cation d states on the structural and electronic properties of III-nitride and II-oxide wide-band-gap semiconductors. *Physical Review B*, **74**:045202, 2006.

[10] The Landolt-Börnstein Database:
Semiconductivity: Group IV Elements, IV-IV and III-V Compounds.
Online available at: http://www.springermaterials.com/navigation/.

[11] V.Yu. Davydov, A.A. Klochikhin, R.P. Seisyan, V.V. Emtsev, S.V. Ivanov, F. Bechstedt, J. Furthmüller, H. Harima, A.V. Mudryi, J. Aderhold, O. Semchinova, and J. Graul. Absorption and Emission of Hexagonal InN. Evidence of Narrow Fundamental Band Gap. *Physica Status Solidi (B)*, **229**:R1, 2002.

[12] T. Makino, Y. Segawa, M. Kawasaki, A. Ohtomo, R. Shiroki, K. Tamura, and T. Yasuda. Band gap engineering based on $Mg_xZn_{1-x}O$ and $Cd_yZn_{1-y}O$ ternary alloy films. *Applied Physics Letters*, **78**:1237, 2001.

[13] Sergey Sadofiev. Radical-source molecular beam epitaxy of ZnO-based heterostructures. Ph.D. thesis, Humboldt-Universität zu Berlin, 2009.

[14] Govind P. Agrawal and Niloy K. Dutta. *Semiconductor-Lasers*. Van Nostrand Reinhold, 1993.

[15] Weng W. Chow, Stephan W. Koch, and Murray Sargent III. *Semiconductor-Laser Physics*. Springer-Verlag, 1994.

[16] C. Klingshirn. *Semiconductor Optics*. Springer-Verlag, 2007.

[17] C. Klingshirn and H. Haug. Optical properties of highly excited direct gap semiconductors. *Physics Reports*, **70**:315, 1981.

[18] R. Zimmermann. Nonlinear Optics and the Mott Transition in Semiconductors. *Physica Status Solidi (b)*, **146**:371, 1988.

[19] Y. Chen, N. T. Tuan, Y. Segawa, Hang ju Ko, Soon ku Hong, and T. Yao. Stimulated emission and optical gain in ZnO epilayers grown by plasma-assisted molecular-beam epitaxy with buffers. *Applied Physics Letters*, **78**:1469, 2001.

[20] A. Yamamoto, T. Kido, T. Goto, Y. Chen, T. Yao, and A. Kasuya. Dynamics of photoexcited carriers in ZnO epitaxial thin films. *Applied Physics Letters*, **75**:469, 1999.

[21] D. M. Bagnall, Y. F. Chen, Z. Zhu, T. Yao, M. Y. Shen, and T. Goto. High temperature excitonic stimulated emission from ZnO epitaxial layers. *Applied Physics Letters*, **73**:1038, 1998.

[22] J. Ding, H. Jeon, T. Ishihara, M. Hagerott, A. V. Nurmikko, H. Luo, N. Samarth, and J. Furdyna. Excitonic gain and laser emission in ZnSe-based quantum wells. *Physical Review Letters*, **69**:1707, 1992.

[23] F. Kreller, M. Lowisch, J. Puls, and F. Henneberger. Role of Biexcitons in the Stimulated Emission of Wide-Gap II-VI Quantum Wells. *Physical Review Letters*, **75**:2420, 1995.

[24] F. Kreller, J. Puls, and F. Henneberger. Temperature-dependent study of optical gain in (Zn,Cd)Se/ZnSe multiple-quantum-well structures. *Applied Physics Letters*, **69**:2406, 1996.

[25] J. Puls, G. V. Mikhailov, F. Henneberger, D. R. Yakovlev, A. Waag, and W. Faschinger. Laser Action of Trions in a Semiconductor Quantum Well. *Physical Review Letters*, **89**:287402, 2002.

[26] H. D. Sun, T. Makino, Y. Segawa, M. Kawasaki, A. Ohtomo, K. Tamura, and H. Koinuma. Biexciton emission from $ZnO/Zn_{0.74}Mg_{0.26}O$ multiquantum wells. *Applied Physics Letters*, **78**:3385, 2001.

[27] J. Puls, S. Sadofev, and F. Henneberger. Trions in ZnO quantum wells and verification of the valence band ordering. *Physical Review B*, **85**:041307(R), 2012.

[28] J. Cui, S. Sadofev, S. Blumstengel, J. Puls, and F. Henneberger. Optical gain and lasing of ZnO/ZnMgO multiple quantum wells: From low to room temperature. *Applied Physics Letters*, **89**:051108, 2006.

[29] S. Schmitt-Rink, D. S. Chemla, and D. A. B. Miller. Linear and nonlinear optical properties of semiconductor quantum wells. *Advances in Physics*, **38**:89, 1989.

[30] P. Gopal and N. A. Spaldin. Polarization, Piezoelectric Constants, and Elastic Constants of ZnO, MgO, and CdO. *Journal of Electronic Materials*, **35**:538, 2006.

[31] A. Ohtomo, M. Kawasaki, T. Koida, K. Masubuchi, H. Koinuma, Y. Sakurai, Y. Yoshida, T. Yasuda, and Y. Segawa. $Mg_xZn_{1-x}O$ as a II-VI widegap semiconductor alloy. *Applied Physics Letters*, **72**:2466, 1998.

[32] S. F. Chichibu, A. C. Abare, M. S. Minsky, S. Keller, S. B. Fleischer, J. E. Bowers, E. Hu, U. K. Mishra, L. A. Coldren, S. P. DenBaars, , and T. Sota. Effective band gap inhomogeneity and piezoelectric field in InGaN/GaN multiquantum well structures. *Applied Physics Letters*, **73**:2006, 1998.

[33] J. S. Im, H. Kollmer, J. Off, A. Sohmer, F. Scholz, and A. Hangleiter. Reduction of oscillator strength due to piezoelectric fields in $GaN/Al_xGa_{1-x}N$ quantum wells. *Physical Review B*, **57**:R9435, 1998.

[34] P. Lefebvre, A. Morel, M. Gallart, T. Taliercio, J. Allègre, B. Gil, H. Mathieu, B. Damilano, N. Grandjean, , and J. Massies. High internal electric field in a graded-width InGaN/GaN quantum well: Accurate determination by time-resolved photoluminescence spectroscopy. *Applied Physics Letters*, **78**:1252, 2001.

[35] M. Stölzel, J. Kupper, M. Brandt, A. Müller, G. Benndorf, M. Lorenz, and M. Grundmann. Electronic and optical properties of ZnO/(Mg,Zn)O quantum wells with and without a distinct quantum-confined Stark effect. *Journal of Applied Physics*, **111**:063701, 2012.

[36] M. A. Noginov. *Solid-State Random Lasers*. Springer, 2005.

[37] X. Wu, W. Fang, A. Yamilov, A. A. Chabanov, A. A. Asatryan, L. C. Botten, , and H. Cao. Random lasing in weakly scattering systems. *Physical Review A*, **74**:053812, 2006.

[38] H. Cao. Review on latest developments in random lasers with coherent feedback. *Journal of Physics A*, **38**:10497, 2005.

[39] D. S. Wiersma. The physics and applications of random lasers. *Nature Physics*, **4**:359, 2008.

[40] O. Zaitsev and L. Deych. Recent developments in the theory of multimode random lasers. *Journal of Optics*, **12**:024001, 2010.

[41] H. Li and K. Iga, editors. *Vertical-Cavity Surface-Emitting Laser Devices*. Springer, 2003.

[42] S. F. Yu. *Analysis and Design of Vertical Cavity Surface Emitting Lasers*. John Wiley & Sons, 2003.

[43] Raphaël Butté, Gabriel Christmann, Eric Feltin, Antonino Castiglia, Jacques Levrat, Gatien Cosendey, Alexei Altoukhov, Jean-François Carlin, and Nicolas Grandjean. Room temperature polariton lasing in III-nitride microcavities: a comparison with blue GaN-based vertical cavity surface emitting lasers. *Proceedings of SPIE*, **7216**:721619, 2009.

[44] V. Savona, L.C. Andreani, P. Schwendimann, and A. Quattropani. Quantum well excitons in semiconductor microcavities: Unified treatment of weak and strong coupling regimes. *Solid State Communications*, **93**:733, 1995.

[45] B. Deveaud, editor. *Physics of Semiconductor Microcavities: From Fundamentals to Nanoscale Devices*. Wiley-VCH, Weinheim, 2007.

[46] R. Houdré. Early stages of continuous wave experiments on cavity-polaritons. *Physica Status Solidi (b)*, **242**:2167, 2005.

[47] A. Kavokin, J. J. Baumberg, G. Malpuech, and Fabrice P. Laussy. *Microcavities*. Oxford University Press, 2007.

[48] S. Sadofev, S. Blumstengel, J. Cui, J. Puls, S. Rogaschewski, P. Schäfer, Yu. G. Sadofyev, and F. Henneberger. Growth of high-quality ZnMgO epilayers and ZnO/ZnMgO quantum well structures by radical-source molecular-beam epitaxy on sapphire. *Applied Physics Letters*, **87**:091903, 2005.

[49] S. Sadofev, S. Blumstengel, J. Cui, J. Puls, F. Henneberger, R. Schneider, D. Litvinov, and D. Gerthsen. Uniform and Efficient UV-emitting ZnO/ZnMgO Multiple Quantum Wells Grown by Radical-Source Molecular Beam Epitaxy. *Japanese Journal of Applied Physics*, **45**:L1250, 2006.

[50] S. Sadofev, S. Blumstengel, J. Cui, J. Puls, S. Rogaschewski, P. Schäfer, and F. Henneberger. Visible band-gap ZnCdO heterostructures grown by molecular beam epitaxy. *Applied Physics Letters*, **89**:201907, 2006.

[51] Lee Gomes. Elusive Green Laser is Missing Ingredient for Amazing Displays. http://online.wsj.com/article/SB120285999714463727.html, February 2008.

[52] S. Itoh, K. Nakano, and A. Ishibashi. Current status and future prospects of ZnSe-based light-emitting devices. *Journal of Crystal Growth*, **214/215**:1029, 2000.

[53] T. Mukai, M. Yamada, and S. Nakamura. InGaN-based UV/blue/green/amber LEDs. *Proceedings of SPIE*, **6894**:689414, 1999.

[54] K. Okamoto, J. Kashiwagi, T. Tanaka, and M. Kubota. Nonpolar m-plane InGaN multiple quantum well laser diodes with a lasing wavelength of 499.8 nm. *Applied Physics Letters*, **94**:071105, 2009.

[55] Y. Enya, Y. Yoshizumi, T. Kyono, K. Akita, M. Ueno, M. Adachi, T. Sumitomo, S. Tokuyama, T. Ikegami, K. Katayama, and T. Nakamura. 531 nm Green Lasing of InGaN Based Laser Diodes on Semi-Polar $20\bar{2}1$ Free-Standing GaN Substrates. *Applied Physics Express*, **2**:082101, 2009.

[56] A. Tyagi, R. M. Farrell, K. M. Kelchner, C.-Y. Huang, P. S. Hsu, D. A. Haeger, M. T. Hardy, C. Holder, K. Fujito, D. A. Cohen, H. Ohta, J. S. Speck, S. P. DenBaars, and S. Nakamura. AlGaN-Cladding Free Green Semipolar GaN Based Laser Diode with a Lasing Wavelength of 506.4nm. *Applied Physics Letters*, **3**:011002, 2010.

[57] T. Miyoshi, S. Masui, T. Okada, T. Yanamoto, T. Kozaki, S. Nagahama, and T. Mukai. 510-515nm InGaN-Based Green Laser Diodes on c-Plane GaN Substrate. *Applied Physics Express*, **2**:062201, 2009.

[58] A. Avramescu, T. Lermer, J. Müller, S. Tautz, D. Queren, S. Lutgen, and U. Strauß. InGaN laser diodes with 50 mW output power emitting at 515 nm. *Applied Physics Letters*, **95**:071103, 2009.

[59] S. Sadofev, S. Kalusniak, J. Puls, P. Schäfer, S. Blumstengel, and F. Henneberger. Visible-wavelength laser action of ZnCdO/(Zn,Mg)O multiple quantum well structures. *Applied Physics Letters*, **91**:231103, 2007.

[60] S. Sadofev, S. Kalusniak, J. Puls, P. Schäfer, S. Blumstengel, S. Rogaschewski, Y.-H. Fan, and F. Henneberger. ZnCdO/ZnO hetero- and quantum well structures for light-emitting applications. *Proceedings of SPIE*, **6895**:68950C, 2008.

[61] S. Kalusniak, S. Sadofev, J. Puls, H.-J. Wünsche, and F. Henneberger. Polarization fields in (Zn,Cd)O/ZnO quantum well structures. *Physical Review B*, **77**:113312, 2008.

[62] G. Mussler, L. Däweritz, K. H. Ploog, J. W. Tomm, and V. Talalaev. Optimized annealing conditions identified by analysis of radiative recombination in dilute Ga(As,N). *Applied Physics Letters*, **83**:1343, 2003.

[63] Y. Ichimura, K. Kishino, M. Kuramoto, and M. Satake und Atsushi Yoshida. Remarkable improvement in emission efficiency of ZnCdSe/Zn(S)Se leds by thermal annealing. *Journal of Electronic Materials*, **24**:99, 1995.

[64] S. Mackowski, L. M. Smith, H. E. Jackson, W. Heiss, J. Kossut, and G. Karczewski. Optical properties of annealed CdTe self-assembled quantum dots. *Applied Physics Letters*, **83**:254, 2003.

[65] M. K. Chai, S. F. Wee, K. P. Homewood, W. P. Gillin, T. Cloitre, and R. L. Aulombard. An optical study of interdiffusion in ZnSe/ZnCdSe. *Applied Physics Letters*, **69**:1579, 1996.

[66] A. V. Thompson, C. Boutwell, J. W. Mares, W. V. Schoenfeld, A. Osinsky, B. Hertog, J. Q. Xie, S. J. Pearton, and D. P. Norton. Thermal stability of CdZnO/ZnO multi-quantum-wells. *Applied Physics Letters*, **91**:201921, 2007.

[67] G. Benndorf M. Lorenz J. Zúñiga-Pérez M. Grundmann M. Lange, C.P. Dietrich. Thermal stability of ZnO/ZnCdO/ZnO double heterostructures grown by pulsed laser deposition. *Journal of Crystal Growth*, **328**:13, 2011.

[68] Jin Seo Im, H. Kollmer, J. Off, A. Sohmer, F. Scholz, and A. Hangleiter. Reduction of oscillator strength due to piezoelectric fields in $GaN/Al_xGa_{1-x}N$ quantum wells. *Physical Review B*, **57**:9435(R), 1998.

[69] H. Matsui, T. Osone, and H. Tabata. Band alignment and excitonic localization of $ZnO/Cd_{0.08}Zn_{0.92}O$ quantum wells. *Journal of Applied Physics*, **107**:093523, 2010.

[70] This calculation was performed iteratively, using the 1D Poisson-Schrödinger solver of G. Snider.
Online available at: //http://www.nd.edu/~gsnider/.

[71] X. J. Wanga, I. A. Buyanova, W. M. Chen, M. Izadifard, S. Rawal, D. P. Norton, S. J. Pearton, A. Osinsky, J. W. Dong, and Amir Dabiran. Band gap properties of $Zn_{1-x}Cd_xO$ alloys grown by molecular-beam epitaxy. *Applied Physics Letters*, **89**:151909, 2006.

[72] J.-J. Chen, F. Ren, Y. Li, D. P. Norton, S. J. Pearton, A. Osinsky, J. W. Dong, P. P. Chow, and J. F. Weaver. Measurement of $Zn_{0.95}Cd_{0.05}O/ZnO$ (0001) heterojunction band offsets by x-ray photoelectron spectroscopy. *Applied Physics Letters*, **87**:192106, 2005.

[73] C. W. Teng, J. F. Muth, Ü. Özgür, M. J. Bergmann, H. O. Everitt, A. K. Sharma, C. Jin, and J. Narayan. Refractive indices and absorption coefficients of $Mg_xZn_{1-x}O$ alloys. *Applied Physics Letters*, **76**:979, 2000.

[74] T. Ohashi, K. Yamamoto, A. Nakamura, T. Aoki, and J. Temmyo. Optical Properties of Wurtzite $Zn_{1-x}Cd_xO$ Films Grown by Remote-Plasma-Enhanced Metalorganic Chemical Vapor Deposition. *Japanese Journal of Applied Physics*, **46**:2516, 2007.

[75] E.V. Lutsenko, A.V. Danilchyk, N. P. Tarasuk, V. N. Pavlovskii, A. L. Gurskii, G. P. Yablonskii, L. Rahimzadeh Khoshroo, H. Kalisch, R. H. Jansen, Y. Dikme, B. Schineller, and M. Heuken. Optically pumped InGaN/GaN MQW lift-off lasers grown on silicon substrates. *Superlattices and Microstructures*, **41**:400, 2007.

[76] H. Cao, Y. G. Zhao, S. T. Ho, E. W. Seelig, Q. H. Wang, and R. P. H. Chang. Random Laser Action in Semiconductor Powder. *Physical Review Letters*, **82**:2278, 1999.

[77] M.A. Noginov, G. Zhu, I. Fowlkes, and M. Bahoura. GaAs random laser. *Laser Physics Letters*, **1**:291, 2004.

[78] J. Fallert, R. J. B. Dietz, J. Sartor, D. Schneider, C. Klingshirn, and H. Kalt. Co-existence of strongly and weakly localized random laser modes. *Nature Photonics*, **3**:279, 2009.

[79] S. F. Yu, C. Yuen, S. P. Lau, W. I. Park, and G.-C. Yi. Random laser action in ZnO nanorod arrays embedded in ZnO epilayers. *Applied Physics Letters*, **84**:3241, 2004.

[80] H. Y. Yang, S. P. Lau, S. F. Yu, M. Tanemura, T. Okita, H. Hatano, K. S. Teng, and S. P. Wilks. Wavelength-tunable and high-temperature lasing in ZnMgO nanoneedles. *Applied Physics Letters*, **89**:081107, 2006.

[81] F. J. P. Schuurmans, D. Vanmaekelbergh, J. van de Lagemaat, and A. Lagendijk. Strongly Photonic Macroporous Gallium Phosphide Networks. *Science*, **284**:141, 1999.

[82] K. L. van der Molen, R. W. Tjerkstra, A. P. Mosk, and A. Lagendijk. Spatial Extent of Random Laser Modes. *Physical Review Letters*, **98**:143901, 2007.

[83] S. Chu, M. Olmedo, Z. Yang, J. Kong, and J. Liu. Electrically pumped ultraviolet ZnO diode lasers on Si. *Applied Physics Letters*, **93**:181106, 2008.

[84] S. Kalusniak, H. J. Wünsche, and F. Henneberger. Random Semiconductor Lasers: Scattered versus Fabry-Perot Feedback. *Physical Review Letters*, **106**:013901, 2011.

[85] M. C. W. van Rossum and Th. M. Nieuwenhuizen. Multiple scattering of classical waves: microscopy, mesoscopy, and diffusion. *Reviews of Modern Physics*, **71**:313, 1999.

[86] C. F. Bohren and D. R. Huffman. *Absorption and Scattering of Light by Small Particles*. Wiley-VCH, Weinheim, 2004.

[87] J. R. Chen, T. C. Lu, Y. C. Wu, S. C. Lin, W. R. Liu, W. F. Hsieh, C. C. Kuo, and C. C. Lee. Large vacuum Rabi splitting in ZnO-based hybrid microcavities observed at room temperature. *Applied Physics Letters*, **94**:061103, 2009.

[88] R. Schmidt-Grund, B. Rheinländer, C. Czekalla, G. Benndorf, H. Hochmuth, M. Lorenz, and M. Grundmann. Exciton-polariton formation at room temperature in a planar ZnO resonator structure. *Applied Physics B*, **93**:331, 2008.

[89] Chih-Chiang Kao, Y. C. Peng, H. H. Yao, J. Y. Tsai, Y. H. Chang, J. T. Chu, H. W. Huang, T. T. Kao, T. C. Lu, H. C. Kuo, S. C. Wang, and C. F. Lin. Fabrication and performance of blue GaN-based vertical-cavity surface emitting laser employing AlN/GaN and Ta_2O_5/SiO_2 distributed Bragg reflector. *Applied Physics Letters*, **87**:081105, 2005.

[90] C. W. Wilmsen, H. Temkin, and L. A. Coldren, editors. *Vertical-Cavity Surface-Emitting Lasers: Design, Fabrication, Characterization, and Applications*. Cambridge University Press, 2001.

[91] H. Yoshida, M. Kuwabara, Y. Yamashita, K. Uchiyama, and H. Kan. The current status of ultraviolet laser diodes. *Physica Status Solidi (a)*, **7**:1586, 2011.

[92] J. W. Raring, E. M. Hall, M. C. Schmidt, C. Poblenz, B. Li, N. Pfister, D. Kebort, Y.-C. Chang, D. F. Feezell, R. Craig, J. S. Speck, S. P. Denbaars, and S. Nakamura. State-of-the-art continuous-wave InGaN laser diodes in the violet, blue, and green wavelength regimes. *Proceedings of SPIE*, **7686**:76860L, 2010.

[93] R. Butté, E. Feltin, J. Dorsaz, G. Christmann, J.-F. Carlin, N. Grandjean, and M. Ilegems. Recent Progress in the Growth of Highly Reflective Nitride-Based Distributed Bragg Reflectors and Their Use in Microcavities. *Japanese Journal of Applied Physics*, **44**:7207, 2005.

[94] S. Kalusniak, S. Sadofev, S. Halm, and F. Henneberger. Vertical cavity surface emitting laser action of an all monolithic ZnO-based microcavity. *Applied Physics Letters*, **98**:011101, 2011.

[95] R. Schmidt, B. Rheinländer, M. Schubert, D. Spemann, T. Butz, J. Lenzner, E. M. Kaidashev, M. Lorenz, A. Rahm, H. C. Semmelhack, and M. Grundmann. Dielectric functions (1 to 5 ev) of wurtzite $Mg_xZn_{1-x}O$ ($x \leq 0.29$) thin films. *Applied Physics Letters*, **82**:2260, 2003.

[96] Y. S. Park and J. R. Schneider. Index of Refraction of ZnO. *Journal of Applied Physics*, **39**:3049, 1968.

[97] C. Weisbuch, M. Nishioka, A. Ishikawa, and Y. Arakawa. Observation of the coupled exciton-photon mode splitting in a semiconductor quantum microcavity. *Physical Review Letters*, **69**:3314, 1992.

[98] P. G. Savvidis, J. J. Baumberg, R. M. Stevenson, M. S. Skolnick, D. M. Whittaker, and J. S. Roberts. Angle-Resonant Stimulated Polariton Amplifier. *Physical Review Letters*, **84**:1547, 2000.

[99] M. Saba, C. Ciuti, J. Bloch, V. Thierry-Mieg, R. André, Le Si Dang, S. Kundermann, A. Mura, G. Bongiovanni, J. L. Staehli, and B. Deveaud. High-temperature ultrafast polariton parametric amplification in semiconductor microcavities. *Nature (London)*, **414**:731, 2001.

[100] C. Diederichs, J. Tignon, G. Dasbach, C. Ciuti, A. Lemaître, J. Bloch, Ph. Roussignol, and C. Delalande. Parametric oscillation in vertical triple microcavities. *Nature (London)*, **440**:904, 2006.

[101] J. Kasprzak, M. Richard, S. Kundermann, A. Baas, P. Jeambrun, J. M. J. Keeling, F. M. Marchetti, M. H. Szymanska, R. André, J. L. Staehli, V. Savona, P. B. Littlewood, B. Deveaud, and L. S. Dang. Bose-Einstein condensation of exciton polaritons. *Nature (London)*, **443**:409, 2006.

[102] H. Deng, D. Press, S. Götzinger, G. S. Solomon, R. Hey, K. H. Ploog, and Y. Yamamoto. Quantum degenerate exciton-polaritons in thermal equilibrium. *Physical Review Letters*, **97**:146402, 2006.

[103] A. Amo, J. Lefrère, S. Pigeon, C. Adrados, C. Ciuti, I. Carusotto, R. Houdré, E. Giacobino, and A. Bramati. Superfluidity of polaritons in semiconductor microcavities. *Nature Photonics*, **5**:805, 2009.

[104] R. Shimada and H. Morkoç. Wide Bandgap Semiconductor-Based Surface-Emitting Lasers: Recent Progress in GaN-Based Vertical Cavity Surface-Emitting Lasers and GaN-/ZnO-Based Polariton Lasers. *Proceedings of the IEEE*, **98**:1113, 2010.

[105] S. Christopoulos, G. Baldassarri Höger von Högersthal, A. J. D. Grundy, P. G. Lagoudakis, A. V. Kavokin, J. J. Baumberg, G. Christmann, R. Butté, E. Feltin, J.-F. Carlin, and N. Grandjean. Room-Temperature Polariton Lasing in Semiconductor Microcavities. *Physical Review Letters*, **98**:126405, 2007.

[106] E. Feltin, G. Christmann, R. Butté, J.-F. Carlin, M. Mosca, and N. Grandjean. Room temperature polariton luminescence from a GaN/AlGaN quantum well microcavity. *Applied Physics Letters*, **89**:071107, 2006.

[107] M. Zamfirescu, A. Kavokin, B. Gil, G. Malpuech, and M. Kaliteevski. ZnO as a material mostly adapted for the realization of room-temperature polariton lasers. *Physical Review B*, **65**:161205(R), 2002.

[108] S. Faure, T. Guillet, P. Lefebvre, T. Bretagnon, and B. Gil. Comparison of strong coupling regimes in bulk GaAs, GaN, and ZnO semiconductor microcavities. *Physical Review B*, **78**:235323, 2008.

[109] R. Shimada, J. Xie, V. Avrutin, Ü. Özgür, and H. Morkoç. Cavity polaritons in ZnO-based hybrid microcavities. *Applied Physics Letters*, **92**:011127, 2008.

[110] S. Faure, C. Brimont, T. Guillet, T. Bretagnon, B. Gil, F. Médard, D. Lagarde, P. Disseix, J. Leymarie, J. Zu niga Pérez, M. Leroux, E. Frayssinet, J. C. Moreno, F. Semond, and S. Bouchoule. Relaxation and emission of Bragg-mode and cavity-mode polaritons in a ZnO microcavity at room temperature. *Applied Physics Letters*, **95**:121102, 2009.

[111] S. Kalusniak, S. Sadofev, S. Halm, and F. Henneberger. Strong exciton-photon coupling in a monolithic ZnO/(Zn,Mg)O multiple quantum well microcavity. *Applied Physics Letters*, **99**:181121, 2011.

[112] R. Hauschild, H. Priller, M. Decker, J. Brückner, H. Kalt, and C. Klingshirn. Temperature dependent band gap and homogeneous line broadening of the exciton emission in ZnO. *Physica Status Solidi (C)*, **3**:976, 2006.

[113] M. Born and E. Wolf. *Principles of Optics*. Pergamon, Oxford, 6st edition, 1993.

[114] L. C. Andreani, G. Panzarini, A. V. Kavokin, and M. R. Vladimirova. Effect of inhomogeneous broadening on optical properties of excitons in quantum wells. *Physical Review B*, **57**:4670, 1998.

List of Figures

List of Tables

List of Publications

Most of this work has been already published in the following articles:

- *Strong exciton-photon coupling in a monolithic ZnO/(Zn,Mg)O multiple quantum well microcavity*
  S. Halm, S. Kalusniak, S. Sadofev, H.-J. Wünsche, and F. Henneberger
  Appl. Phys. Letters **99**, 181121 (2011)

- *Random semiconductor lasers: Scattered versus Fabry-Perot Feedback*
  S. Kalusniak, H.-J. Wünsche, and F. Henneberger
  Phys. Rev. Letters **106**, 013901 (2011)

- *Vertical cavity surface emitting laser action of an all monolithic ZnO-based microcavity*
  S. Kalusniak, S. Sadofev, S. Halm, and F. Henneberger
  Appl. Phys. Letters **98**, 011101 (2011)

- *ZnCdO/ZnO - a new heterosystem for green-wavelength semiconductor lasing*
  S. Kalusniak, S. Sadofev, J. Puls, and F. Henneberger
  Laser & Photon. Rev. **3**, 233 (2009)

- *Polarization fields in (Zn,Cd)O/ZnO quantum well structures*
  S. Kalusniak, S. Sadofev, J. Puls, H.-J. Wünsche, and F. Henneberger
  Phys. Rev. B **77**, 113312 (2008)

- *ZnCdO/ZnO hetero- and quantum well structures for light-emitting applications*
  S. Sadofev, S. Kalusniak, J. Puls, P. Schäfer, S. Blumstengel, S. Rogaschewski, Y.-H. Fan, and F. Henneberger
  (Invited), Proc. of SPIE, Vol. **6895**, 68950C (2008)

- *Visible-wavelength laser action of ZnCdO /(Zn,Mg)O multiple quantum well structures*
  S. Sadofev, S. Kalusniak, J. Puls, P. Schäfer, S. Blumstengel, and F. Henneberger
  Appl. Phys. Letters **91**, 231103 (2007)

Acknowledgement

This work has been prepared under the supervision of Prof. Dr. Fritz Henneberger. I would like to thank him for giving me the opportunity to work in his group and for his support and supervision during this time.

Further I want to thank:

Dr. Joachim Puls for the introduction to several experimental setups and his help in some of the experiments.

Dr. Hans-Jürgen Wünsche for his support concerning numerical calculations. The theoretical analysis of the random laser data would not exist without his persistent efforts. I would also like to thank him for many stimulating discussions.

Dr. Sergey Sadofev for growth of the samples. Without his efforts in fabrication of high-quality samples this work would not have been possible.

Dr. Matthias Brandt, who took over this task later.

Dr. Simon Halm for many useful discussions and his help in some of the measurements.

Dr. Peter Schäfer for scanning electron microscopy measurements.

Dr. Holm Kirmse for is effort in focused ion beam milling of artificial holes in ZnO nanostructures.

Holger Spranger for assistance in the atomic force microscopy measurements.

H.-J. Pöhls from the Ferdinand-Braun-Institut for processing of the sapphire substrates by ultraviolet laser light.

I am grateful to everybody who has taken his time to read this manuscript. Further I would like to thank all current and former members of the Photonics group for the nice working atmosphere.

Selbständigkeitserklärung

Ich erkläre, dass ich die vorliegende Arbeit selbständig und nur unter Verwendung der angegebenen Literatur und Hilfsmittel angefertigt habe.

Berlin, den 04.06.2012 Sascha Kalusniak